Generating In-depth Process Knowledge by Computational Fluid Dynamics and a Novel Online Monitoring Technique for Shake Flasks

Gewinnung eines vertieften Prozessverständnis durch Computational Fluid Dynamics und eine neuartige Online-Messtechnik für Schüttelkolben

Von der Fakultät für Mathematik und Naturwissenschaften der
RWTH Aachen University zur Erlangung des akademischen Grades eines
Doktors der Naturwissenschaften genehmigte Dissertation

vorgelegt von

Carl Dinter, M. Sc.
aus
Düsseldorf

Berichter: Univ.-Prof. Dr. rer. nat. Arnold Reusken
Univ.-Prof. Dr.-Ing. Dr. h. c. (Osaka) Jochen Büchs

Tag der mündlichen Prüfung: 12.06.2025

“It is possible to commit no mistakes and still lose.

That is not weakness. That is life.”

Jean-Luc Picard – Captain of the USS Enterprise

Danksagung

Die vorliegende Arbeit wurde während meiner Tätigkeit als wissenschaftlicher Mitarbeiter am Lehrstuhl für Bioverfahrenstechnik der RWTH Aachen angefertigt. Teile meiner Arbeit wurden im Rahmen des „Zentrales Innovationsprogramm Mittelstand“ (KK5068601JO0). in Kooperation mit PyroScience. gefördert. Außerdem wurden im Rahmen des Projektes „rwth0850“ Rechenressourcen für die Computational Fluid Dynamics Simulationen auf dem HPC der RWTH Aachen gewährt.

Besonders danken möchte ich Prof. Dr.-Ing. Büchs für die Möglichkeit meine Promotionsarbeit am Lehrstuhl für Bioverfahrenstechnik anzufertigen. Ihre enge und direkte wissenschaftliche Betreuung, Begeisterung für alle Themen ihrer Doktoranden und Doktorandinen, sowie die wertschätzenden Diskussionen haben maßgeblich zum Gelingen meiner Arbeit beigetragen. Weiterhin möchte ich Prof. Dr. Arnold Reusken für die Möglichkeit der Promotion am Lehrstuhl für numerische Mathematik, sowie Prof. Dr. Maria Fyta für die Übernahme des Drittgutachtens danken. Darüber hinaus danke ich Prof. Dr. Christof Erich Melcher für die Übernahme des Prüfungsvorsitz.

Meine Promotion hat von zwei Kooperation entscheidend profitiert. Im Bereich der Computational Fluid Dynamics möchte ich Andreas Gumprecht und Dr. Sven Hansen für die Kooperation danken. Auch möchte ich mich an dieser Stelle bei Dr.-Ing. Amizon Azizan für die Aufbereitung und Bereitstellung ihrer Daten zu Flüssigkeitsverteilungen in Schüttelkolben bedanken. Mein weiterer Dank geht an Dr. David Flitsch und Moritz Mertens für die Kooperation im Bereich der kombinierten Onlinemesstechnik. Außerdem möchte ich hier David Vonester für die Zusammenarbeit und Übernahme des Projektes mit PyroScience danken.

Studierende haben als HiWis oder durch ihre Abschlussarbeiten tatkräftig zum Gelingen dieser Arbeit beigetragen. Ich möchte mich für die gemeinsame Arbeit und das Vertrauen, die Betreuung übernehmen zu dürfen, bedanken bei: Matthias Alexander Menze, Marc Tüschenbönner, Wayan Jonathan Schiwietz, Matthias Jan Pesch und Laura Barth.

Bei meinen ehemaligen Kollegen und Kolleginnen am Lehrstuhl möchte ich mich für die tolle Atmosphäre und den starken Zusammenhalt bedanken. Ich bin überzeugt, dass die Stimmung am Lehrstuhl mit dazu beigetragen hat die Promotion bis zum Ende durchzustehen.

Zu guter Letzt möchte ich von Herzen bei meiner Familie danken. Ihr habt mich mein gesamtes Leben, während Schulzeit, Studium und Promotionszeit unterstützt und Rückhalt gegeben. Danke, dass ihr immer für mich da seid und Vertrauen schenkt.

Zusammenfassung

Computational Fluid Dynamics (CFD) ermöglicht ein tiefgehendes Prozessverständnis und ist zu einem wichtigen Werkzeug im Design und Scale-up von Bioprozessen geworden. Für die Auslegung von Rührkesseln wird CFD bereits flächendeckend angewendet. Im Gegensatz hierzu ist die Anwendung bei geschüttelten Bioreaktoren, wie Schüttelkoben, besonders bei erhöhter Viskosität, sehr begrenzt. In dieser Arbeit wurde ein CFD-Modell für 250 mL Schüttelkolben etabliert und für eine Bandbreite an Schüttelbedingungen und Viskositäten bis zu 100 mPa·s angewendet. Anhand der CFD-Simulationen wurden der volumetrische Leistungseintrag, der k_La-Wert und die Scherrate berechnet. Die simulierte Flüssigkeitsbewegung stimmt mit experimentell ermittelten Flüssigkeitsverteilungen überein. Der berechnete volumetrische Leistungseintrag weicht im Mittel 0,18 kW/m^3 von experimentellen, volumetrischen Leistungseinträgen ab. Die k_La-Werte sind, über drei Größenordnungen, im Mittel doppelt so hoch, wie publizierte Daten. Die Scherrate wurde auf zwei verschiedene Weisen berechnet, wobei die erste Variante ungenügende Ergebnisse erzielt. Die zweite Variante, die anhand des größten Eigenwerts des Strain Rate Tensors berechnet wird, ist im Mittel 16 % kleiner, als publizierte Daten. Schlussendlich heben die CFD-Simulationen hervor, dass der Übergang zwischen in- und außer-Phase Bedingungen in Schüttelkolben inhärent gradueller Natur ist.

Die Prozessüberwachung ist ebenso von entscheidender Wichtigkeit für die Bioprozessentwicklung. Klassische Probennahme und Auswertung ist allerdings zeitaufwändig und stellt ein Kontaminationsrisiko da. Daher ist die Online-Überwachung wichtiger Prozessparameter zu bevorzugen. In dieser Arbeit sind Online-Überwachung der Gelöstsauerstoffsättigung (DOT), des pH-Wertes, des Streulichtes und der Viskosität in einem einzigen Messsystem für Schüttelkolben, ShakeVisc genannt, kombiniert. Die DOT-Messungen wurden mit sauerstoffsensitiven, fluoreszierenden Nanopartikeln realisiert. Für die pH Messungen wurden pH-sensitive, fluoreszierenden Sensorspots verwendet. Das Streulicht wurde mittels eines neuentwickelten, optischen Sensors bei 610 – 630 nm gemessen. Der Versatz der Winkelposition der rotierenden Flüssigkeit korreliert mit der Viskosität. Dieser Versatz wurde anhand der Fluoreszenzintensität der sauerstoffsensitiven Nanopartikeln und, zum ersten Mal, anhand der Streulichtintensität bestimmt. Das ShakeVisc-System wurde erfolgreich für Kultivierungen von *Escherichia coli*, *Paenibacillus polymyxa* and *Xanthomonas campestris* angewendet.

Abstract

Computational Fluid Dynamics (CFD) has become a pivotal tool in the design and scale-up of bioprocesses by providing deep process insights. It has been extensively researched and used in stirred tank reactors. Research for shaken vessels, like shake flasks, especially at elevated viscosity, is, however, very limited. In this work, a CFD model for 250 mL shake flasks has been established, simulating a variety of shaking conditions, including viscosity of up to 100 mPa·s. CFD model results were then used to calculate volumetric power input, volumetric gas-liquid mass transfer rate (k_La) and shear rates. Simulated fluid flow agrees well with experimentally recorded liquid distributions. Calculated volumetric power inputs deviate on average by 0.18 kW/m^3 from experimentally determined volumetric power inputs. k_La values, spanning almost three orders of magnitude, deviated by less than a factor of two from published data for k_La values in shake flasks. Shear rates were calculated in two ways, where the first showed unsatisfactory results. The second approach, which is based on the largest eigenvalue of the strain rate tensor, was on average 16 % smaller than indicated by published data for effective shear rates in shake flasks. Lastly, the CFD model highlighted the inherently gradual nature of the transition between so-called in-phase and out-of-phase operating conditions in shake flasks.

Process monitoring is also crucially important for design and scale-up of bioprocesses. Traditional offline sampling is, however, highly laborious, a risk for contamination and provides limited time resolution. Hence, online monitoring of key process parameters is highly advantageous. In this work, online monitoring of dissolved oxygen tension (DOT), pH, scattered light and viscosity were combined in a single monitoring system for shake flasks, termed ShakeVisc. DOT measurements were performed with oxygen sensitive fluorescent nanoparticles. The pH was measured with pH sensitive fluorescent sensor spots. Scattered light was measured at 610 – 630 nm with a newly developed optical sensor. The shift of the angle of the bulk liquid is correlated to the viscosity. This shift was determined based on the fluorescence intensity of the oxygen sensitive nanoparticles and, for the first time, based on scattered light signal intensity. The ShakeVisc system was successfully applied to cultivations of *Escherichia coli*, *Paenibacillus polymyxa* and *Xanthomonas campestris*.

Eidesstattliche Erklärung

Carl Dinter erklärt hiermit, dass diese Dissertation und die darin dargelegten Inhalte die eigenen sind und selbstständig, als Ergebnis der eigenen originären Forschung, generiert wurden. Hiermit erkläre ich an Eides statt

1. Diese Arbeit wurde vollständig oder größtenteils in der Phase als Doktorand dieser Fakultät und Universität angefertigt;
2. Sofern irgendein Bestandteil dieser Dissertation zuvor für einen akademischen Abschluss oder eine andere Qualifikation an dieser oder einer anderen Institution verwendet wurde, wurde dies klar angezeigt;
3. Wenn immer andere eigene- oder Veröffentlichungen Dritter herangezogen wurden, wurden diese klar benannt;
4. Wenn aus anderen eigenen- oder Veröffentlichungen Dritter zitiert wurde, wurde stets die Quelle hierfür angegeben. Diese Dissertation ist vollständig meine eigene Arbeit, mit der Ausnahme solcher Zitate;
5. Alle wesentlichen Quellen von Unterstützung wurden benannt;
6. Wenn immer ein Teil dieser Dissertation auf der Zusammenarbeit mit anderen basiert, wurde von mir klar gekennzeichnet, was von anderen und was von mir selbst erarbeitet wurde;
7. Ein Teil oder Teile dieser Arbeit wurden zuvor veröffentlicht. Eine Auflistung findet sich im Kapitel Funding and Publications.

Funding and Publications

Simulations in chapter 2 ‘Computational Fluid Dynamics for Shake Flasks’ were performed with computing resources granted by RWTH Aachen University under project rwth0850.

The work in chapter 3 ‘Online Monitoring of Dissolved Oxygen Tension, Biomass, pH and Viscosity in Shake Flasks’ was supported by Zentrales Innovationsprogramm Mittelstand (ZIM) [grant number KK5068601JO0].

Parts of this thesis have been published previously. Any thought, methodology, result and conclusion that is part of an existing publication with first authorship is not explicitly referred to but considered as properly cited by the following listing:

- Dinter, C., Gumprecht, A., Menze, M. A., Azizan, A., Niehoff, P.-J., Hansen, S., Büchs, J. Validation of computational fluid dynamics of shake flask experiments at moderate viscosity by liquid distributions and volumetric power inputs. *Scientific reports* **14**, 3658 (2024).
- Dinter, C., Gumprecht, A., Menze, M. A., Azizan, A., Hansen, S., Büchs, J. Exploration of the out-of-phase phenomenon in shake flasks by CFD calculations of volumetric power input, k_La value and shear rate at elevated viscosity. *Biotechnology and Bioengineering* **122**, 509-524 (2024).
- Dinter, C. †, Vonester, D. †, Flitsch, D., Mertens, M., Tüschenbönner, M., Hoffmann, M., Büchs, J., Magnus, J. Combined optical measurement of dissolved oxygen tension (DOT), pH value, biomass and viscosity in shake flasks. *Biochemical Engineering Journal* **212**, 109515 (2024).

† Authors contributed equally to the work

Contributions to further publications during the preparation of this thesis:

- Sparviero, S., Barth, L., Keil, T., Dinter, C., Berg, C., Lattermann, C., Büchs, J. Black glucose-releasing silicon elastomer rings for fed-batch operation allow measurement of the oxygen transfer rate from the top and optical signals from the bottom for each well of a microtiter plate. *BMC Biotechnol* **23**, 5 (2023).

Contributions to publications that are currently in preparation:

- Hanke, R., Wollborn, D., Dinter, C., Ojima, Y., Büchs, J. Relative maximum oxygen transfer capacity at elevated viscosity in shake flasks is highly dependent on shaking frequency and diameter.

Contributions to conferences during the preparation of this thesis:

- Dinter, C., Sieben, M., Büchs, J. (2021). Non-invasive online viscosity monitoring in shake flasks. Oral presentation. 13th ECCE and 6th ECAB, digital conference
- Dinter, C., Sieben, M., Azizan, A., Büchs, J. (2021) New online viscosity measurement in shake flasks. Poster. ESBES2021, digital conference
- Dinter, C., Büchs, J., Flitsch, D., Mertens, M. (2022) Minimal-invasive online monitoring of dissolved oxygen tension, viscosity, scattered light and pH in shake flask cultivations. Oral presentation. Himmelfahrtstagung on Bioprocess Engineering 2022, Mainz, Germany

Table of Contents

Nomenclature

Name	Abbreviation	Unit
CFD	Computational Fluid Dynamics	
CGQ	Cell Growth Quantifier	
CTR	Carbon dioxide transfer rate	mmol/L/h
d	Largest inner flask diameter	mm or m
d_0	Shaking diameter	cm or m
D_L	Diffusion coefficient	m^2/s
DOT	Dissolved oxygen tension	% air saturation
f_{GW}	Gierer and Wiertz correction factor	-
F_σ	Surface tension	N/m
g	Gravitational acceleration	m/s^2
GY medium	Glucose-Yeast medium	
k	Turbulent kinetic energy	m^2/s^2
K	Flow consistency index	$Pa \cdot s^m$
k_B	Boltzmann constant	J/K
k_La	Volumetric gas-liquid mass transfer rate	h^{-1} or s^{-1}
m	Flow behavior index	-
MOPS	(N-morpholino)-propane sulfonic acid	
MW	Molecular weight	Da
n	Shaking frequency	min^{-1} or s^{-1}
N_A	Avogadro's constant	mol^{-1}
Ne´	Modified Newton number	-
OD_{600}	Optical density at 600 nm	-
OTR	Oxygen transfer rate	mmol/L/h
p	Pressure	Pa
P	Power input	W or $kg \cdot m^2/s^3$
Ph	Phase number	-
pK_a	Acid dissociation constant	-
qO_2	Specific oxygen uptake rate	mmol/g/h
RAMOS	Respiratory activity monitoring system	
Re	Reynolds number	-
Re_{film}	Reynolds film number	-
r_M	Molecule radius	Å
S	Strain rate tensor	s^{-1}

$\|\|\mathbf{S}\|\|$	Scalar measure of the strain rate tensor	s^{-1}
SFR	Shake Flask Reader	
STR	Stirred tank reactor	
t	Time	s
T	Temperature	K
TOM	Transfer-rate online measurement	
$\mathbf{U}$	Velocity vector	m/s
V_L	Filling volume	mL or L
VOF	Volume of fluid	
YM medium	Yeast-Malt medium	
α	Volume fraction	-
β	Ratio of radii of solute and solvent	-
γ	Shear rate	s^{-1}
ε	Energy dissipation rate	W/kg or m^2/s^3
θ	Angle of bulk liquid	°
θ_0	Angle of bulk liquid at the beginning of cultivation	°
η	Dynamic viscosity	Pa·s
κ	Approximation of the curvature at the interface	-
ν	Kinematic viscosity	m^2/s
ρ	Density	kg/m^3
ρ_{eff}	Effective density	kg/m^3
σ	Surface tension constant	N/m
τ	Viscous stress	Pa
τ_L	Average shear stress	Pa
τ_t	Turbulent stress	Pa
ω	Specific energy dissipation rate	s^{-1}
$\vec{\omega}$	Angular velocity	rad/s

List of Tables

List of Figures

Chapter 1

1 Introduction

Shake flasks are widely used in the early stages of bioprocess development e.g., in strain selection or media optimization. They are a simple, cost-effective tool and easily parallelized. However, useful experiments, enabling a straightforward scale-up require deep process knowledge. Shake flasks have been researched extensively in the last decades. Investigations into the mechanisms of gas transfer[1,2], power input[3,4], fluid flow[5,6] and shear rate in shake flasks[7] have been conducted.

Due to their useful rheological properties, biopolymers are used in medicine for drug delivery and drug release systems, wound dressing and injections for joint health and as additives in the food and cosmetic industry[8–10]. Well-known examples are xanthan[11,12] and alginate[10,13,14]. Filamentous fungi are, similarly, applied industrially for the production of useful chemical compounds, including organic acids, antibiotics, enzymes like glucoamylases and as meat substitutes[15–19]. Virtually all biopolymer solutions and culture broths of filamentous fungi are viscous, non-Newtonian fluids, showing pronounced shear-thinning behavior, i.e., a reduction in viscosity with increasing shear rates. The increasing viscosity during fermentation, however, leads to a lot of problems, including diminished mixing efficiency and insufficient oxygen supply[9,20].

Most notably, the viscosity is one of the major contributors to the so-called out-of-phase phenomenon, described by Büchs et al.[3,4]. The out-of-phase phenomenon, describes a situation, where the centrifugal force caused by the orbital shaking motion of the shaking table is insufficient to accelerate the liquid phase. At in-phase operating conditions, the bulk liquid follows the shaking motion of the shaker, whereas at out-of-phase operating conditions a

complete collapse of the bulk liquid, with uncoordinated liquid movement, can be observed. Low shaking frequency, low filling volume, small shaking diameters and, importantly, high viscosity all contribute to out-of-phase operating conditions. Büchs et al. suggested the dimensionless phase number as an indicator for the degree, to which the liquid is out-of-phase with the shaking motion[3,4]. Based on experimentally determined volumetric power inputs, they found a critical phase number of 1.26, below which the out-of-phase phenomenon predominates[4]. At in-phase operating conditions, the volumetric power input increases continuously with increasing viscosity, but at out-of-phase operating conditions, the volumetric power input becomes far less predictable and stagnates or sometimes even declines. Büchs et al. provide a correlation of the Reynolds number and modified Newton number for in-phase operating conditions, enabling the calculation of volumetric power inputs[4]. Azizan et al. further investigated the out-of-phase phenomenon and used experimental liquid distributions in shake flasks to determine a new critical phase number of 0.91[5].

As mentioned, biopolymers exhibit non-Newtonian properties, requiring the estimation of shear rates, to accurately determine the effective viscosity in shake flask experiments. Giese et al. developed a correlation for effective shear rates in shake flasks for in-phase operating conditions with shear-thinning fluids[7]. They used a power law approach to model the shear-thinning behavior.

The oxygen transfer in shake flasks is best described by the so-called “two sub-reactor model” from Maier et al.[2]. In this model, the oxygen transfer into the rotating bulk liquid is the first sub-reactor and can be calculated with the models by Kawase and Moo-young[21] or by Gnielinski[22]. The second sub-reactor is the liquid film, which is formed and left behind on the flask wall by the rotating bulk liquid. The oxygen transfer into this liquid film is modelled with Higbie’s penetration theory. An increase in viscosity significantly lowers the diffusion coefficient in the bulk liquid and film. It, however, also leads to thicker liquid films on the shake flask wall. Giese et al. found, that small increases in viscosity lead to an increase in the maximum oxygen transfer capacity, despite the reduction of the oxygen diffusion coefficient in the liquid[23]. The increasing liquid film thickness, leading to an increased capacity to store oxygen in the film, explains this effect. At a specific film thickness, however, the oxygen transfer in the film is no longer limited by the capacity to store oxygen in the film. Rather, the duration until the bulk liquid rolls over the liquid film again, which depends on the shaking frequency of the shaking table, limits the oxygen transfer. The liquid film no longer reaches oxygen saturation during the revolution, hence, the reduction of the oxygen diffusion coefficient,

with increasing viscosity, outweighs the benefits of an increased capacity to store oxygen. The maximal oxygen transfer capacity is reached at roughly 10 – 20 mPa·s in shake flasks. Besides the discussed model by Maier et al.[2], multiple attempts to correlate the k_La value to the operating conditions in shake flasks have been published[24–28]. However, to our knowledge, only Henzler and Schedel included the viscosity in their correlation by fitting to experimental data for a variety of viscosities.

The discussed investigations into the out-of-phase phenomenon, volumetric power input and oxygen transfer are all based on online monitoring of shake flask cultivations. In general, online monitoring is an immensely powerful tool in generating process knowledge. Computational Fluid Dynamics (CFD) is another pivotal tool for bioprocess design. For large stirred tanks, in later stages of bioprocesses, CFD is already widely used in academia and industry alike[29–38]. In contrast, prevalence of CFD for shake flasks is much lower. Only a limited body of research exists on the topic[39–42].

The first aim of this thesis is to establish and verify a CFD model for shake flasks at a variety of shaking conditions and viscosity. The CFD model will be used to predict fluid flow, volumetric power input, volumetric gas-liquid mass transfer rate (k_La) and shear rates. The second aim of this thesis is the combination of DOT, scattered light, pH and viscosity online monitoring into a single system called ShakeVisc. DOT and pH will be measured with commercially available nanoparticles and sensor spots from PyroScience. Scattered light will be measured by a sensor developed with PyroScience. Viscosity can be determined from the nanoparticle and scattered light signal. Importantly, DOT and scattered light measurement will be triggered to ensure measurement within the rotating bulk liquid.

Contribution statement for chapter 2:

The following chapter is a combination of the publications “Validation of computational fluid dynamics of shake flask experiments at moderate viscosity by liquid distributions and volumetric power inputs”, published in Scientific Reports and “Exploration of the out-of-phase phenomenon in shake flasks by CFD calculations of volumetric power input, k_La value and shear rate at elevated viscosity” published in Biotechnology and Bioengineering. Andreas Gumprecht provided a first implementation of the CFD model, performed first simulations for waterlike viscosity and provided valuable input during the entire study. Matthias Alexander Menze supported this work during his master thesis at AVT.BioVT at RWTH Aachen University. He implemented first passes of the calculation of volumetric power input and k_La and performed CFD simulations at elevated viscosity. Dr. Amizon Azizan kindly restructured and provided experimental data of liquid distributions. Prof. Jochen Büchs and Dr. Sven Hansen initiated the cooperation and supervised the project. I performed all remaining CFD simulations, finalized the calculations of volumetric power input, k_La and shear rates, analyzed the data and created the figures.

Chapter 2

2 Computational Fluid Dynamics for Shake Flasks

2.1 Background

Computational Fluid Dynamics (CFD) has proven to be an extremely valuable tool for the computation of common process performance indicators in stirred tank reactors (STRs), such as volumetric power input, mixing times and inhomogeneities, gas hold-up, shear stress and k_La [29–38,43]. In contrast, CFD applications for small scale, shaken bioreactors, such as microtiter plates[44–48], shake flasks[39–42] and other small cylindrical vessels[49] are scarce in the scientific literature. Zhang et al. used a CFD model for shake flasks to calculate the volumetric power input and k_La for a variety of shaking parameters[41]. Similarly, Li et al. calculated the k_La value from CFD models, while investigating the influence of baffles in shake flask[40]. Furthermore, they determined the effect of shear stress on mycelial cell cultures. Liu et al. also used a CFD model to compute k_La and shear stress in baffled and unbaffled flasks, in order to investigate the effects on plant cell cultures[39]. In contrast to Li et al.[40], they not only calculated average shear stress, but also proposed an approach to estimate the distribution of hydromechanical stress. To our knowledge, Mehmood et al. published the only CFD simulations in shake flasks with non-Newtonian, shear-thinning liquids. The effect of the shear-thinning behavior is, however, minuscule. Above shear rates of 100 s^{-1}, which is exceeded in virtually all shake flask experiments, the fluids show a Newtonian plateau, resulting in an elevated viscosity of up to 3 mPa·s with essentially Newtonian behaviour[42]. They calculated power dissipation and k_La, assuming laminar flow, outlining the importance of these parameters for culture performance

of a filamentous microorganism[42]. Discacciati et al. performed simulations for small cylinders at an extremely high viscosity of 1000 mPa·s[49]. CFD models have also been already used for the development of novel shaken bioreactor designs[48,50,51]. For example, He et al. used a CFD model, employing a RNG k-epsilon turbulence model, to design a novel well type for microtiter plates, computing the k_La at a variety of shaking conditions, including viscosities of up to 30 mPa·s[48].

A comprehensive validation of CFD models is crucial to achieve reliable results. In principle. two avenues for directly validating the liquid flow in shake flasks exist. Firstly, the internal fluid flow can be recorded with techniques like Particle Image Velocimetry[52–54] (PIV) and Particle Tracking Velocimetry[55,56] (PTV). Both techniques are the most common and accurate techniques to measure the internal liquid flow in STRs[31] . They have already been used before in the small scale, e.g., cylindrical bioreactors[57,58] and shake flasks by Palacios-Morales et al.[59]. Palacios-Morales et al. provide a great inside into the flow behavior in shake flask and investigate the effects of baffle structures of the fluid flow. They do so for a single set of experimental conditions at a relatively low shaking frequency of 150 rpm. Unfortunately, this does not provide enough data for thoroughly validating a CFD model for shake flasks. Secondly, the liquid flow in CFD models for shake flasks can be validated by the externally observable liquid distribution. This approach has already been used in the literature for the validation of larger, orbitally shaken, cylindrical bioreactors[60,61]. The orbital shaking motion in orbitally shaken experiments drives the liquid along the flask wall, leading to distinct, externally observable liquid distributions (see Fig. 2-1). In non-baffled shake flasks such liquid distributions are in a quasi-steady state, except for the angular rotation due to the shaking motion. Hence, CFD models for shake flasks can simply be validated by comparing the liquid distribution, taken from CFD simulations, to photographs of the rotating bulk liquid in shake flasks[41]. The necessary photographs can be obtained with a rotating camera, where the angular position relative to the centrifugal force and, hence, to the bulk liquid remains constant[62,63]. Although a direct comparison to photographs is possible, the approach is hardly quantifiable and highly subjective. Zhu et al. improved this approach by recording the liquid distribution of orbitally shaken cylinders with filling volumes of 2.5 to 10 L and smaller cylinders with a conical bottom with high-speed cameras, measuring the liquid height in those videos[60,61].

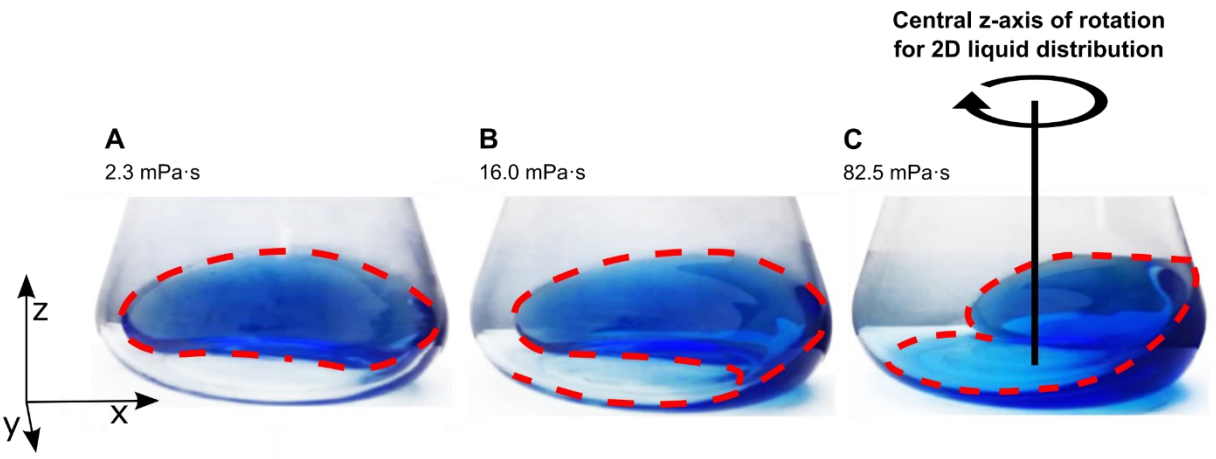

Fig. 2-1: Liquid distribution as a function of viscosity

Photographs of the rotating liquid in shake flasks are adapted from Sieben et al.[64] and shown at (A) 2.3 mPa·s, (B) 16 mPa·s and (C) 82.5 mPa·s, taken with a rotating camera, which is fixed, relative to the direction of centrifugal force and, hence, in a fixed position to the bulk liquid[62,63]. The centrifugal force is pointing in the negative y-direction in all 3 images. With the dashed red line, the liquid contact line at the intersection of liquid, glass and air is highlighted. This contact line is considered representative for the entire liquid distribution and responds to changes in the operating conditions, as shown for viscosity. The contact line is, therefore, an ideal tool to validate CFD calculations. Shaking conditions: Filling volume (V_L) = 30 mL, shaking frequency (n) = 150 rpm, shaking diameter (d_0) = 5 cm, temperature (T) = 25°C

Azizan et al. aimed to provide quantitative data for the liquid distributions in shake flasks[5,6]. Based on previous work by Ottow et al.[65], the devised measurement system employed non-invasive fluorescence measurements. Liquid contact lines at the intersection of liquid, air and glass were recorded at 14 distinct heights, each 5 mm apart. Liquid contact lines are representative of the entire liquid distribution and are responsive to changes in the operating conditions. Illustrations of such liquid contact lines are depicted as dashed red lines in Fig. 2-1 for a variation of the viscosity. The overall shape of the liquid distribution and, consequently, the liquid contact line changes with the increase in viscosity. For all three viscosities, the centrifugal force points in the same direction, indicating the shaker tray is in the same angular position. The leading edge of the rotating bulk liquid is shifted against the shaking direction, out of alignment with the centrifugal force, as can be seen in Fig. 2-1. This is the on-set of the out-of-phase phenomenon described previously. Sieben et al.[64], Ladner et al.[66] and Hoffmann et al.[67] have previously exploited this shift of the leading edge against the shaking direction to measure the viscosity in shake flask experiments.

The aim of this chapter is to establish and validate a CFD model for shake flasks from waterlike to viscosity of 100 mPa·s. The model will be validated with experimental liquid distribution data from Azizan et al.[5,6], in terms of the shape of the liquid distribution and overall position

relative to the centrifugal force, at a variety of shaking conditions. Furthermore, the simulations are compared to experimentally determined volumetric power inputs and the volumetric power input correlation from Büchs et al.[3,4], k_La values, calculated with the correlation by Henzler and Schedel[28] and shear rates, calculated with the correlation by Giese et al.[7].

2.2 Materials and Methods

2.2.1 The interFoam solver

The CFD simulations in this work were performed with OpenFOAM version 9, released by the OpenFOAM Foundation[68]. For an accurate estimation of the liquid movement in shake flasks, the interface between gas and liquid phase must be resolved. When handling incompressible and immiscible fluids, the Volume of Fluid (VOF) method is the standard approach for this situation. Instead of solving a set of Euler equations for each fluid separately, the VOF method needs to solve only one set of Euler equations for the average conditions in each mesh cell. The VOF method only requires a single extra conservation equation for the volume fraction. This leads to a significantly lower computation effort, compared to "true" two-phase simulation approaches. In the simulations in this work the interFoam solver was used for performing the VOF simulations. It solves the standard conservation equations for mass and momentum for incompressible fluids:

$$\nabla \cdot \mathbf{U} = 0 \qquad \text{Eq. 1}$$

$$\frac{\partial(\rho \mathbf{U})}{\partial t} + \nabla \cdot (\rho \mathbf{U}\mathbf{U}) = -\nabla p + \nabla \cdot (\tau + \tau_t) + \rho \mathbf{g} + \mathbf{F}_{\boldsymbol{\sigma}} \qquad \text{Eq. 2}$$

where $\mathbf{U}$, ρ, p, τ, τ_t, $\mathbf{g}$ and $\mathbf{F}_\sigma$ are the velocity in m/s, density in kg/m^3, pressure in Pa, viscous and turbulent stress in Pa, gravity acceleration on the reverse z-axis in m/s^2 and surface tension in N/m^2. Additionally, the VOF method implements a conservation equation for the interface:

$$\frac{\partial \alpha_L}{\partial t} + \nabla \cdot (\alpha_L \mathbf{U}) = 0 \qquad \text{Eq. 3}$$

where α_L encodes the volume fraction of liquid phase in each mesh cell. Accordingly, the following constraint on α exists:

$$\sum \alpha_i = 1 \qquad \text{Eq. 4}$$

where α_i encodes the volume fraction of phase i. In this work only two phases are simulated, a liquid and a gas phase i.e., water and air. If the volume fraction for the liquid phase $\alpha_L = 1$, the cell in question is entirely filled with water and for $\alpha_L = 0$ with air. In the case of $0 < \alpha_L < 1$ the cell is part of the free surface between both phases. Furthermore, the volume fraction is used to determine the average density and viscosity as follows:

$$\rho = \alpha_L \cdot \rho_L + (1 - \alpha_L) \cdot \rho_G \quad \text{Eq. 5}$$

$$\eta = \alpha_L \cdot \eta_L + (1 - \alpha_L) \cdot \eta_G \quad \text{Eq. 6}$$

where ρ_L, ρ_G, η_L and η_G are the density and viscosity of the liquid and gas phase, respectively. The surface tension is modelled as a continuum surface force (CSF)[69,70], calculated as follows:

$$\mathbf{F}_\sigma = \sigma \kappa \nabla \alpha_L \quad \text{Eq. 7}$$

$$\kappa = -\nabla \cdot \left(\frac{\nabla \alpha}{|\nabla \alpha|} \right) \quad \text{Eq. 8}$$

where σ is the surface tension constant in N/m^2 and κ is an approximation of the curvature at the interface[69,70]. Previously, a critical Reynolds number for turbulent flow of 60,000 in shake flasks has been proposed by Peter et al.[71]. Although a Reynolds number of 60,000 is not achieved under usual shaking conditions for 250 mL shake flasks, some experiments in this work come close (Re ~ 55,000 for conditions in Fig. 2-7G). Hence, at least transitional flow is to be expected for some of the simulated conditions. Nevertheless, a simulation for fully laminar conditions was conducted in preliminary calculations. Volumetric power input for this fully laminar simulation was, however, only half of the experimentally determined volumetric power input. Therefore, the k-omega Shear Stress Transport (k-omega SST) turbulence model was utilized in the simulations[72]. The k-omega SST model implements the k-epsilon model in the free shear stream, but switches to the k-omega model for better model performance up to the shake flask wall, through the viscous sublayers. This makes the k-omega SST model applicable as a low Reynolds number turbulence model.

In OpenFOAM the k-omega SST model from Menter et al.[72] is implemented. They give the conservation equations for the turbulent kinetic energy (k) and the specific energy dissipation rate (ω) as follows:

$$\frac{\partial(\rho k)}{\partial t} + \nabla \cdot (\rho \mathbf{U} k) = \tilde{P} - \beta^* \rho \omega k + \nabla \cdot [(\eta + \sigma_k \eta_t) \nabla k] \quad \text{Eq. 9}$$

$$\frac{\partial(\rho\omega)}{\partial t} + \nabla \cdot (\rho \mathbf{U}\omega) = \frac{\gamma\rho}{\eta_t}\tilde{P} - \beta\rho\omega^2 + \nabla \cdot [(\eta + \sigma_\omega \eta_t)\nabla\omega] + 2(1 - F_1)\frac{\rho\sigma_{\omega 2}}{\omega}\nabla k \cdot \nabla\omega \quad \text{Eq. 10}$$

with $\tilde{P}$ being the limiter of the production of turbulent kinetic energy, η, η_t the viscosity and turbulent viscosity, respectively and F_1 a blending function. β^*, σ_k, γ and σ_w are model coefficients. The production limiter is given as:

$$\tilde{P} = \min(\eta_t \nabla \mathbf{U}{:}\mathbf{S}, 10\beta^*\rho k\omega) \quad \text{Eq. 11}$$

where **S** is the strain rate tensor. The strain rate tensor is the symmetric part of the gradient of the velocity vector field. The symmetric part describes the rate of shearing and stretching in the velocity field. The antisymmetric part, called vorticity tensor or spin tensor, describes only rotational movement. F_1 is a blending function, which leads to the transition from the k-omega SST to the k-epsilon model and is defined as:

$$F_1 = \tanh\left\{\left\{\min\left[\max\left(\frac{\sqrt{k}}{\beta^*\omega y}, \frac{500\eta}{y^2\omega\rho}\right), \frac{4\rho\sigma_{w2}}{CD_{k\omega}y^2}\right]\right\}\right\} \quad \text{Eq. 12}$$

where y is the normal distance from the nearest wall and $CD_{k\omega}$ is given as:

$$CD_{k\omega} = \max\left(2\frac{\rho\sigma_{\omega 2}}{\omega}\nabla k \cdot \nabla\omega, 10^{-10}\right) \quad \text{Eq. 13}$$

For the turbulent viscosity, Menter et al.[72] give the following expression:

$$\frac{\eta_t}{\rho} = \frac{a_1 k}{\max(a_1\omega; \|\mathbf{S}\|F_2)} \quad \text{Eq. 14}$$

where a_1 is another model coefficient, ||**S**|| a scalar measure for the strain rate tensor and F_2 a second blending function, which is defined as:

$$F_2 = \tanh\left[\left[\max\left(\frac{2\sqrt{k}}{\beta^*\omega y}, \frac{500\eta}{y^2\omega\rho}\right)\right]^2\right] \quad \text{Eq. 15}$$

The scalar measure for the strain rate tensor is defined as follows:

$$\|\mathbf{S}\| = \sqrt{2\mathbf{S}:\mathbf{S}} \qquad \text{Eq. 16}$$

$$= \sqrt{2 \cdot \left[\left(\frac{\partial u}{\partial x}\right)^2 + \left(\frac{\partial v}{\partial y}\right)^2 + \left(\frac{\partial w}{\partial z}\right)^2\right] + \left(\frac{\partial u}{\partial y} + \frac{\partial v}{\partial x}\right)^2 + \left(\frac{\partial v}{\partial z} + \frac{\partial w}{\partial y}\right)^2 + \left(\frac{\partial u}{\partial z} + \frac{\partial w}{\partial x}\right)^2}$$

where u, v and w are the velocity components in direction of the cartesian coordinates x, y and z. All model coefficients, used in Eq. 9 - Eq. 16, are given in Table 2-1. Model coefficients, which are given with subscripts 1 and 2 are also blended with blending function F_1, according to the following expression:

$$\varphi = \varphi_1 F_1 + \varphi_2 (1 - F_1) \qquad \text{Eq. 17}$$

Table 2-1: Model coefficients of the k-omega SST model.

Model coefficient	**Value [-]**
β^*	0.09
a_1	0.31
σ_{k1}	0.85
σ_{k2}	1
$\sigma_{\omega 1}$	0.5
$\sigma_{\omega 2}$	0.856
β_1	0.075
β_2	0.0828
γ_1	5/9
γ_2	0.44

Simulations were transient and performed with an adjustable time step, limited by a maximal Courant number of 1 and additionally, a maximal time step of 0.005 s.

Material parameters for the simulations (see Appendix 1) were taken from the VDI Heat Atlas[73].

2.2.2 Modelling the shaking motion

Shake flasks are usually agitated on orbital shakers with a given shaking diameter and shaking frequency. Directly simulating this shaking motion requires a recalculation of the positioning

of mesh at each timepoint. To avoid the computational expense of mesh recalculation, the modelling approach from Li et al. was implemented[40]. They reduced the shaking motion down to a cyclic centrifugal force, sweeping around the stationary shake flask. The forces in the x and y direction can be calculated as follows:

$$F_x = \vec{\omega}^2 \cdot \frac{d_0}{2} \cdot \cos(\omega \cdot t) \quad \text{Eq. 18}$$

$$F_y = \vec{\omega}^2 \cdot \frac{d_0}{2} \cdot sin(\omega \cdot t) \quad \text{Eq. 19}$$

where $\vec{\omega}$, d_0 and t are the angular velocity in rad/s, shaking diameter in m and point in time in s. All simulations in this work were performed with a runtime of 10 s. In the first 0.5 s of this runtime the shaking frequency linearly ramps up from a standstill to the desired shaking frequency.

2.2.3 Shake flask geometry and mesh generation

Generally, the geometry of shake flasks consists of a partial torus for the lower part and an added cone for the upper part of the shake flask. Two approaches to model the intersection between lower torus and upper cone are used in this work (Fig. 2-2). The first approach is consistent with one in the simplified mechanistic model by Büchs et al.[74] and is used for the comparison to the simplified mechanistic model. It approximates the lower part as a quarter torus (90°) with an added cone as the upper part of the flask[74], as illustrated in Fig. 2-2A, leading to a sharp transition between lower and upper part of the shake flask. In the second approach the curvature of the torus is extended until it is in line with the slope of the added cone (107.2°), as shown in Fig. 2-2B, creating a smooth transition between lower and upper part. This second approach resembles the real shake flask geometry much more closely (see Appendix 2). All dimensions are otherwise consistent between both approaches. They include a torus radius of 14.5 mm (Fig. 2-2), maximal diameter of 81.6 mm (Fig. 2-3B) at a height of 14.5 mm, tapering down to a diameter of 30.7 mm at a height of 99 mm (Fig. 2-3B), equating to an angle of 16.76° for the cone, as can be seen in Fig. 2-2. The rise of the center of the bottom in the shake flask, formed during the cooling step in the production of shake flasks, is modelled in neither approach. Instead, a flat bottom with a diameter of 52.6 mm is assumed (Fig. 2-3B). Mean precise inner shake flask dimensions were taken from three shake flasks, after milling them to exactly half their maximal outer diameter (done by Aachener Quarzglas-Technologie Heinrich GmbH &

Co.KG). Photographs of the three shake flasks are shown in the supplementary information (Appendix 2).

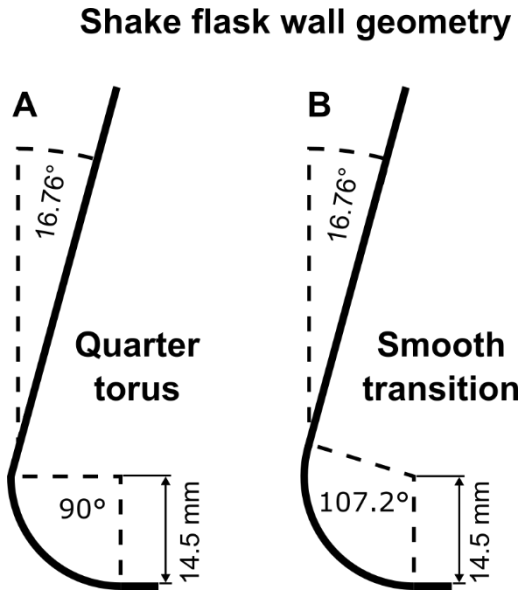

Fig. 2-2: Schematic illustration of the shake flask geometry.

Two approaches in modelling the basic shape of shake flasks are shown. (A) The shake flask is modelled as a quarter torus (r = 14.5 mm) with an added cone (16.76°) for the upper part, leading to a sharp transition between the segments[74]. (B) The curvature of the torus (r = 14.5 mm) is extended until it is in line with the slope of the cone (16.76°), leading to a smooth transition.

After the implementation of the basic flask geometry, the meshing was performed with the *blockMesh* and *snappyHexMesh* utilities, included in OpenFOAM. The finished mesh for the flask geometry with a smooth transition between torus and cone part (refer Fig. 2-2B) is shown in Fig. 2-3. During the meshing process *blockMesh* is used to create a first, basic mesh, which is then refined or *chiselled* to precisely fit the intended geometry with *snappyHexMesh* [75]. In this work a cylindrical, hexahedral mesh with a diameter slightly larger than the maximal shake flask diameter is created with *blockMesh*. Afterwards the mesh is refined with the three steps of castellation, snapping and an addition of layers with *snappyHexMesh*. During castellation all mesh cells of the cylindrical mesh, which are more than 50 % outside of the flask geometry, are removed. Additionally, refinement steps, dividing one cell into eight, can be included. In this work one refinement region was applied to the entire inside of the shake flask, affecting all cells of the mesh. Furthermore, two refinement steps with the shake flask wall as the refinement surface were applied during castellation. The resulting edges of the cell refinement are clearly visible in Fig. 2-3. One can be seen with a diameter of 22.1 mm in Fig. 2-3b and one roughly 1 mm from the shake flask wall in the close-up view in Fig. 2-3A. The castellation creates a jagged surface at the flask wall. During snapping, vertex points of those initially hexahedral

cells are moved on the flask wall surface. Affected cells are no longer necessarily hexahedral afterwards. Although this step leaves a perfectly smooth surface, some, if not all, of the cells at the surface might be irregularly shaped leading to potentially poor CFD performance. Therefore, in the last step of snappyHexMesh additional layers of hexahedral cells can be added parallel to the snapped surface. In this work, three additional layers were added at the shake flask wall, as can be seen in Fig. 2-3A. The first layer, closest to the wall, is the thinnest layer with a thickness of roughly 140 µm, with following layers being 20 % larger than the preceding layer. The generated, final mesh has about $1.4 \cdot 10^6$ cells in total.

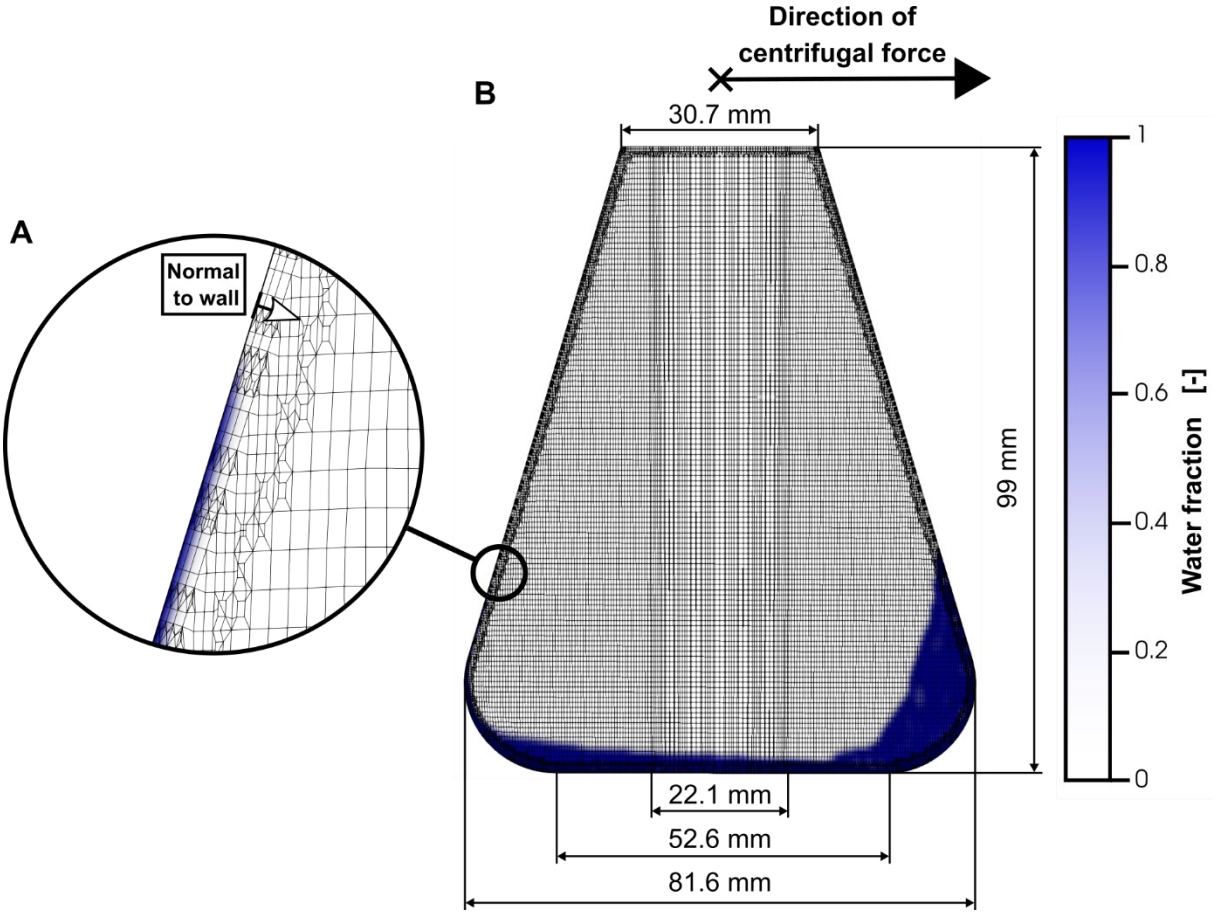

Fig. 2-3: Cross-section of the meshed shake flask.

In (B) the cross-section of the entire shake flask mesh can be seen. A close-up view of the wall is depicted in (A). The 3D model of the shake flask is meshed with the OpenFOAM utility *snappyHexMesh*. First, a cylindrical base mesh is created with *blockMesh*. Two refinement steps (factor 8 increase in mesh resolution), introduced during the castellated meshing of *snappyHexMesh* can be seen. One refinement step is introduced at a diameter of 22.1 mm. A second one can be seen near the shake flask wall in (A). Additionally, three wall layers, depicted in (A) are introduced. Wall layers are orientated parallel to the shake flask wall, as indicated by the arrow normal to the wall in (A). A completely flat bottom with a diameter of 52.6 mm is modelled. In total, the meshed shake flask model consists of roughly 1.4 million cells. The color scale from white to blue indicates the water fraction of the simulated CFD case. Simulated conditions: Viscosity (η) = 16.7 mPa·s, shaking diameter (d_0) = 2.5 cm, filling volume (V_L) = 40 mL, shaking frequency (n) = 250 rpm, surface tension (σ) = 70 mN/m, contact angle (Θ) = 20°, temperature (T) = 25°C

2.2.4 Extraction of liquid contact lines

Liquid contact lines, as a representation of the entire liquid distribution, are extracted with the *probes* post processing function, included in OpenFOAM. The *probes* function can be used to return field values of mesh cells closest to a provided combination of cartesian coordinates. In the case of this work, the liquid volume fraction α_L is returned for sampled cells. Cells are sampled along the flask wall with a distance of 0.5 mm in the z-axis and 1°-degree steps around the central z-axis of the shake flask, leading to roughly 72000 sampled positions. For each sampled angle, the liquid contact line is determined separately. To this end, all cells with an α_L value above 0.5 are considered as cells filled with water and below 0.5 with air. Descending from the top of the shake flask all changes from air filled to water filled cells and vice versa are recorded and plotted over their respective angle, leading to representations like Fig. 2-5. The described process is usually repeated for multiple, normal distances from the wall (Fig. 2-3A), as can be seen in Fig. 2-6 and Fig. 2-7. Even for the first repetition of the extraction of liquid contact lines, a distance of 50 µm is chosen to ensure sampled positions are within the mesh cells. Positions exactly on the shake flask wall might not be considered as within the meshed geometry by the *probes* function. For further repetitions, the normal distance is increased by 200 µm up to a normal distance of 1050 µm.

2.2.5 Simplified mechanistic model of liquid distributions in shake flasks

For a first comparison of the liquid contact lines, the simplified, mechanistic model for liquid distributions in shake flasks by Büchs et al.[74] was used. The model entirely neglects viscous forces and describes the shaking motion as a superposition of a translatoric and an opposing rotation of the shake flask. This allows for an approximation of the liquid distributions inside of the shake flask as an intersection of a symmetrical paraboloid and the shake flask wall geometry, where the overall shape of the paraboloid is determined by the centrifugal force. Further, the height of the origin of the paraboloid is adjusted until the volume encapsulated in the intersection of paraboloid and shake flask wall matches the desired filling volume. Lastly, it should be noted, that the simplified model uses the same basic shake flask geometry as shown in Fig. 2-2A, where a sharp transition between the lower torus and upper cone occurs.

2.2.6 Calculation of volumetric power input from CFD simulations

To calculate the volumetric power input from CFD simulations, the relationship to the energy dissipation rate was used:

$$\frac{P}{V_L} = \varepsilon \cdot \rho \qquad \text{Eq. 20}$$

where P, V_L and ε are the power input in W, the liquid volume in m^3 and the energy dissipation rate in W/kg. This approach has been used before for the simulation of shaken system in general[45–47] and shake flasks specifically[41]. The total energy dissipation consists of the dissipation of the mean flow and dissipation caused by the turbulence. The energy dissipation of the mean flow can be calculated according to:

$$\varepsilon_m = \frac{\eta}{\rho} \|\mathbf{S}\|^2 \qquad \text{Eq. 21}$$

The turbulent energy dissipation can be taken from the conservation equation of turbulent kinetic energy (Eq. 9):

$$\varepsilon_t = \beta^* k\omega \qquad \text{Eq. 22}$$

Hence, the energy dissipation rate for the entire liquid volume can be calculated as follows:

$$\varepsilon = \frac{\int_{V_L} \left(\frac{\eta}{\rho} \cdot \|\mathbf{S}\|^2 + \beta^* \omega k \right) \cdot dV_L}{V_L} \qquad \text{Eq. 23}$$

It should be noted, that the liquid volume for a specific cell i in Eq. 23 must be calculated according to the VOF model as:

$$V_{L,i} = V_i \cdot \alpha_{L,i} \qquad \text{Eq. 24}$$

where $V_{L,i}$ V_i and $\alpha_{L,i}$ are the liquid volume, total cell volume and liquid volume fraction of cell i.

2.2.7 Calculation of the phase number

The phase number is calculated according to Büchs et al. as follows[4]:

$$Ph = \frac{d_0}{d} \cdot (1 + 3 \cdot \log_{10}(Re_{film})) \qquad \text{Eq. 25}$$

where Ph and Re_{film} are the phase number and Reynolds film number. The Reynolds film number is given as:

$$Re_{film} = Re \cdot \frac{\pi}{2} \cdot \left(1 - \sqrt{1 - \frac{4}{\pi} \cdot \left(\frac{V_L^{\frac{1}{3}}}{d} \right)^2} \right)^2 \quad \text{Eq. 26}$$

2.2.8 Volumetric power input correlation

Volumetric power inputs for shake flasks can be calculated from the correlation of the modified Newton number (Ne′) and Reynolds number (Re)[3] by Büchs et al.[4]:

$$Ne' = 70 \cdot Re^{-1} + 25 \cdot Re^{-0.6} + 1.5 \cdot Re^{-0.2} \quad \text{Eq. 27}$$

where the Reynolds number [-] and modified Newton number [-] are given as follows:

$$Ne' = \frac{P}{\rho \cdot n^3 \cdot d^4 \cdot V_L^{\frac{1}{3}}} \quad \text{Eq. 28}$$

$$Re = \frac{\rho \cdot n \cdot d^2}{\eta} \quad \text{Eq. 29}$$

where n, d and VL are the shaking frequency, the largest inner flask diameter and the filling volume. Büchs et al.[3,4] derived this correlation of Reynolds and modified Newton number from volumetric power inputs determined experimentally at a variety of shaking conditions for 100 to 2000 mL shake flasks. The derived correlation includes only experiments, which were deemed to be in-phase by Büchs et al., based on a critical phase number of 1.26.

2.2.9 Diffusion coefficient for small molecules

The diffusion coefficient is necessary to calculate the k_La value. For the calculation of the diffusion coefficient D_L, the Stokes-Einstein Gierer-Wiertz estimation is used[76]. It is an extension of the Stokes-Einstein equation, which is the ratio of thermal energy and friction forces and can be given for spherical molecules as follows:

$$D_L = \frac{k_B \cdot T}{6 \cdot \pi \cdot \eta \cdot r_M} \quad \text{Eq. 30}$$

where k_B is the Boltzmann constant, T the temperature, η the dynamic viscosity and r_M the molecule radius. This equation follows the assumption of a particle randomly moving through

a continuous medium. However, for the traversal of small molecules, i.e., gases the assumption of a continuous medium does not hold. Instead, the physical interactions of traversing small molecule and molecules of the liquid phase, moving randomly in space, should be considered. The interaction of molecules can be expressed as a modification of the friction forces in the standard Stokes-Einstein equation. Gierer and Wirtz modelled this behavior as the correction factor f_{GW}[76]:

$$f_{GW} = \left(\frac{3\beta}{2} + \frac{1}{1+\beta}\right)^{-1} \quad \text{Eq. 31}$$

where β is the ratio of radii of the solute and solvent. Applying the assumption of hard spheres, Evans et al. estimate the radii of solute and solvent based on the molecular weights as follows[76]:

$$r_M = \sqrt[3]{\frac{3 \cdot MW}{4 \cdot \pi \cdot \rho_{eff} \cdot N_A}} \quad \text{Eq. 32}$$

where MW is the molecular weight, ρ_{eff} the effective density and N_A Avogadro's constant. Gierer and Wirtz give an effective density of 619 kg/m^{-3}, which they obtained by fitting measurement data for 109 combinations of 44 solutes and 5 solvents[76]. Combining Eq. 30, Eq. 31 and Eq. 32 yields the following equation for the diffusion coefficient:

$$D_L = \frac{k_B \cdot T \cdot \left(\frac{3 \cdot \sqrt[3]{\frac{MW_{solute}}{MW_{solvent}}}}{2} + \frac{1}{1+\sqrt[3]{\frac{MW_{solute}}{MW_{solvent}}}}\right)}{6 \cdot \pi \cdot \eta \cdot \sqrt[3]{\frac{3 \cdot MW_{solute}}{4 \cdot \pi \cdot \rho_{eff} \cdot N_A}}} \quad \text{Eq. 33}$$

2.2.10 Calculation of the k_La value from CFD simulations

The k_La value consists of the mass transfer coefficient k_L and the specific surface area a. In this work the eddy cell model by Lamont and Scott was used to calculate the k_L value for the CFD simulations[77]. Similar to the calculation of the volumetric power input, the model is based on the energy dissipation rate (see Eq. 23) and is given as follows:

$$k_L = 0.4 \cdot \sqrt{D_L} \left(\frac{\varepsilon}{\nu}\right)^{\frac{1}{4}} \quad \text{Eq. 34}$$

where D_L is the diffusion coefficient (see Eq. 33), ε the energy dissipation rate (see Eq. 23) and ν the kinematic viscosity. The specific surface area a of a mesh cell *i* in the CFD model can be approximated as the magnitude of the gradient of the volume fraction α of that cell[46,78]:

$$a_i = |\nabla \alpha_i| \quad \text{Eq. 35}$$

The k_La value was then calculated on a per cell basis and integrated over the entirety of the CFD model as follows:

$$k_L a = \frac{\int_V k_{L,i} \cdot a_i \cdot dV}{V} \quad \text{Eq. 36}$$

2.2.11 Correlation for k_La values in shake flask experiments

The correlation from Henzler and Schedel describes the k_La value in shake flask experiments as follows[28]:

$$k_L a = 0.5 \cdot d^{\left(\frac{73}{36}\right)} \cdot n \cdot d_0^{\left(\frac{1}{4}\right)} \cdot V_L^{\left(-\frac{8}{9}\right)} \cdot \nu^{\left(-\frac{13}{54}\right)} \cdot g^{\left(-\frac{7}{54}\right)} \cdot D_L^{\left(\frac{1}{2}\right)} \quad \text{Eq. 37}$$

where d, n, d_0, V_L, ν, g and D_L are the largest inner flask diameter, shaking frequency, shaking diameter, filling volume, kinematic viscosity, gravitational acceleration and diffusion coefficient.

2.2.12 Approximation of the shear-thinning behavior as a power-law fluid

The simplest and most common approach to approximate the non-Newtonian flow behavior of shear-thinning fluids is the power-law model, also routinely referred to as the Ostwald-de Waele relationship. The power-law model can be given as the relationship of shear stress and shear rate as follows:

$$\tau = K \cdot \gamma^m \quad \text{Eq. 38}$$

where τ, γ, K and m are the shear stress, shear rate, flow consistency index and flow behavior index. The power-law model can also be given as the relationship of viscosity and shear rate as follows:

$$\eta_{eff} = K \cdot \gamma^{m-1} \quad \text{Eq. 39}$$

where η_{eff} is the effective viscosity for the given shear rate.

2.2.13 Calculation of the shear rate from CFD simulations

The shear rate for CFD simulations was calculated in two ways. First, as the scalar measure of the strain rate tensor. This is a common approach, utilized in OpenFOAM[79], which is given as follows:

$$\gamma_i = \|\mathbf{S}\| \quad \text{Eq. 40}$$

where γ_i and $\|\mathbf{S}\|$ are the shear rate in mesh cell *i* and the scalar measure of the strain rate tensor. The second approach uses the estimation of average shear stress based on the eigenvalues of the strain rate tensor. Soos et al. give the equation of average shear stress as follows[80]:

$$\tau_L = 2.5 \cdot \eta \cdot \lambda_1(\mathbf{S}) \quad \text{Eq. 41}$$

where τ_L is the average shear stress, η the dynamic viscosity and $\lambda_1(\mathbf{S})$ the largest, positive eigenvalue of the strain rate tensor **S**. Under the assumption of Newtonian flow behavior, the shear rate for a mesh cell *i* can be easily calculated from the shear stress, leading to the following equation:

$$\gamma_i = 2.5 \cdot \lambda_1(\mathbf{S_i}) \quad \text{Eq. 42}$$

where γ_i and $\mathbf{S}_i$ are the shear rate and strain rate tensor in mesh cell *i.* For both approaches the shear rates per cell are then integrated over the liquid volume of the CFD model as follows:

$$\gamma = \frac{\int_{V_L} \gamma_i \cdot \alpha_i \cdot dV_L}{V_L} \quad \text{Eq. 43}$$

Under the assumption of non-Newtonian flow, the equation for shear stress (Eq. 41) cannot directly be transformed to an estimation of the shear rate (Eq. 42). Instead, the shear stress would need to be calculated for an intermediate viscosity, depending on some intermediate shear rate as follows:

$$\tau_{L,inter} = 2.5 \cdot \eta_{inter}(\gamma_{inter}) \cdot \lambda_1(\mathbf{S}) \quad \text{Eq. 44}$$

where $\tau_{L,inter}$, η_{inter} and γ_{inter} are the intermediate shear stress, viscosity and shear rate. An approximation of the non-Newtonian fluid with, for example, a power-law approach (see Eq. 38) would, after rearranging, enable the calculation of the shear rate as follows:

$$\gamma_{inter,new} = \left(\frac{\tau_{L,inter}}{K}\right)^{\frac{1}{m}} \quad \text{Eq. 45}$$

where K and m are the flow consistency index and flow behavior index from the power-law. Hence, the calculation of the shear rate would have to be performed iteratively in the CFD, when non-Newtonian fluids are simulated.

2.2.14 Correlation for effective shear rates in shake flask experiments

The correlation for effective shear rates by Giese et al. is given as follows[7]:

$$\gamma = 2.06^{\frac{1}{m+1}} \cdot \left(\frac{P}{V_L \cdot K}\right)^{\frac{1}{m+1}} \cdot \left(\frac{V_L^{\frac{1}{3}}}{d}\right)^{\frac{-0.331}{m+1}} \quad \text{Eq. 46}$$

2.2.15 Experimental data sets

Experimental data for the comparison of liquid contact lines was provided by Azizan et al.[5,6]. The data set includes shaking frequencies from 150 to 450 rpm, filling volumes from 15 to 40 mL, at a shaking diameter of 2.5 cm for a viscosity of 0.89 to 80 mPa·s. The data set form Büchs et al. contains volumetric power inputs for a broad range of shaking conditions, including different shake flasks sizes, shaking frequencies, shaking diameters, filling volumes and viscosities[3,4]. A subset of the data set for 250 mL shake flasks, including shaking frequencies from 180 to 380 rpm, filling volumes of 25 and 40 mL at a shaking diameter of 2.5 cm for a viscosity of 1 to 200 mPa·s, was used for the comparison to the CFD model.

2.3 Results and Discussion

2.3.1 Liquid contact lines

In the initial phase of model tuning, the liquid contact lines (Fig. 2-1, red dashed lines) extracted from the CFD model and simplified mechanistic model[74], were compared at 25 and 40 mL filling volumes and shaking frequencies of 350 (Fig. 2-4A) and 250 rpm (Fig. 2-4B). The liquid contact lines are not depicted in a 3D-representation, as illustrated in Fig. 2-1, but rather in a 2D-representation by rotating around the central z-axis of the shake flask (Fig. 2-1C). The height of the contact line over one rotation is depicted. The 3D-representations are not depicted because they quickly become incomprehensible for the comparison between CFD and experiments. An example of a 3D-representation is included in the supplement (see Appendix 3).

Due to the fact that the simplified mechanistic model completely disregards the influence of viscous forces on the liquid distribution, it was necessary to generate comparable conditions in the CFD model. Since entirely removing viscous forces from the CFD model is non-trivial, a viscosity of $1 \cdot 10^{-27}$ Pa·s was chosen for the comparison instead. It should be noted that the numerical diffusion, due to the discretization of the convective momentum transport, introduces an additional diffusive momentum transport. The overall diffusive momentum transport should, however, remain sufficiently low for a comparison to the simplified mechanistic model. Excluding viscous forces results in a completely symmetric liquid contact line, as can be seen in Fig. 2-4A and B for the simplified mechanistic model[74] and the CFD model, respectively. In addition, the bulk liquid and maximal liquid height are perfectly aligned with the direction of the centrifugal force, indicated by the vertical dashed black line in Fig. 2-4. Given that viscous forces were not entirely eliminated from the CFD simulations, small deviations were anticipated. Yet, liquid contact lines for the CFD remain highly symmetrical, only showing slight deviations in the leading edge (left flank of the contact line) for both filling volumes at 350 rpm and 40 mL at 250 rpm. At a filling volume of 25 mL and a shaking frequency of 250 rpm (Fig. 2-4B), the largest discrepancy between the CFD and the mechanistic model can be seen. The leading edge extracted from the CFD model is approximately 15° behind the leading edge of the simplified model, resulting in a minor asymmetry in the CFD calculation's contact line. In Fig. 2-4C the simplified mechanistic model is compared to a CFD simulation with a realistic, waterlike viscosity of 0.69 mPa·s at the previous shaking parameters of 40 mL and 250 rpm. This example illustrates the effect of viscous forces on the observed liquid contact line. The entire bulk liquid and its maximal liquid height are moved against the shaking motion and positioned about 15°

after the direction of the centrifugal force. This shift occurs along the entire leading edge of the liquid contact line, reaching a maximum of nearly 30° at the liquid contact line's widest point. As discussed, this shift of the leading edge of the liquid contact line against the shaking direction has been observed previously[3,4,64,66,67] and was recorded by Azizan et al. in their liquid distribution data [5,6]. The observed shift with increasing viscosity may also account for the small, yet noticeable differences between the CFD and simplified mechanistic model in Fig. 2-4A and B. In addition, the effects of viscous forces on the trailing liquid (right flank of the contact line) are visible in the CFD calculation in Fig. 2-4C. A clear, extended tail from approximately 300° onward, with a visible shoulder at a liquid height of about 15 mm can be seen. In Fig. 2-4 the shake flask is modelled as a quarter torus for the lower part and a cone for the upper part, resulting in a sharp transition between the lower and upper part of the shake flask at a height of 14.5 mm (refer to Fig. 2-2A), which is close in height to the extended tail. Consequently, the extended tail after 300° in the CFD calculation is most likely formed due to this sharp transition. The geometric model of the shake flask as a quarter torus was initially chosen by Büchs et al.[74] for the simplified mechanistic model and replicated in the CFD accordingly.

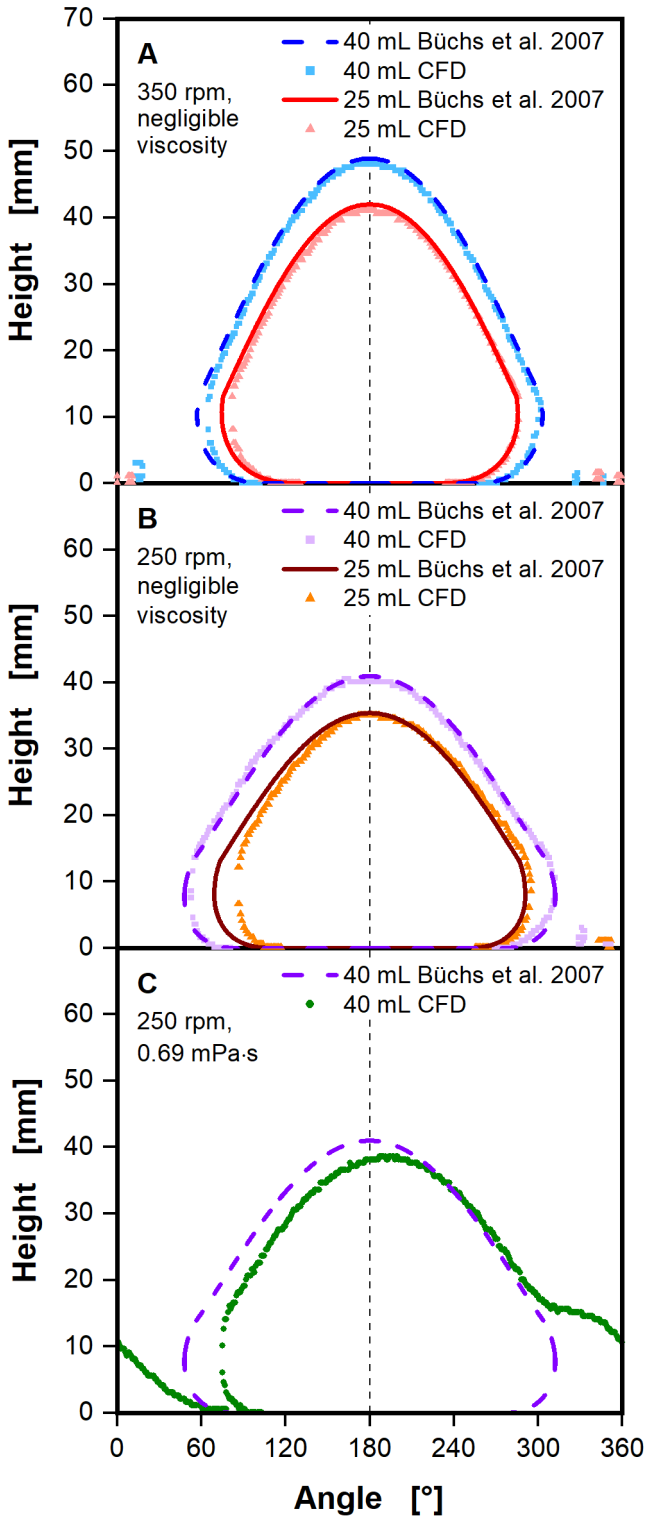

Fig. 2-4: Liquid contact line calculated by the CFD model, compared to the simplified mechanistic model from Büchs et al. assuming negligible viscosity[74].

The height of the liquid contact line is shown in mm, viewed from the center of the shake flask, rotating around the z-axis (see Fig. 2-1C). For CFD results, the first wall layer, closest to the flask wall is sampled. As indicated by the vertical dashed black line in (A), (B) and (C) the centrifugal force is pointing in the direction of 180°. Calculations of the liquid contact line with the simplified mechanistic model by Büchs et al. entirely neglect viscosity[74]. For comparison, a vanishingly small viscosity was chosen for the CFD model in (A) and (B). In (C) a realistic waterlike viscosity was simulated with the CFD model instead. Simulated conditions: Viscosity (η) = $1 \cdot 10^{-10}$ Pa·s (A, B) and 0.69 mPa·s (C), shaking diameter (d_0)

= 2.5 cm, filling volume (V_L) = 25 mL and 40 mL, shaking frequency (n) = 350 rpm (A) and 250 rpm (B, C), surface tension (σ) = 70 mN/m, contact angle (Θ) = 20°, temperature (T) = 37°C (C)

Although the simplified mechanistic model verifies the CFD model's accuracy for negligible viscosity, it cannot validate the CFD model for realistic viscosities. Consequently, CFD simulations with viscosities comparable to water and higher must be compared to experimental data. In Fig. 2-5, the experimental data from Azizan et al.[5,6] is compared with CFD simulations at waterlike viscosity. In a first attempt, the CFD simulation from Fig. 2C was compared to the experimental data. This simplified approximation of the real shake flask geometry as a quarter torus, however, produced unsatisfactory results. Although, the liquid contact line of the CFD simulation with a quarter torus geometry in Fig. 2-5 closely matches the experimental data in overall shape and position, the maximal liquid height and tail from 180° onward are underestimated by up to 15 mm by the CFD model. Notably, the shoulder in the tail region at roughly 300° is not observed in the experimental data in Fig. 2-5. Recall that this shoulder in the tail region appears at the height of the intersection of the quarter torus and cone of the geometric model of the shake flask (see Fig. 2-2A). Therefore, the sharp transition at the intersection of quarter torus and cone was suspected to be at fault for the poor CFD model performance in the tail region, when compared to the experimental data. Hence, the modelled shake flask geometry was adjusted. The lower torus part was extended past a quarter torus, until it was in line with the slope of the cone part (see Fig. 2-2B). This approach leads to a smooth transition between the torus and cone and much more closely resembles the geometry of the real shake flask (see Appendix 2). Changing the geometry to a smooth transition, eliminates the issues in the tail region and maximal liquid to a large extent. The liquid contact line nearly coincides with the experimentally determined liquid contact line and the maximal liquid height of 42 mm. Solely, a minor difference in the tail of the liquid contact line can be seen. Notably, a plateau in the tail region of the CFD simulations is no longer present. In conclusion, the smooth transition replicates the real shake flask geometry (see Appendix 2) significantly better and was crucial to the satisfactory performance of the CFD model. In light of this, the geometry with a smooth transition is used in all subsequent CFD simulations. Modification of the simplified mechanistic model to use the smooth transition shake flask model should be considered in the future.

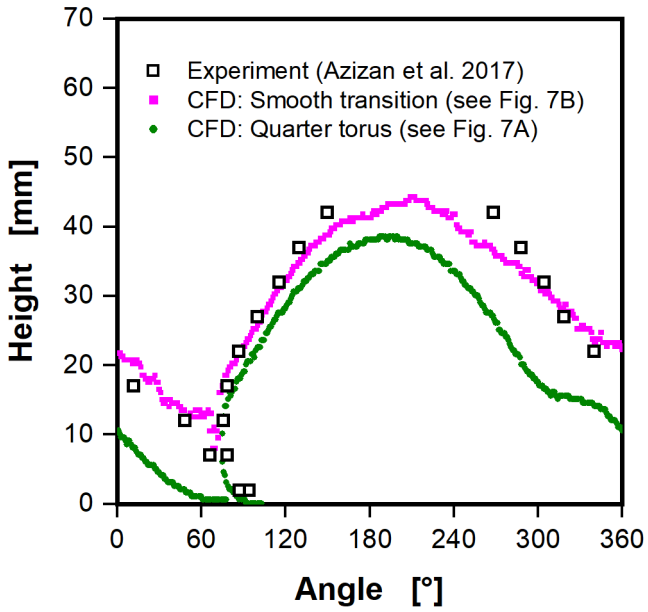

Fig. 2-5: Influence of the assumed shake flask geometry on the liquid contact line.

The liquid contact line is shown in mm, viewed from the center of the shake flask, rotating around the z-axis (see Fig. 2-1C). The underlying shake flasks geometry is either modeled as a quarter torus with an added cone for the upper part or with a smooth transition between torus and cone segment (see Fig. 2-2A and B, respectively). CFD results are compared with experimental data by Azizan et al.[5,6]. Simulated conditions: Viscosity (η) = 0.69 mPa·s, shaking diameter (d_0) = 2.5 cm, filling volume (V_L) = 40 mL, shaking frequency (n) = 250 rpm, surface tension (σ) = 70 mN/m, contact angle (Θ) = 20°, temperature (T) = 37°C

Following the selection of a shake flask geometry, the effects of an increase in viscosity on CFD model performance was investigated. Consequently, Fig. 2-6 depicts the results of a CFD simulation at an elevated viscosity of 16.7 mPa·s. Increasing the viscosity from waterlike viscosity to 16.7 mPa·s results in a reduction of the Reynolds number from roughly 31.000 to roughly 1.600. Fig. 2-6A shows the three-dimensional liquid distribution computed by the CFD model. In addition to the leading edge of the bulk liquid, a liquid film on the inner flask wall over the entire circumference up to the maximal liquid height is visible. Hence, the liquid contact line of the CFD simulation cannot be extracted directly at the flask wall (normal distance of 50 µm), as done for Fig. 2-4 and Fig. 2-5. Instead, the liquid contact line is extracted multiple times, increasing the normal distance between sampled cells and the shake flask wall with each extraction (compare Fig. 2-3A). Fig. 2-6B depicts liquid contact lines at these normal distances. For small normal distances between 50 and 250 µm, almost constant liquid heights between 35 and 37 mm are extracted, representing the liquid film over the entire flask circumference. In contrast, the large normal distances of 650, 850 and 1050 µm surpass the liquid film and, therefore, represent the shape of the bulk liquid. Liquid contact lines at the high normal distances align well with the experimental data in the leading edge and overall position of the

bulk liquid. Nonetheless, variations in the contact line can be observed in the tail region. These disparities, however, are not surprising. The leading edge is characterized by a stark difference in the liquid thickness normal to the wall, as evident in Fig. 2-6A. In contrast, it is challenging to define the limits of the tail region, due to the seamless transition between the tail region of the bulk liquid and the liquid film. Consequently, precisely defining the tail region is somewhat arbitrary and much more error-prone, compared to the detection of the leading edge. This is the simple, physical reality of the flow in shake flasks and affects the detection of the tail region in experiments and CFD alike.

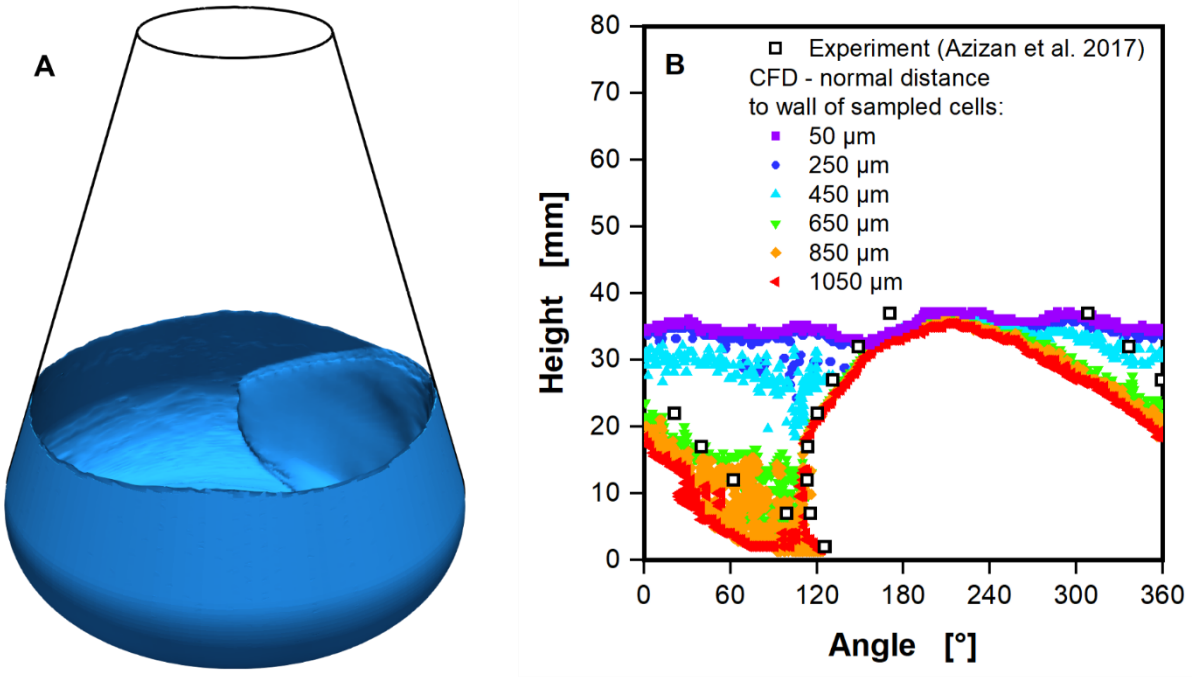

Fig. 2-6: Impact of the liquid film on the extraction of the liquid contact line from CFD calculations at elevated viscosity.

3D image of the calculated CFD case, showing a liquid film at the inner flask wall along the entire circumference of the shake flask, up to the maximal liquid height. (B) Liquid contact lines from CFD calculations, extracted by numerically sampling at multiple distances normal to the shake flask wall (as indicated in Fig. 2-3A), aiming to exclude the resolved liquid film, are shown. Results for the liquid contact line from CFD are compared to experimental data by Azizan et al.[5,6]. Simulated conditions: Viscosity (η) = 16.7 mPa·s, shaking diameter (d_0) = 2.5 cm, filling volume (V_L) = 40 mL, shaking frequency (n) = 250 rpm, surface tension (σ) = 70 mN/m, contact angle (Θ) = 20°, temperature (T) = 25°C

Concerning the observed liquid films in the CFD simulations, it should be noted that the formation of such liquid films in shake flask experiments and its importance for the gas-liquid mass transfer has already been discussed in the literature[1,2,23,81]. Such liquid films can also be seen in photographs of shake flask experiments in the supplementary data (Appendix 4B, Appendix 5B and Appendix 6B). [52–55]Hermann conducted approximate measurements of the

liquid film thickness in shake flasks (see Appendix 7, Appendix 8 and Appendix 9)[82]. He used a measurement apparatus comparable to the one from Azizan et al. for liquid contact lines[6], but with a single sensor at a height of 20.6 mm. Hermann assessed liquid film thicknesses of 50 and 800 µm at 1 and 35 mPa·s, respectively (see Appendix 9). Comparatively, the extraction of liquid contact lines at numerous distances normal to the flask wall in the CFD model reveals the liquid film thickness to be between 450 and 650 µm (Fig. 2-6B), being slightly thinner near the maximal liquid height due to gravity. Taking into account the lower viscosity of 16.7 mPa·s in the CFD model, the results are consistent. In CFD simulations with a viscosity comparable to water, however, no liquid film is observed, as shown in Fig. 2-5. This is most likely caused by an insufficient mesh resolution for liquid films with an expected thickness of about 50 µm. The thinnest wall layer of mesh cells with an approximate edge length of 140 µm perpendicular to the wall (see Fig. 8A) are likely too large to resolve these thin liquid films. Resolving the thin liquid film for waterlike viscosity might be possible with a finer mesh, an adaptively refined mesh, where mesh cells are refined during CFD computation or with a Direct Numerical Simulation. All these approaches, however, lead to significantly longer computation times, with extreme computation times in the case of Direct Numerical Simulations. The comparison between the CFD results and the experimental liquid contact lines from Azizan et al.[5,6] does, generally, not require consideration of the liquid film. Therefore, the faster computation time of the fixed meshing is preferable and was chosen for all simulations in this work. Additionally, the liquid film contributes very little to the overall volumetric power input, as can be seen later on, when volumetric power inputs form model and correlation are compared.

Due to the possibility of small underestimations of the maximal liquid height in the CFD simulations in Fig. 2-5 and Fig. 2-6B, some of the material parameters (taken from VDI Heat Atlas[73]) were selected for a parameter study prior to simulating a larger data set of shaking conditions. Surface tension, contact angle and the slope of the upper cone part of the shake flask geometry were selected, as variables that could potentially affect the maximal liquid height. Adjustment of the parameters were small and on a realistic scale, and unidirectional, favoring potentially greater maximum liquid heights. Thus, a 10 % decrease in surface tension, a 15° decrease in contact angle, and a 1° decrease in the slope of the cone were simulated. Resulting liquid contact lines are shown in the supplementary data in Appendix 10, Appendix 11 and Appendix 12. No appreciable differences in the overall liquid contact line and maximal liquid height were observed for any of the three adjustments. Consequently, the standard parameters from the previous simulations were used for a larger set of CFD simulations.

In order to thoroughly validate the model against the experimental data provided by Azizan et al.[5,6], a larger set of CFD simulations were conducted following the optimization of the model. For the larger set of CFD simulations, nine combinations of shaking conditions were selected, including shaking frequencies between 150 and 450 rpm and filling volumes between 15 and 40 mL. For each of the nine combinations, experimental data on the liquid distribution by Azizan et al.[5,6] is available. CFD simulations were performed for a waterlike viscosity of 0.89 mPa·s and an elevated viscosity of 16.7 mPa·s. A subset of four of the shaking conditions for both viscosities are shown in Fig. 2-7. Fig. 2-7A, C, E and G depict the results at the waterlike viscosity, while Fig. 2-7B, D, F and H depict the results at the moderate viscosity of 16.7 mPa·s. The extraction of liquid contact lines at multiple normal distances described for Fig. 2-6 has been performed not only for the moderate viscosity, but also for waterlike viscosity. CFD simulations for Fig. 2-7A and B have already been discussed and are depicted in Fig. 2-5 and Fig. 2-6. The remaining subfigures depict the results for a filling volume of 15 mL at shaking frequencies of 150 rpm (Fig. 2-7C and D), 250 rpm (Fig. 2-7E and F) and 450 rpm (Fig. 2-7G and H). CFD model performance at these shaking conditions is comparable to the ones already discussed. Overall shape and position of the leading edge align nicely between experiment and CFD simulation, as long as liquid films are excluded by analyzing the larger normal distances to the shake flask wall. Only for shaking frequencies of 250 and 450 rpm at a moderate viscosity of 16.7 mPa·s, as depicted in Fig. 2-7F and H, are there notable deviations in the liquid contact line between experimental data and CFD model. In both cases, the shape of the leading edge appears to be the same, yet, occurs approximately 15° later in the CFD model than the experimental data suggests. Notably, the CFD model accurately predicts the shift of the liquid against the shaking direction as viscosity increases. In some of the simulated conditions, the extracted maximum liquid heights may be slightly lower than the experimentally determined values. This affects waterlike viscosity (Fig. 2-7E) and moderate viscosity (Fig. 2-7D and H) alike, showing differences of up to 3 mm between the two. Taking into consideration the already discussed issues of defining the tail region in the context of Fig. 2-6B, the tail region is suitably matched by the CFD simulations. This holds true especially for cases with a waterlike viscosity.

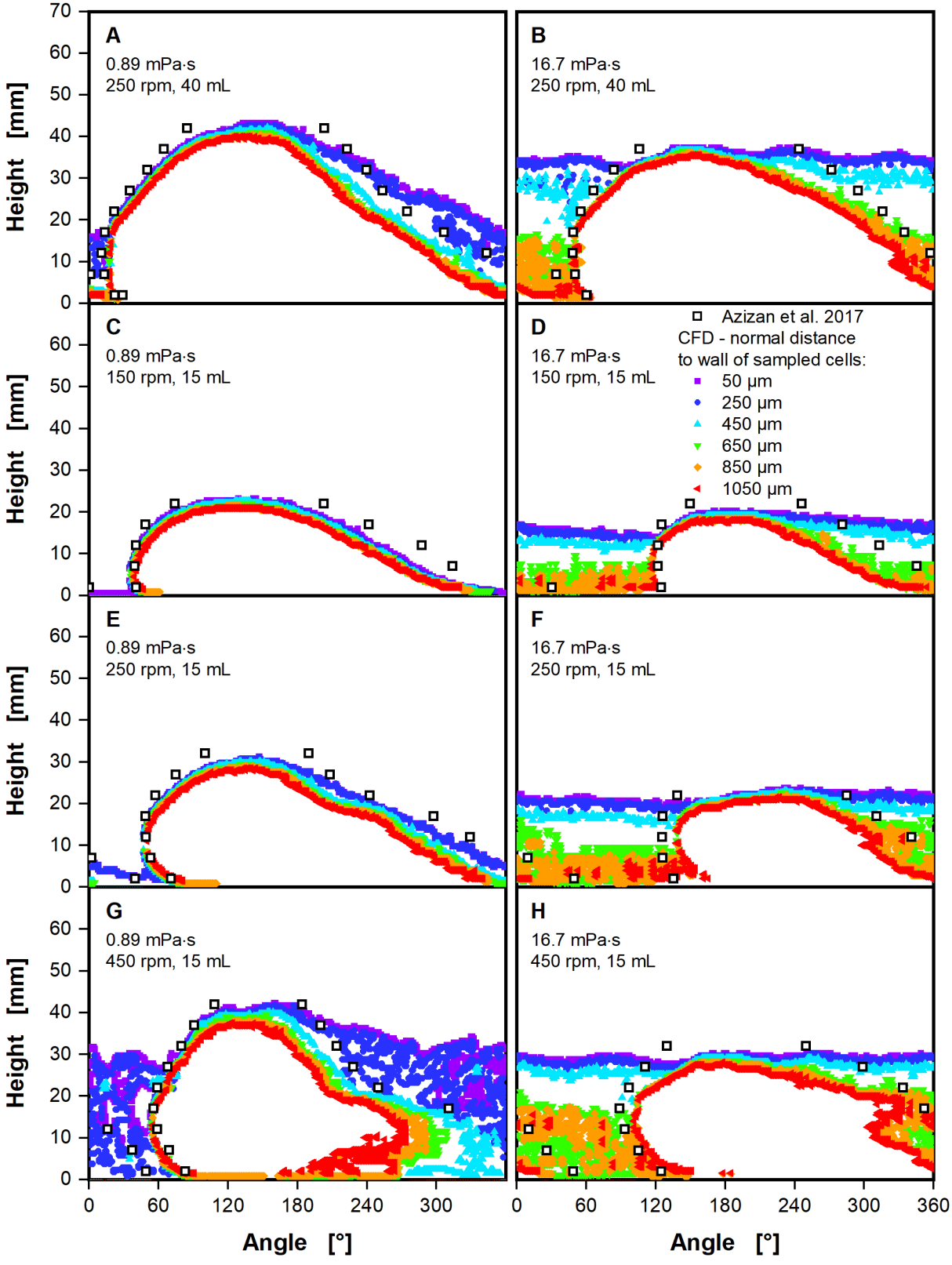

Fig. 2-7: Liquid contact lines calculated by the CFD model, compared to experimental data by Azizan et al.[5,6] for a variety of shaking conditions.

The liquid contact lines are shown in mm, viewed from the center of the shake flask, rotating around the z-axis (see Fig. 2-1C). Liquid contact lines from CFD were extracted at multiple distances from 50 to 1050 µm normal to the shake flask wall (as indicated in Fig. 2-3A) to exclude the liquid film (see Fig. 2-6A). Simulated conditions: Shaking diameter (d_0) = 2.5 cm, surface tension (σ) = 70 mN/m, contact angle (Θ) = 20°, temperature (T) = 25°C. (A, C, E, G) Cases with a low viscosity of 0.89 mPa·s. (B, D,

F, H) Cases with a higher viscosity of 16.7 mPa·s. (A+B) filling volume (V_L) = 40 mL, shaking frequency (n) = 250 rpm. (C+D) filling volume (V_L) = 15 mL, shaking frequency (n) = 250 rpm. (E+F) filling volume (V_L) = 15 mL, shaking frequency (n) = 150 rpm. (G+H) filling volume (V_L) = 15 mL, shaking frequency (n) = 450 rpm

Curiously, the tail region no longer exhibits a consistent slope at high shaking frequencies. At 450 rpm at waterlike viscosity (Fig. 2-7G) the liquid height remains almost constant at 20 mm from 200° onwards, only declining slightly. Fig. 2-7H depicts the formation of a spike-like feature at 450 rpm for the moderate viscosity at a similar height and position in the tail region. As previously discussed in the context of Fig. 2-6, the extraction of liquid contact lines at multiple distances from the flask wall in the CFD model can be used to estimate the thickness of formed liquid films. Contrary to previous findings, a partially formed liquid film with a thickness of approximately 250 µm can be observed in CFD cases with waterlike viscosity, and at the highest shaking frequency of 450 rpm (Fig. 2-7G). For the moderate viscosity of 16.7 mPa·s, a film thickness ≥500 µm is found in the CFD simulations. As previously mentioned, Hermann provides approximations for the liquid film thickness in shake flasks[82]. For viscosities of 1 and 35 mPa·s, a liquid film thickness of 50 and roughly 800 µm, respectively, were found, confirming the CFD model results (see Appendix 9).

Following the validation at waterlike and moderate viscosity, the liquid distribution was also analyzed near and at out-of-phase operating conditions. Fig. 2-8 depicts a comparison of the liquid contact lines at about 80 mPa·s, for a variety of shaking conditions, including shaking frequencies between 150 and 450 rpm and filling volumes between 15 and 40 mL. CFD simulations were conducted for Newtonian fluids, i.e., at a constant viscosity. The polyvinylpyrrolidone, used by Azizan et al. for the evaluation of the experimental liquid contact lines, however, shows slight shear-thinning behavior, i.e., a reduction in viscosity with increasing shear rates[5,6]. Prior to performing the CFD simulations, effective shear rates for the given shaking conditions were calculated according to Giese et al.[7] and used to determine constant viscosities for the simulations. This leads to small variations in the viscosity around 80 mPa·s for the CFD simulations in Fig. 2-8. The simulations in Fig. 2-8 are ordered from highest to lowest phase number, crossing both the critical phase number by Büchs et al. of 1.26[4] and by Azizan et al. of 0.91[5].

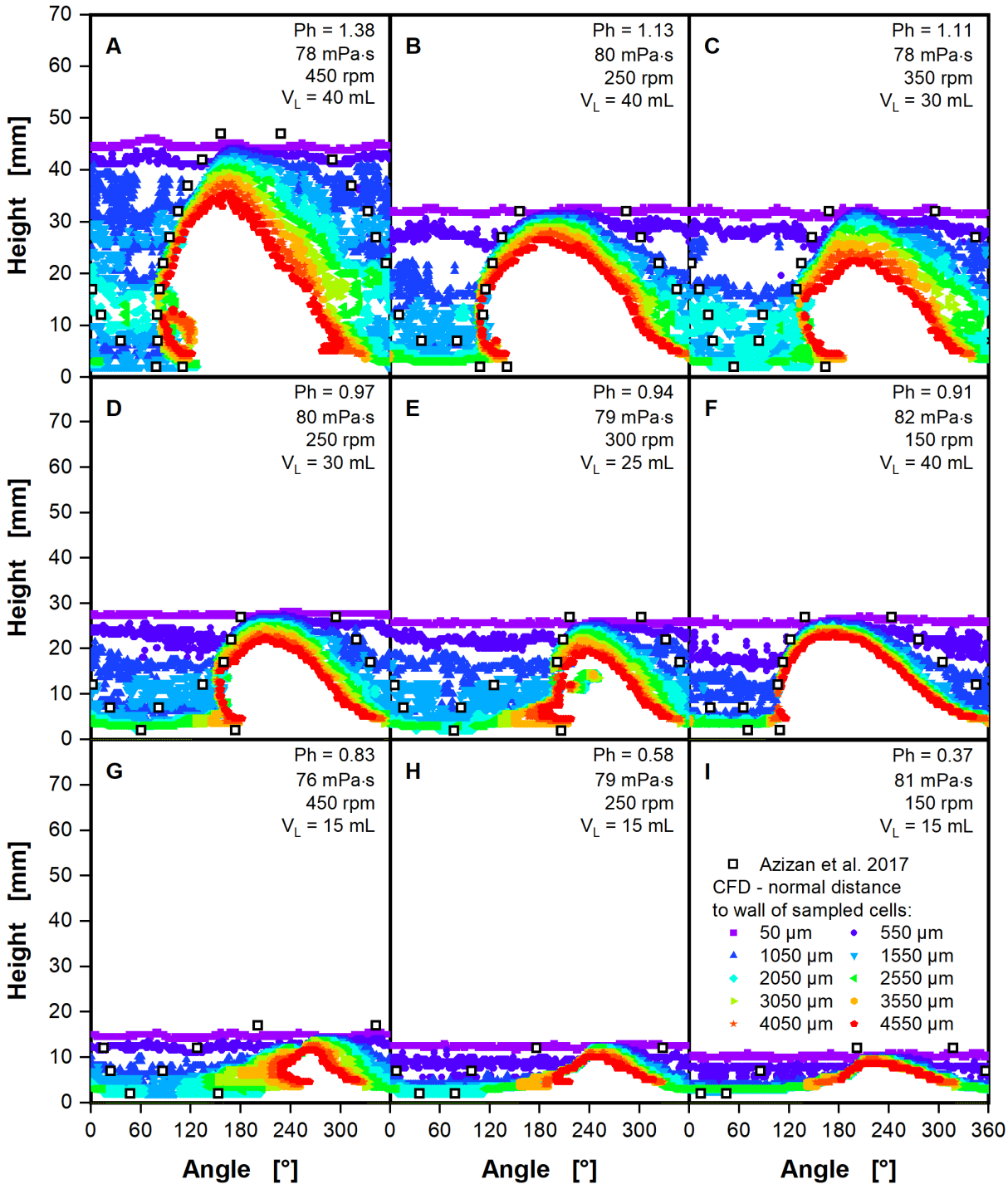

Fig. 2-8: Liquid contact lines extracted from the CFD model, compared to experimental data (open black squares) by Azizan et al.[5,6]

The liquid contact lines are shown in mm, viewed from the center of the shake flask, rotating around the z-axis (see Fig. 2-1). To exclude the liquid film, liquid contact lines from the CFD simulations were extracted at multiple distances from 50 to 4550 µm normal to the shake flask wall (as indicated in Fig. 2-3A). Simulated conditions are ordered from highest to lowest phase number (Eq. 25). The polyvinylpyrrolidone, used by Azizan et al. shows shear-thinning[5,6]. Hence, Newtonian viscosities for CFD simulations were determined by calculating the effective shear rate according to Giese et al.[7] (Eq. 46) and then estimating the viscosity with the power law for non-Newtonian fluids (Eq. 39). Simulated conditions: Shaking diameter (d_0) = 25 mm, surface tension (σ) = 70 mN/m, contact angle (Θ) = 20°, temperature (T) = 20°C, consistency factor (K) = 104 mPa·s and flow behavior index (m) = 0.956 according to Azizan et al.[5,6].

Due to the occurrence of liquid films in shake flasks, liquid contact lines were not only extracted directly at the flask wall, but at multiple, iteratively increasing normal distances to the shake flask wall (see Fig. 2-6). The smallest, considered normal distance of 50 µm ensures the extraction of the liquid contact line from the first wall layer of the generated mesh. This first layer of cells in the mesh has a width of 140 µm. This normal distance is increased by 500 µm in each iteration, until 4550 µm are reached. For the lowest normal distance to the flask wall of 50 µm (violet square), a constant liquid height over the entire flask circumference can be observed for every depicted case, deviating only marginally from the maximal liquid height of the experimentally determined liquid contact lines. Liquid contact lines at the larger normal distances from 1550 µm onward (light blue, upside down triangles) reveal the rotating bulk liquid for all depicted cases in Fig. 2-8. The liquid film thickness in the CFD increases from 50 µm (violet square) at the maximal liquid height to 2050 µm (blue-green diamonds) at the base of the shake flask, averaging around 1050 µm (blue triangles). Experimentally evaluated liquid films from Hermann[82], confirm a film thickness of roughly 1000 µm at 100 mPa·s (see Appendix 9).

At the normal distances of 1550 µm (light blue, upside down triangles) and larger, the leading edge of the rotating bulk liquid (left flank) is clearly visible in the CFD simulations in Fig. 2-8A – F. In the leading edge the data points for the offsets from 1550 µm onward are stacked on top of each other, signifying a large difference in the liquid thickness between liquid film and bulk liquid. For the cases in Fig. 2-8A – F the leading edge in the CFD simulation agrees well with the experimentally determined liquid contact lines, deviating a few degrees at most. In the tail region, the data points for all offsets are spread out over a large section of the flask wall, indicating a smooth transition from bulk liquid to liquid film. This complicates a clear distinction into the tail region of the bulk liquid and liquid film, affecting both CFD and experimental values. Yet, as explained above, the liquid film should show a thickness of around 1000 µm. Hence, the edge of the tail region can be roughly defined as the change from the offset of 1550 µm (light blue, upside down triangles) to 1050 µm (blue triangles). This region agrees well with the experimentally determined tail of the rotating bulk liquid in Fig. 2-8A – F. In Fig. 2-8G – I the phase numbers are significantly below the critical phase number of 0.91 by Azizan et al.[5]. Under this critical phase number, a complete collapse of the rotating bulk liquid has been described, which is confirmed by the liquid distribution from CFD and experiments in Fig. 2-8G – I. The maximal liquid height is greatly reduced, compared to the cases in Fig. 2-8A – F, showing only a small wave flowing on the bottom of the shake flask. In summary, the liquid contact lines from the CFD model fit well to the experimental data from Azizan et al.[5,6].

2.3.2 Volumetric power inputs

After confirming that the liquid distribution is correctly simulated in the CFD at low and high viscosity, the model was used to calculate the volumetric power input at a variety of shaking conditions. CFD simulations were first run at filling volumes of 25 and 40 mL, viscosities of 1 and 16 mPa·s, shaking frequencies from 180 to 380 rpm and a shaking diameter of 25 mm, calculating the volumetric power input based on the energy dissipation (Eq. 20 and Eq. 23). Values calculated from the CFD model are compared to experimental data and values calculated based on the Ne′-Re-correlation by Büchs et al.[3,4] (Fig. 2-9). Unfortunately, Büchs et al.[3,4] do not report an experimental error for the determined volumetric power inputs. However, Büchs et al.[3,4] did include a repetition measurement after three months at a filling volume of 10 mL and shaking diameter of 25 mm. The repeated measurements show a maximal deviation of 0.23 kw/m^3 and an average deviation of 0.06 kW/m^3. Triplicates for the experimental data at a viscosity of 1 mPa·s are available at both filling volumes, but not for the higher viscosity of 16 mPa·s, as indicated by the error bars. When comparing only experimental data and correlation values, both from Büchs et al.[3,4], a remarkably small deviation can be seen. It should be noted that in the Ne′ and, therefore, in the Ne′-Re-correlation the shaking diameter was omitted for the sake of simplicity[3,4]. An increase in the shaking diameter, however, leads to an increase in the centrifugal force and greater liquid height and, therefore, an increase in volumetric power input. This increase in the volumetric power input is visible in the experimentally determined volumetric power inputs from Büchs et al.[3,4]. Extending the shaking diameter from 2.5 to 5 cm increased the volumetric power input by roughly 13 % for waterlike and moderate viscosity. This effect is illustrated by a parity plot of the original experimentally determined volumetric power inputs from Büchs et al.[3,4], which is included in the supplement (see Appendix 13). In addition, the effect of the shaking diameter on volumetric power inputs was also observed in our CFD simulations of various shaking diameters (data will be included in a future publication). The low deviation between the experimental data and the correlation in Fig. 2-9 is, therefore, somewhat unexpected.

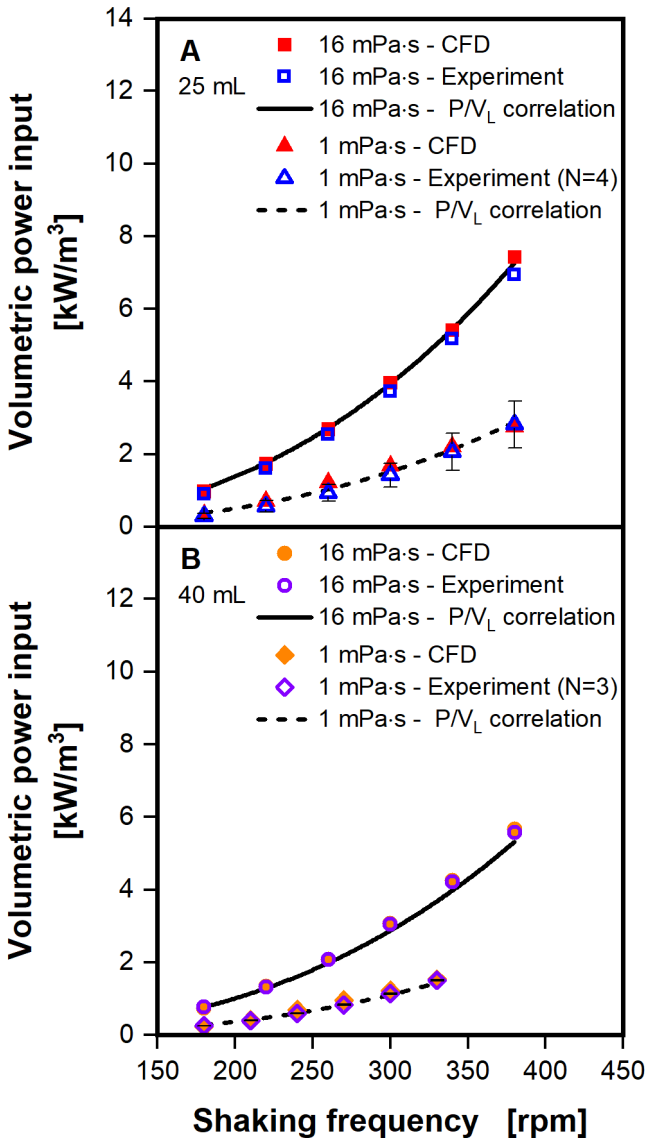

Fig. 2-9: Comparison of volumetric power input obtained from CFD calculations with experimental data and the correlation of Büchs et al.[4].

The volumetric power inputs calculated from CFD utilizing the energy dissipation rate (see Eq. 23) are shown (filled symbols). Results are compared to experimental results (open symbols) and values calculated with the volumetric power input correlation (line and dashed line) from Büchs et al.[4]. Replicates of the experimentally determined volumetric power inputs and corresponding error bars exist only for the low viscosity of 1 mPa·s at 25 (A) and 40 (B) mL. Simulated conditions: Viscosity (η) = 1 mPa·s and 16 mPa·s, shaking diameter (d_0) = 2.5 cm, filling volume (V_L) = 25 mL (A) and 40 mL (B), shaking frequency (n) = 180 – 380 rpm, surface tension (σ) = 70 mN/m, contact angle (Θ) = 20°, temperature (T) = 20°C

Volumetric power inputs, computed based on the CFD model, also align exceptionally well with the experimental data and correlation. CFD, experiment, and correlation differ by a maximum of 0.5 kW/m^3 across all simulated conditions, with an average deviation of 0.01 kW/m^3. As anticipated, the volumetric power input increases as shaking frequency and

viscosity increase, and when filling volume decreases. Note that these trends must only hold true if the out-of-phase phenomenon is avoided[4,5].

As discussed in the context of Fig. 2-6 and Fig. 2-7 the liquid film is not completely resolved by the CFD model for waterlike viscosity, except for the highest shaking frequency of 450 rpm. Nevertheless, the calculated volumetric power inputs are correct, suggesting that the liquid film contributes negligible power to the liquid. This finding is expected, as the energy dissipation is based on the velocity gradients, as it is utilized in the CFD model (Eq. 23 and Eq. 16). In the liquid film, movement is mainly caused by the gravitational force, causing small velocity gradients. Comparably massive velocity gradients are observed in the rotating bulk liquid as it rolls over the shake flask wall. Hence, the bulk liquid is the major contributor to the volumetric power input in shake flask experiments.

Afterwards, the CFD model was used to calculate the volumetric power input at a variety of shaking conditions at higher viscosities, than shown in Fig. 2-9. Conditions were chosen according to already existing, experimental volumetric power input data from Büchs et al.[3,4]. Fig. 2-10 compares the volumetric power input, computed from the CFD model and values derived from volumetric power input correlation (see Eq. 27) and experiment by Büchs et al.[3,4] at a variety of shaking conditions and viscosities. Fig. 2-10 also shows the phase number (see Eq. 25) for the given shaking conditions.

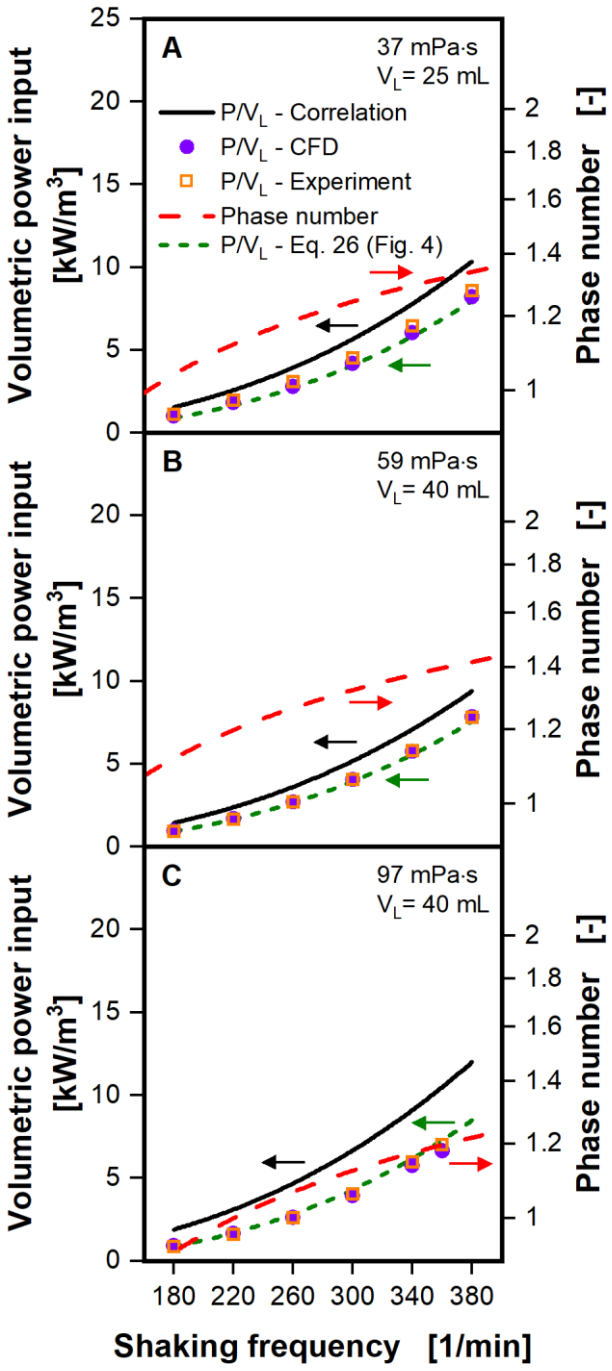

Fig. 2-10: Volumetric power input as a function of shaking frequency at elevated viscosity.

Volumetric power inputs for viscosities of 37 mPa·s at V_L = 25 mL filling volume and 59 and 97 mPa·s at V_L = 40 mL filling volume are shown in A, B and C, respectively. Values derived from the CFD model, experimentally determined values and values calculated with the power input correlation (Eq. 27), developed for in-phase operating conditions by Büchs et al.[3,4], are compared. Phase numbers are calculated according to Büchs et al.[4] (see Eq. 25) and are depicted on a logarithmic scale. Simulated conditions: Shaking diameter (d_0) = 25 mm, shaking frequency (n) = 180 – 380 rpm, surface tension (σ) = 70 mN/m, contact angle (Θ) = 20°, temperature (T) = 20°C

Fig. 2-10A shows the volumetric power inputs for 37 mPa·s at 25 mL filling volume and Fig. 2-10B and C for 59 and 97 mPa·s at 40 mL filling volume, respectively. For all three viscosities

(Fig. 2-10A, B and C) the volumetric power input from experiments and CFD differ remarkably little over the analyzed shaking frequencies. The average deviation between CFD and experiment is merely 0.14 kW/m^3 or 2.3 %. This indicates an exceptional performance of the CFD model, even at these near out-of-phase to out-of-phase operating conditions. Phase numbers for the investigated conditions are in the range of 1 to 1.5, hence already crossing the critical phase number of 1.26 by Büchs et al.[4]. Fig. 2-10 also depicts the volumetric power input calculated with the volumetric power input correlation by Büchs et al.[4] (Eq. 27). Although these values generally follow the same trajectory as the experimental data and volumetric power inputs calculated with the CFD model, they are consistently higher. In Fig. 2-10A and B the volumetric power input correlation overestimates the volumetric power input by roughly 30 %, but in Fig. 2-10C the overestimation is on average at approximately 80 %. It must be emphasized, that the volumetric power input correlation by Büchs et al.[4] was solely developed for fully in-phase operating conditions, which they based on a critical phase number of 1.26. In Fig. 2-10A the phase number crosses this critical phase number of 1.26 at a shaking frequency of 300 rpm and in Fig. 2-10B at 260 rpm. In Fig. 2-10C the phase numbers at all shaking frequencies are below this critical phase number. It is, hence, unsurprising that the overestimation by the volumetric power input correlation is larger in Fig. 2-10C, than in A and B. It should also be mentioned, that the transition from in-phase to out-of-phase is inherently a gradual transition. Hence, any one critical phase number is, although practically useful, never fully accurate. It is, therefore, unsurprising, that the volumetric power input correlation overestimates the volumetric power input at near out-of-phase conditions, even when the phase number is slightly above 1.26. This again highlights the benefit of a well validated CFD model for shake flasks.

Fig. 2-11 depicts the volumetric power input over the viscosity, complementing the plot over shaking frequency in Fig. 2-10. Varying the viscosity allows for a larger response of the phase number and, hence, enables a clearer investigation of the performance of the CFD model from in-phase into out-of-phase operating conditions. Furthermore, the limits of the volumetric power input correlation can be explored in more detail. Fig. 2-11 depicts the volumetric power input from CFD, experiment and from the power input correlation (see Eq. 27) and the phase number (see Eq. 25) at a shaking diameter of 25 mm and filling volume of 40 mL (Fig. 2-11A), 25 mm and 25 mL (Fig. 2-11B) and 50 mm and 25 mL (Fig. 2-11C), all at a shaking frequency of 300 rpm and at viscosities ranging from roughly 1 mPa·s up to 200 mPa·s. Volumetric power inputs from experiments and from the CFD model, again, align exceptionally well across almost all investigated experimental conditions. In Fig. 2-11A the deviation between experiment and

CFD is on average just 0.05 kW/m^3 (equates to 2.6 %), a remarkably small difference. Fig. 2-11B shows a similar performance for the first three viscosities of up to 37 mPa·s, with an average deviation of less than 0.3 kW/m^3 (less than 10 %). At the highest viscosity of 76.8 mPa·s in Fig. 2-11B, the largest deviation between experimental volumetric power inputs and those from CFD can be observed. The experimental value is more than 2 kW/m^3 (more than 80 %) higher, than the CFD indicates. Possible explanations will be discussed below. Volumetric power inputs from experiment and CFD differ again very little in Fig. 2-11C, by approximately 0.55 kW/m^3 (less than 9 %) for all viscosities. It is remarkable, that these small deviations between experiment and CFD hold across a wide range of phase numbers, from above 3 to below 1, notably crossing the critical phase number of 1.26 by Büchs et al.[4].

At high phase numbers, above a value of roughly 2, i.e., far above the critical phase number and, hence, at fully in-phase operating conditions, the volumetric power input correlation perfectly matches the volumetric power inputs from experiment and CFD. While the correlation continues to increase for smaller phase numbers, volumetric power inputs from CFD and experiment remain constant, or even decline slightly at high phase numbers. As discussed previously, the volumetric power input correlation was only developed for fully in-phase operating conditions and, hence, cannot accurately predict the volumetric power input at out-of-phase conditions. The volumetric power input correlation only captures the aspect of increasing friction with increasing viscosity. The deviation between the volumetric power input correlation and CFD and experiment seems to arise roughly at phase numbers of 1.5, slightly above the critical phase number of 1.26 established by Büchs et al.[4]. However, as discussed in context of Fig. 2-10, a deviation between volumetric power input correlation and experiment and CFD is to be expected, even above the critical phase number, because of the inherently gradual transition from in-phase to out-of-phase conditions. Interestingly, the largest deviation in volumetric power input between experiment and CFD of above 2 kW/m^3, shown in Fig. 2-11B, occurred at the lowest phase number in Fig. 2-11, of roughly 0.95. Notably, this phase number is below the critical phase number of 1.26 by Büchs et al.[4] and is even close to the more recent critical phase number of 0.91 by Azizan et al.[5]. At phase numbers this low, it is known, that the volumetric power input tends to become unstable and even small differences in operating conditions can strongly affect the volumetric power input[3,4,83]. Büchs et al. showed, that for large shake flasks, even the acceleration profile to reach the desired shaking frequency might determine, whether the liquid will remain in-phase or will be out-of-phase[83]. Hence, even small differences between experimental setup and CFD might lead to the rather large differences in volumetric power input observed between experiment and CFD. Across all

conditions in Fig. 2-11, the difference in volumetric power input between experiment and CFD is only 12.4 % (7.1 % when disregarding the point of largest deviation), emphasizing the high accuracy of the CFD model and experimental volumetric power inputs.

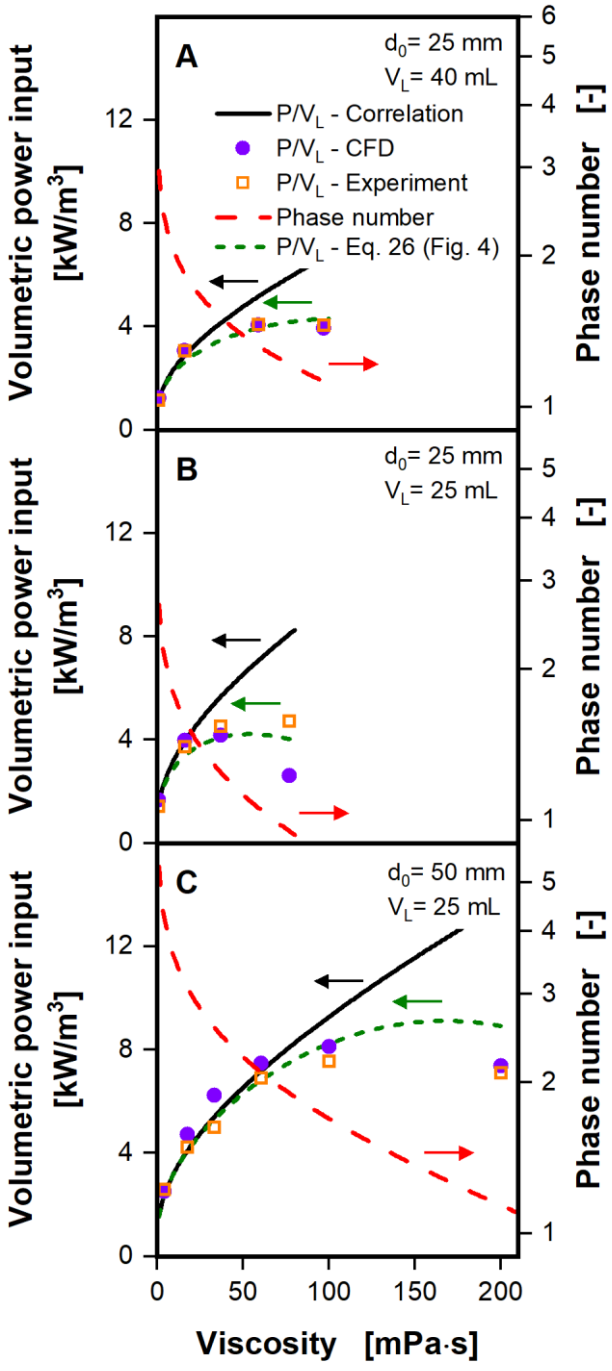

Fig. 2-11: Volumetric power input and phase number as function of viscosity.

Volumetric power inputs are derived from the CFD model and compared to experimentally determined values and values calculated with the power input correlation (Eq. 27), developed for in-phase operating conditions by Büchs et al.[3,4]. Phase numbers are calculated according to Büchs et al.[4] (see Eq. 25) and are depicted on a logarithmic scale. Simulated conditions: Shaking diameter (d_0) = 25 mm (A + B) and 50 mm (C), filling volume (V_L) = 40 mL (A) and 25 mL (B + C), shaking frequency (n) = 300 1/min, surface tension (σ) = 70 mN/m, contact angle (Θ) = 20°, temperature (T) = 20°C, viscosity (η) = 1 – 97 (A), 1 – 76.8 (B), 4 – 199 mPa·s (C)

For a more thorough estimation of the relationship of phase number and volumetric power input, the quotient of the volumetric power input from CFD and volumetric power input correlation was plotted over the phase number in Fig. 2-12. Fig. 2-12 contains more than 100 simulations. At a high phase number, the quotient between CFD and correlation is scattered with a 20 % deviation around 1. As already discussed, however, the correlation overestimates the volumetric power input, compared to the CFD, for small phase numbers. Below the critical phase number of 0.91 by Azizan et al.[5] (first vertical dashed line) this overestimation escalates. Around phase numbers of 0.5 the CFD predicts up to eight times lower volumetric power inputs. Even at the more conservative critical phase number of 1.26 by Büchs et al.[4], the volumetric power inputs by the CFD are already consistently 30 % smaller than the correlation suggests. To repeat the previous statement: Although defining a critical phase number, differentiating between in-phase and out-of-phase conditions is practical, the transition between the two is inherently gradual and cannot be truly captured in a single critical phase number. As can be seen in Fig. 2-12, the data points gradually approach unity with increasing phase number, without any drastic or abrupt changes, which would indicate a sudden onset of the out-of-phase phenomenon. Fig. 2-12 also depicts an exponential fit (green line) of the quotient of volumetric power input from CFD and volumetric power input correlation. The fit takes the following form:

$$y = -3.43 \cdot e^{-2.02 \cdot x} + 1 \qquad \text{Eq. 47}$$

where y is the quotient of volumetric power input from CFD and correlation and x the phase number. This fit enables the correction of the volumetric power input, as determined by the volumetric power input correlation at low phase numbers. In Fig. 2-10 and Fig. 2-11 the quotient was already used to correct the volumetric power input of the correlation from Büchs et al.[4], as indicated by the dashed green lines. In Fig. 2-10 the corrected volumetric power input correlation (dashed green lines) is now neatly aligned with volumetric power inputs from CFD and experiments for all three viscosities and the entire range of the shaking frequency. In Fig. 2-11 a similar performance can be observed. Only for the highest viscosities, therefore lowest phase numbers, in Fig. 2-11 B and C can a deviation between corrected volumetric power correlation (dashed green line) and values from CFD and experiment still be seen. It is, however, noteworthy, that the corrected volumetric power input correlation now displays stagnant volumetric power inputs and even declining volumetric power inputs for low phase numbers. This behavior has not been captured in the original volumetric power input correlation by Büchs et al.[4].

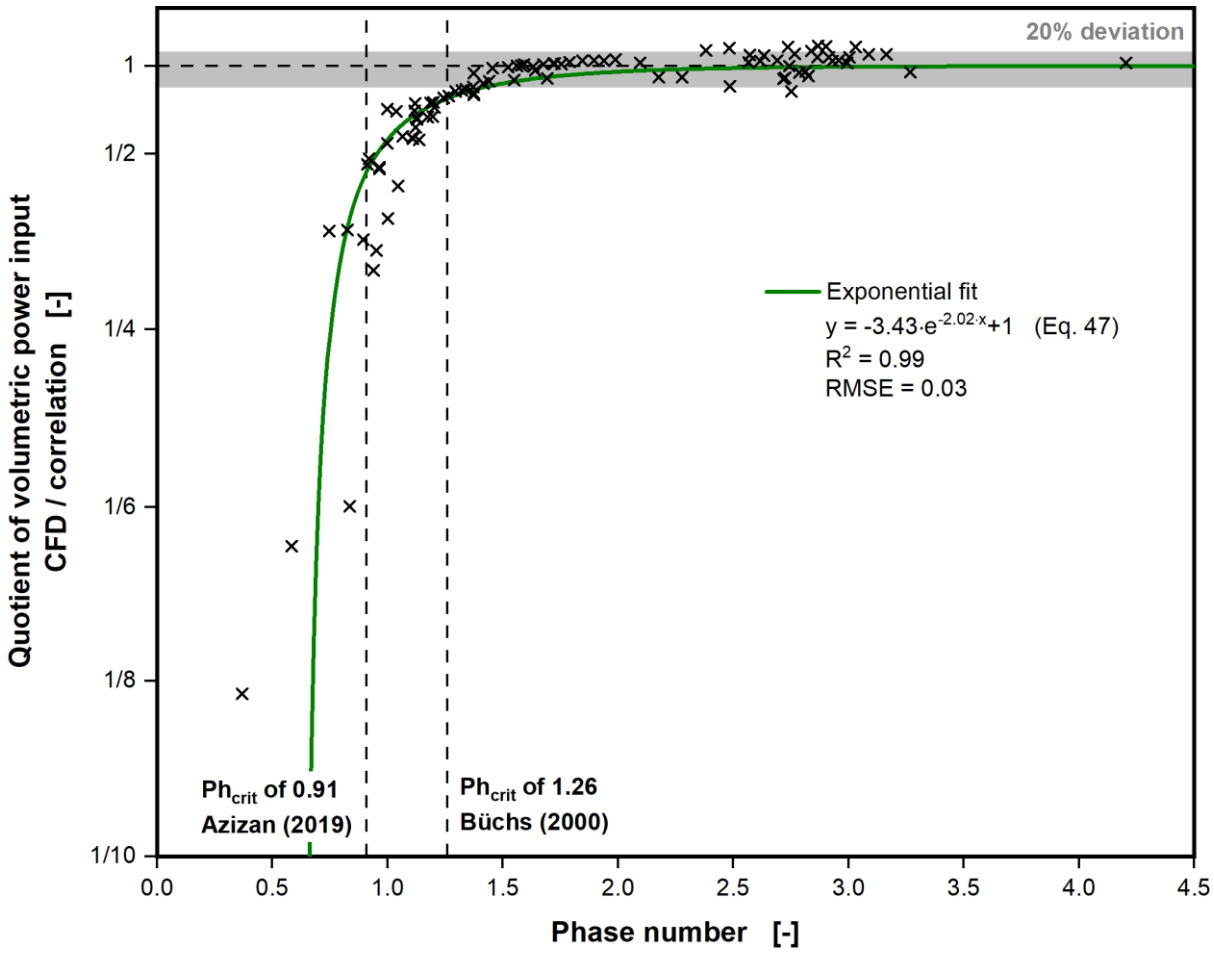

Fig. 2-12: Quotient of volumetric power inputs derived from the CFD simulations and calculated with the power input correlation (see Eq. 27), developed for in-phase operating conditions by Büchs et al.[3,4], as function of the phase number (see Eq. 46).

Dashed vertical lines show the critical phase numbers for out-of-phase conditions of 1.26, according to Büchs et al.[4] and 0.91, according to Azizan et al.[5]. The horizontal grey area indicates a 20 % deviation of the volumetric power inputs, derived from the CFD simulations from the volumetric power inputs, calculated with the power input correlation for in-phase operating conditions [4]. The green curve indicates the fitted, exponential relationship of the quotient of volumetric power input from CFD model and power input correlation with the phase number. Simulated conditions: Viscosity (η) = 0.69 – 100 mPa·s, shaking diameter (d_0) = 25 and 50 mm, shaking frequency (n) = 150 – 450 rpm, filling volume (V_L) = 15 – 40 mL, surface tension (σ) = 70 mN/m, contact angle (Θ) = 20°, temperature (T) = 20 – 37 °C

Despite the general recommendation to perform shake flask experiments under in-phase operating conditions, this might not always be possible, particularly at high viscosity. Furthermore, it might sometimes even be advantageous to deliberately perform experiments close to out-of-phase operating conditions, or perhaps even slightly out-of-phase, to exploit the phenomenon as a selection pressure. Peter et al. investigated the influence of the out-of-phase phenomenon on two previously performed screening projects of filamentous fungi[20]. They found that initial wild type strains reached out-of-phase operating conditions during the fermentation, due to the filamentous growth and, hence, increasing viscosity. It turned out, that

later strain generations, selected during the screening campaign, showed a successively lower maximal viscosity, remaining in-phase during cultivation. A less filamentous morphology caused the lower maximal viscosity of later strain generations. Peter et al. underline that later strain generations were chosen, during the screening projects, based on the production titer, but that the increases in titer were simply caused by the altered morphology[20]. The altered morphology led to in-phase operating conditions, which improved mixing and mass transfer. Although the selection of strains with more disperse growth was unintentional in the screening projects discussed by Peter et al.[20], deliberately exploiting the out-of-phase phenomenon as a selection pressure for manipulation of fungal morphology seems promising. The presented CFD model and to some extent the correction of the volumetric power input (exponential fit, i.e., green line, in Fig. 2-12) enable the determination of volumetric power input at the required operating conditions necessary for such a carefully planned screening campaign.

The deviations between volumetric power input correlation and volumetric power input from experiments and CFD, observed with decreasing phase number in Fig. 2-10 and Fig. 2-11, must be connected to distinct changes in the liquid distribution. Changes in the liquid distribution are the only possible reason why the volumetric power input would not continue to rise with increasing viscosity (see Fig. 2-11), as is predicted by the volumetric power input correlation. While Büchs et al. used the volumetric power input to determine their critical phase number for out-of-phase conditions[4], Azizan et al. already used their observations of the liquid distribution to determine a critical phase number[5]. Fig. 2-13 depicts 3D representations of the liquid distribution of a selection of CFD simulations. The color scale from blue to red corresponds to the magnitude of the velocity vector in the simulation. While Fig. 2-13A shows the results at 15 mL filling volume with 250 rpm shaking frequency, Fig. 2-13B shows the same filling volume at 450 rpm. For both shaking frequencies the same three viscosities were deliberately chosen to cross both critical phase numbers of 0.91 and 1.26. For the lowest viscosity of 0.69 mPa·s, corresponding to phase numbers larger than 2, the bulk liquid flows along the flask wall, with the leading edge showing a smooth, rounded shape. In contrast, at the highest viscosity of 104 mPa·s, i.e., phase numbers below the critical phase number of 0.91 by Azizan et al.[5], the liquid no longer flows along the flask wall and remains instead at the bottom of the shake flask. Only a tiny wave, flowing along the bottom with greatly reduced maximal speeds can be seen in these cases. An indication of this shift in liquid distribution was already visible in Fig. 2-8. In Fig. 2-8G – I, the phase numbers dropped below the critical phase number of 0.91. Compared to Fig. 2-8A – F the maximal liquid height is greatly reduced, implying that the liquid no longer flows along the flask wall. Additionally, the shape of the observed rotating

bulk liquid changed between Fig. 2-8A – F and G – I, aligning with the findings from Fig. 2-13. The intermediate viscosity of 16.7 mPa·s in Fig. 2-13 results in phase number of 1.21 and 1.44, i.e., close to the critical phase number by Büchs et al.[4]. At these phase numbers, the liquid still flows largely along the flask wall, but the rotating bulk liquid appears more compacted, with the leading edge having a much narrower tip. Incidentally, this compacting of the rotating bulk liquid becomes more severe with decreasing phase numbers. The described change in liquid shape can be observed across both shaking frequencies for the cases above the critical phase number of 0.91 (B at 0.69 mPa·s → A at 0.69 mPa·s → B at 16.7 mPa·s → A at 16.7 mPa·s).

The findings for the volumetric power input and investigation of the liquid distribution confirm the critical phase number of 0.91 by Azizan et al.[5]. Below this phase number a complete collapse of the liquid distribution, with drastic decreases in the volumetric power input, can be observed. But they also give validity to the original critical phase number of 1.26 by Büchs et al.[4]. Around this phase number first changes in the liquid distribution are visible, with noticeable effects on the volumetric power input. Although, the characterization in in-phase and out-of-phase operating conditions remains useful in practice the transition between these states is gradual in nature, as underlined by the presented results.

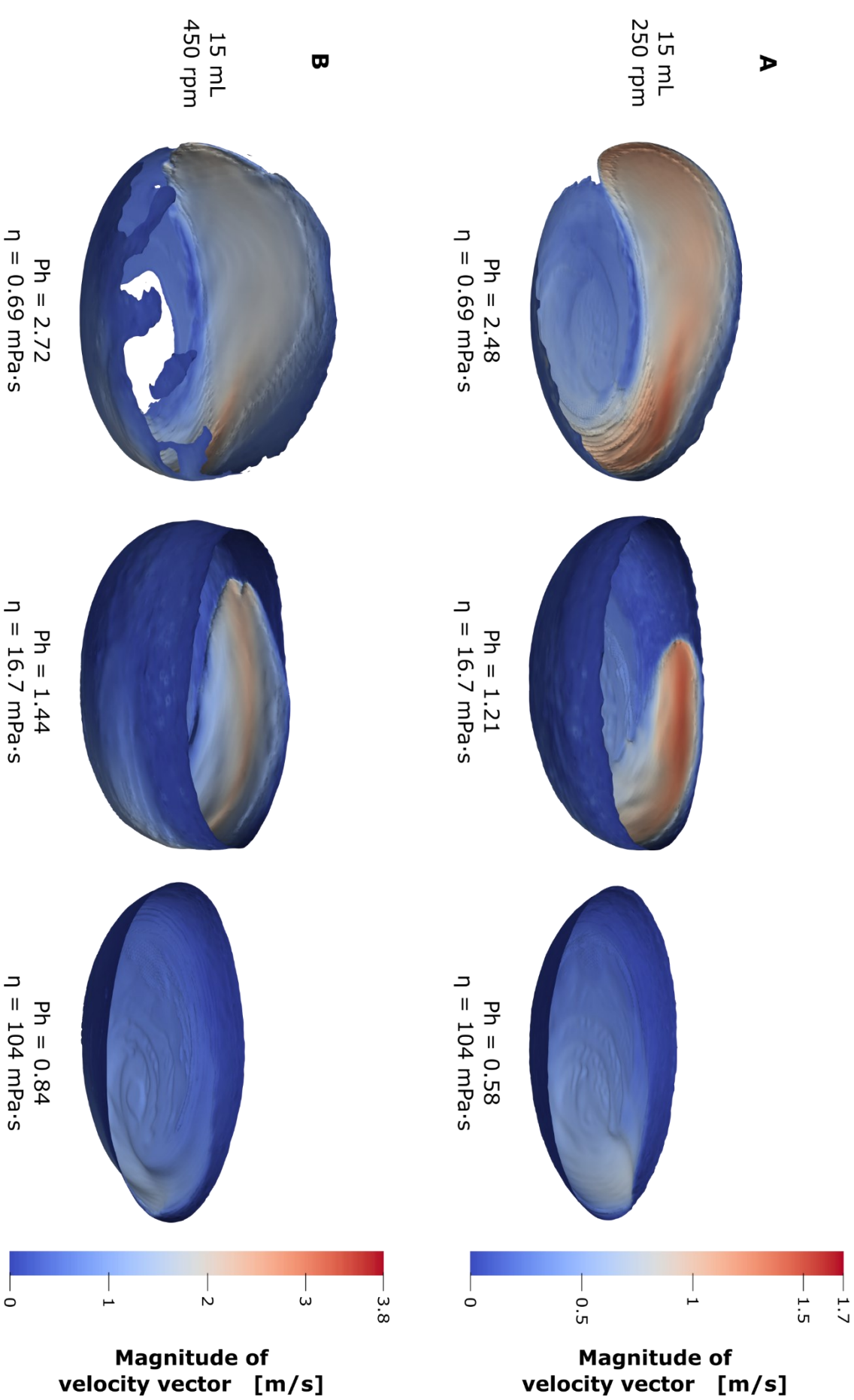
A
15 mL
250 rpm
Ph = 2.48
η = 0.69 mPa·s
Ph = 1.21
η = 16.7 mPa·s
Ph = 0.58
η = 104 mPa·s
B
15 mL
450 rpm
Ph = 2.72
η = 0.69 mPa·s
Ph = 1.44
η = 16.7 mPa·s
Ph = 0.84
η = 104 mPa·s
0
0.5
1
1.5
1.7
Magnitude of
velocity vector [m/s]
0
1
2
3
3.8
Magnitude of
velocity vector [m/s]

Fig. 2-13: 3D images of the free surface area from CFD simulations with decreasing phase numbers (see Eq. 46), passing the critical phase numbers.

The color scale from blue to red illustrates the magnitude of the velocity vector, easily highlighting the rotating bulk liquid in the simulations. Conditions were deliberately chosen to cross the critical phase numbers from Büchs et al. of 1.26[4] and Azizan et al of 0.91[5] with increasing viscosity. Simulated conditions: Viscosity (η) = 0.69, 16.7 and 104 mPa·s, shaking diameter (d_0) = 25 mm, filling volume (V_L) = 15 mL, surface tension (σ) = 70 mN/m, contact angle (Θ) = 20°, temperature (T) = 20 °C, shaking frequency (n) = 250 rpm (A) and 450 rpm (B)

2.3.3 Volumetric gas-liquid mass transfer rates

The k_La value is also one of the most important process parameters for shake flasks and bioprocesses in general. Hence, the k_La value was computed for the CFD simulations, investigating again the influence of increasing viscosity. Fig. 2-14 depicts the specific interfacial area (a), the gas-liquid mass transfer coefficient (k_L) and the k_La value at a filling volume of 40 mL (Fig. 2-14A, C, E) and 25 mL (Fig. 2-14B, D, F) at 300 rpm and viscosities from 1 mPa·s up to 97 mPa·s. A wide variety of other shaking conditions are included in the supplement in Appendix 14 to Appendix 17.

The specific interfacial area (a) stays almost constant with increasing viscosity, only showing a small decline at the highest viscosity at 25 mL (see Fig. 2-14B). This finding is consistent with the analysis by Henzler and Schedel[28], who also found that the specific interfacial area (a) is not significantly affected by the viscosity. As expected, the reduction of filling volume, at otherwise constant shaking conditions, leads to a higher specific interfacial area (a) (compare Fig. 2-14A and B). Further, the specific interfacial area (a) is roughly 25 m^2/m^3 lower at the waterlike viscosity of 1 mPa·s, compared to the next higher viscosity at both filling volumes. This underestimation at waterlike viscosity is most likely a shortcoming of the presented CFD model. The mesh size of the CFD model is probably too coarse to fully resolve the liquid film of roughly 50 µm, expected at waterlike viscosity. The trade-off of computational effort and model accuracy was mentioned above. The effect can be seen in Fig. 2-13, where the liquid film is fully resolved for the higher viscosities, but not for the waterlike viscosity. For the two higher viscosities in Fig. 2-13 the liquid film (dark blue area) reaches up to the maximal liquid height over the entire circumference of the shake flasks, while this is not the case for the waterlike viscosity.

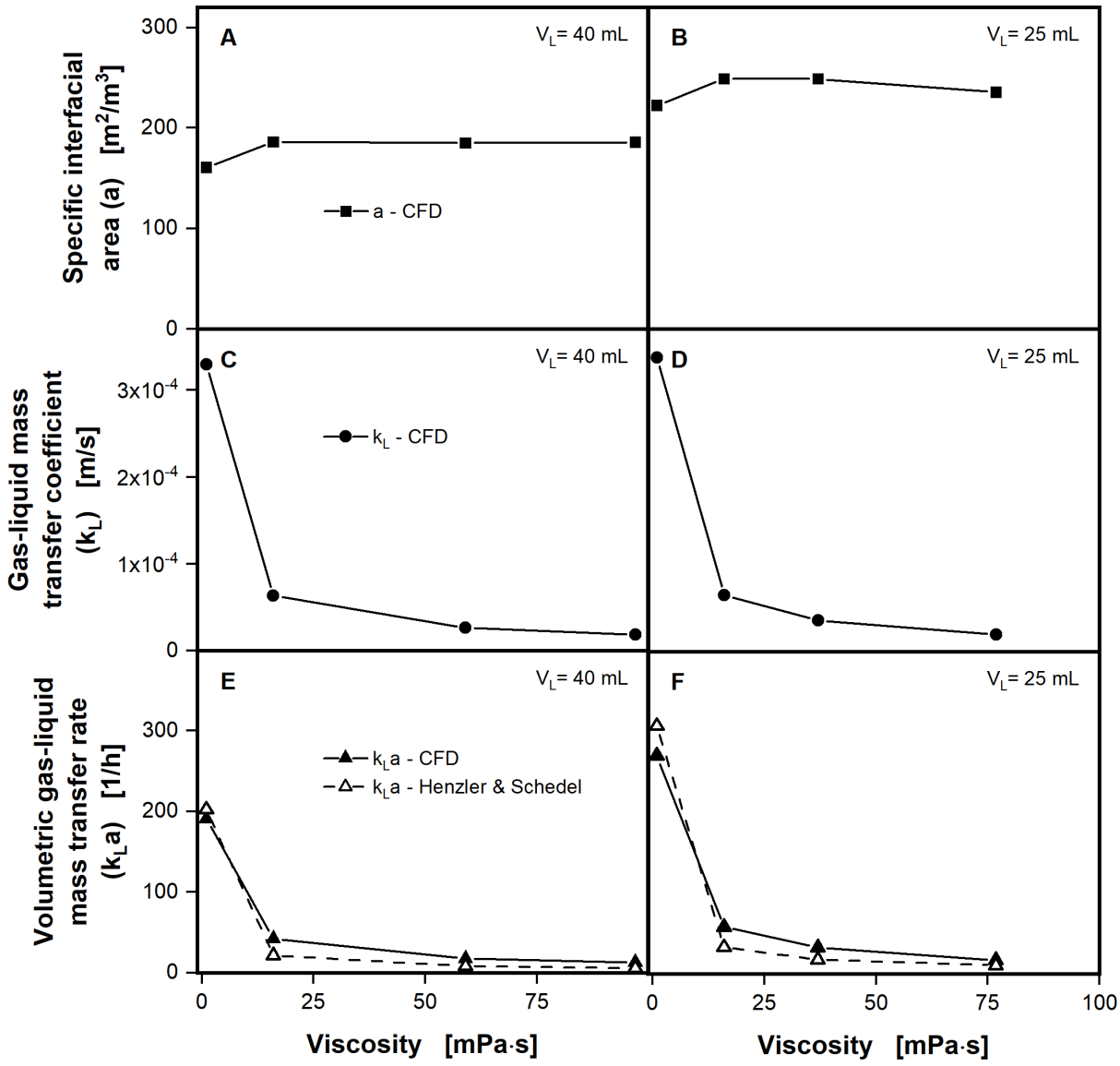

Fig. 2-14: The k_La value derived from CFD simulations as function of viscosity.

The specific interfacial area (A + B), gas-liquid mass transfer coefficient k_L (C + D) and volumetric gas-liquid mass transfer rate k_La (E + F) are derived from the CFD simulations and depicted as a function of viscosity. The k_La values from the CFD simulations in E and F are compared to values calculated with the k_La correlation from Henzler and Schedel[28] (see Eq. 37). Simulated conditions: Shaking frequency (n) = 300 rpm, shaking diameter (d_0) = 25 mm, surface tension (σ) = 70 mN/m, contact angle (Θ) = 20°, temperature (T) = 20 °C, viscosity (η) = 1 – 97 mPa·s (A, C, E) and 1 – 76.8 mPa·s (B, D, F), filling volume V_L = 40 mL (A, C, E) and 25 mL (B, D, F)

The k_L decreases sharply with increasing viscosity at both filling volumes (Fig. 2-14C and D), dropping from almost $3x10^{-4}$ m/s to about $0.5x10^{-4}$ m/s at 16 mPa·s and decreasing further to below $0.2x10^{-4}$ m/s at the highest respective viscosity. This decline of the k_L is directly caused by the reduction of the diffusion coefficient and changes in liquid distribution due to the increasing viscosity. The k_La value, being the product of k_L and interfacial area, shows the combination of both signals, again sharply decreasing with moderately increasing viscosity.

Values computed with the CFD model (see Eq. 36) are compared to k_La values calculated with the k_La correlation from Henzler and Schedel (see Eq. 37). The progression of the k_La value from CFD and k_La correlation are exceptionally similar. At waterlike viscosity the k_La value from the CFD is just 5 % (Fig. 2-14E) and 12 % (Fig. 2-14F) lower, than indicated by the k_La correlation from Henzler and Schedel[28]. For the higher viscosities, the k_La from the CFD model is approximately twice as high as indicated by the k_La correlation from Henzler and Schedel[28]. It should be noted, that, both, the CFD method and k_La correlation from Henzler and Schedel[28] require the diffusion coefficient for the k_La value calculation (see Eq. 34 and Eq. 37). In this work the diffusion coefficient is calculated according to Eq. 33,which gives the diffusion for pure oxygen in pure water, including viscous effects. It, however, does not include effects of other cultivation media components, like salt, on the diffusion coefficient. Fortunately, CFD method and k_La correlation from Henzler and Schedel[28] include the diffusion coefficient with the same weighting. Therefore, it does not affect the comparison of the two.

Fig. 2-15 shows a parity plot of both CFD and k_La correlation for a more detailed comparison, containing more than 100 simulations. Data points are presented separately for waterlike conditions of around 1 mPa·s (open blue squares) and for the more viscous conditions above 1 mPa·s (open red circles). The k_La values in Fig. 2-15 span three orders of magnitude, from approximately 5 h^{-1} to 750 h^{-1}. Across this entire range the data points follow the parity line quite closely. Data points for the waterlike viscosity are especially close to the parity line. On average the k_La values from the CFD model are less than 20 % smaller than suggested by the k_La correlation. For the higher viscosity, the difference between CFD model and k_La correlation is somewhat larger, but with data points remaining highly parallel to the parity line. On average the k_La values form the CFD model are twice as high, as indicated by the k_La correlation (+93 % with a standard deviation of 32 %). As discussed previously, the liquid film is not fully resolved in the CFD model for waterlike viscosity. The liquid film has, however, previously been proven to contribute significantly to the overall oxygen transfer in shake flasks experiments[1,2,23,81,84]. Maier et al. showed, that the maximal oxygen transfer capacity in hydrophobic shake flasks, where no liquid film is formed, was reduced by up to a factor of four[1]. Hence, the not fully resolved liquid film in the CFD model might explain, why the CFD model produces k_La values lower than the k_La correlation at low viscosity, but higher than the k_La correlation at higher viscosities. Liu et al. showed a similar deviation between k_La values computed by their CFD model for shake flasks and the k_La correlation by Henzler and Schedel[28] for waterlike viscosity, albeit for only four CFD simulations, performed at similar shaking conditions[39]. Interestingly, their CFD model apparently also did not fully resolve the liquid film.

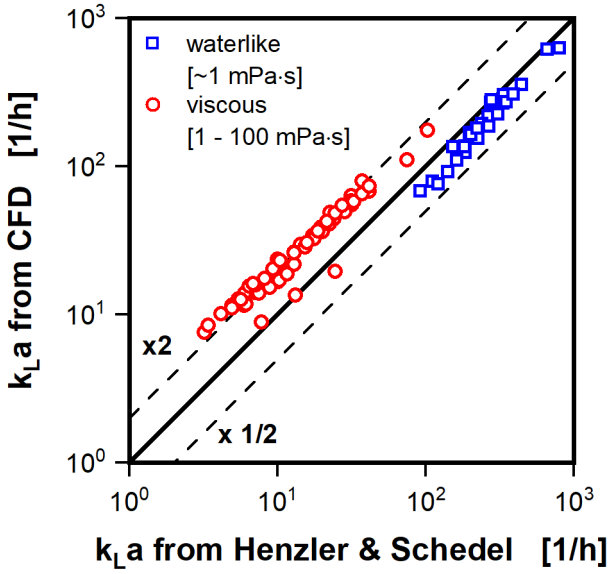

Fig. 2-15: Parity plot of k_La values derived from the CFD simulations against values calculated with the k_La correlation from Henzler and Schedel[28] (see Eq. 37).

Simulated conditions are split into two groups; waterlike viscosity of roughly 1 mPa·s (blue open squares) and elevated viscosity of 1 – 100 mPa·s (red open circles). Black lines indicate parity and an over- and underestimation by a factor of 2. Simulated conditions: Viscosity (η) = 0.69 - 100 mPa·s, shaking diameter (d_0) = 25 and 50 mm, shaking frequency (n) = 150 - 450 rpm, filling volume (V_L) = 15 – 40 mL, surface tension (σ) = 70 mN/m, contact angle (Θ) = 20°, temperature (T) = 20 – 37°C

The k_La computation in the CFD model uses the mass transfer model from Lamont & Scott (1970) (see Eq. 34), which focuses on the influence of small eddies near the interface surface, as the acting force behind the mass transfer. Lamont and Scott compared the results of their mathematical approach for the calculation of the k_L to three widely different experimental situations[77]. Firstly, they compared it to their own experimental work for bubbles in a turbulent pipe flow. Secondly, to the experimental data from Calder bank and Moo-Young for bubble aerated stirred tank reactors including a solid phase[85] and thirdly experimental data from Fortescue and Pearson for the transfer into the surface of turbulent channel flow[86]. Lamont and Scott also found a deviation within a factor of 2 between their model and the three experimental data sets[77].

For the correlation of the k_La value for shake flasks, Henzler and Schedel determined oxygen transfer rates for experiments with the sulfite system and culture broth of *Escherichia coli* and *Streptomyces tendae*[28]. They used the resulting oxygen transfer rates to calculate the k_La value under the assumption of a complete absence of oxygen in the liquid phase (dissolved oxygen tension = 0)[28]. However, Meier et al. later showed, that the dissolved oxygen tension does not reach zero in the liquid film[84]. Hence, the correlation by Henzler and Schedel likely

underestimates the k_La value for shake flasks to some degree. Furthermore, Henzler and Schedel provide, to our knowledge, the only k_La correlation, for which the influence of the viscosity was fitted based on experimental results. However, there are some unfortunate limitations to the data used for elevated viscosity. Even though, Henzler and Schedel measure the shear-thinning behavior of the utilized *Streptomyces tendae* culture broth, they were forced to assume a fixed shear rate (100 s^{-1}) to estimate a viscosity for their model[28]. The later developed correlation for effective shear rates would have allowed for a more precise estimation of the shear rate and, hence, viscosity[7]. Additionally, Henzler and Schedel varied the viscosity by performing experiments with the sulfite system using water at various temperatures and glucose solutions of different concentrations[28]. While this approach does not suffer the same problems of shear-thinning behavior as the *Streptomyces tendae* culture broth, it unfortunately only covers viscosities from roughly 0.6 to 5 mPa·s. Hence, the k_La correlation by Henzler and Schedel[28] might be more accurate at waterlike and low viscosities, than at higher viscosities. Given the discussed accuracy of the transfer model from Lamont and Scott[77] and shortcoming of the k_La correlation by Henzler and Schedel[28], the performance of the CFD model, predicting the k_La value across three orders of magnitude is satisfactory.

2.3.4 Shear rates

In this work, viscosity has proven to have a major influence on liquid distribution, volumetric power input and k_La value. However, as stated previously, the usually encountered shear-thinning behavior of most biopolymers and filamentous fungi was approximated with a constant viscosity for Newtonian flow, based on the correlation for effective shear rates by Giese et al.[7]. Ideally, the CFD model would directly incorporate the non-Newtonian behavior by calculating shear rates in each mesh cell. OpenFOAM, in fact, provides a scheme to calculate the shear rate (see Eq. 40). A set of CFD simulations, modelling the shear-thinning behavior with the power law, has been performed for this work. Simulations were performed with the same conditions as shown in Fig. 2-8 (except for the viscosity). Resulting liquid contact lines are shown in the supplement (see Appendix 18) and can be compared to Fig. 2-8. Due to the very weak shear-thinning behavior of the polyvinylpyrrolidone (flow behavior index of 0.956) used by Azizan et al.[5,6], the effect on the computed liquid contact lines, of directly modelling the non-Newtonian behavior is almost non-existent. For a better insight into the performance of the OpenFOAM scheme for the shear rate calculation, resulting shear rates of all performed simulations are compared to the effective shear rates calculated with the correlation from Giese et al.[7] in the parity plot in Fig. 2-16A.

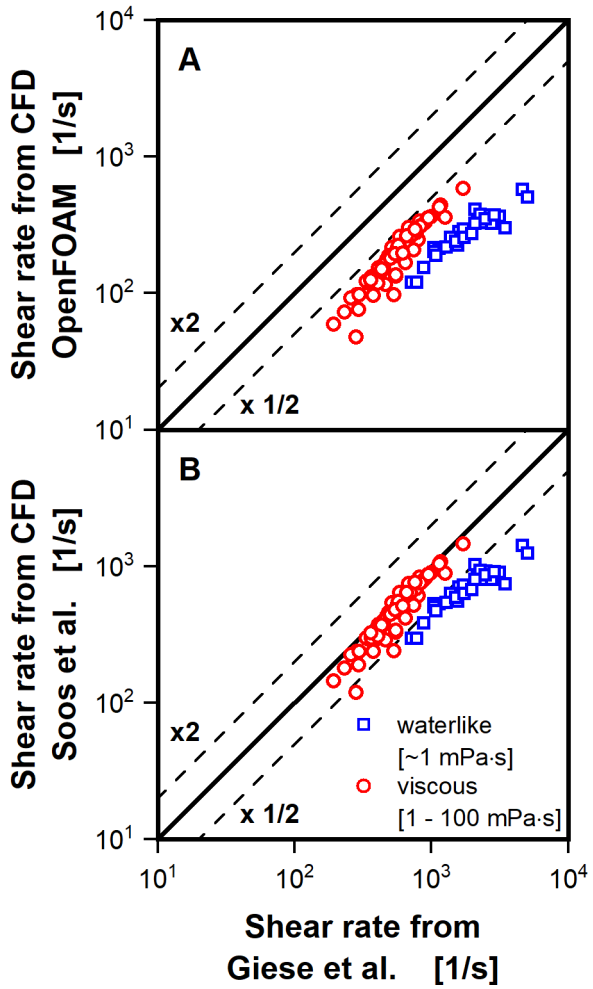

Fig. 2-16: Parity plots of two approaches to derive shear rates from the CFD simulations against values calculated with the correlation from Giese et al.[7] (see Eq. 46).

Simulated conditions are split into two groups; waterlike viscosity of roughly 1 mPa·s (blue open squares) and elevated viscosity of 1 – 100 mPa·s (red open circles). Black lines indicate parity and an over- and underestimation by a factor of 2. In A the shear rate calculation is the one implemented in OpenFOAM. In B the shear rate calculation for the CFD model is based on the calculation of shear stress provided by Soos et al.[80]. Simulated conditions: Viscosity (η) = 0.69 - 100 mPa·s, shaking diameter (d_0) = 25 and 50 mm, shaking frequency (n) = 150 - 450 rpm, filling volume (V_L) = 15 – 40 mL, surface tension (σ) = 70 mN/m, contact angle (Θ) = 20°, temperature (T) = 20 – 37°C

All data points are again split into waterlike and higher viscosity. It should be noted that the determination of a shear rate, in context of shear-thinning behavior, is only truly relevant for elevated viscosities above waterlike viscosity. At waterlike viscosity (blue open squares) the shear rates calculated with the OpenFOAM scheme are on average roughly six times smaller than suggested by the correlation for effective shear rates. At the higher viscosity the performance is much better, showing only three times smaller values. As the overall performance of the OpenFOAM scheme, compared to the correlation for effective shear rates was not satisfactory, an additional approach for computing the shear rates was investigated. This approach is based on the computation of average shear stress, as given by Soos et al.[80](see

Eq. 41). According to Soos et al. this calculation of average shear stress is valid only for laminar flow conditions[80]. Although, transitional flow is to be expected for waterlike viscosity, liquid flow is laminar at higher viscosities in shake flasks. Importantly, the estimation of shear rates is mostly of interest for higher viscosities, where shear-thinning behavior might need to be modelled. Under the assumption of Newtonian flow, the computed shear stress can be easily transformed to the shear rate. A resulting parity plot, comparing the results to the correlation for effective shear rates by Giese et al.[7] is shown in Fig. 2-16B. Generally, the data points are much closer to the parity line than for the OpenFOAM scheme. For waterlike viscosity, the correlation for effective shear rates now only predicts values to be 2.6 times smaller than the CFD model indicates. For the higher viscosity this difference is reduced to just 16 %. For both methodologies for the calculation of the shear rate in the CFD model, the larger underestimation for the waterlike viscosity is surprising. The only apparent difference to the simulations at the higher viscosity is the not fully resolved liquid film. However, as fully resolving the liquid film was not necessary to correctly predict the volumetric power input, the importance of the film was not expected. Again, estimation of the shear rate, with the aim of simulating shear-thinning behavior, is more relevant for elevated viscosities. Although the second presented approach appears to model the shear rate much more accurately, especially for elevated viscosities, further research into its validity is necessary. Notably, the conversion of shear stress to shear rate is no longer straight forward, when non-Newtonian conditions are simulated in the CFD. An iterative approach of estimating the shear rate with an approximation of the viscosity in the mesh cell, calculation of the shear rate and following adjustment of the viscosity in the mesh cell would be necessary.

2.4 Conclusion

The presented CFD model for shake flasks excellently predicts liquid distributions across a wide range of operating conditions. This includes simulations with a negligible viscosity, where resulting liquid contact lines were compared to the mechanistic model by Büchs et al.[74] and simulations with waterlike viscosity up to 100 mPa·s, where results were compared to the experimental data by Azizan et al. [5,6]. Notably, simulations at high viscosity reach and surpass out-of-phase operating conditions. At elevated viscosity a liquid film was observed in the CFD simulations. The liquid film had an approximate thickness of 500 µm at 16.7 mPa·s and of 1000 µm at 80 mPa·s. Previous experimental measurements of the liquid film thickness in shake flasks by Hermann show similar values for the liquid film[82]. Hermann found a film thickness of roughly 800 µm at 35 mPa·s and of roughly 1000 µm at 99 mPa·s[82] (see Appendix 9). The estimation of the liquid distribution by the presented CFD model has already been used to aid in the design of a specific shaken bioreactors with concentric rings (termed “perforated ring flask”) by Hansen et al.[50].

Furthermore, the volumetric power input was calculated with the CFD model, deviating by less than 7 % from experimentally determined values form Büchs et al.[3,4] across all tested conditions, including near out-of-phase operating conditions. The volumetric power input correlation by Büchs et al.[4] proofed highly accurate for fully in-phase operating conditions, deviating by less than 0.01 kW/m^3 from CFD and experimental results. With decreasing phase number, however, the volumetric power input becomes increasingly inaccurate as it does not model the out-of-phase phenomenon. In this work a correction for the volumetric power input correlation, as function of the phase number is provided, allowing an approximation of the volumetric power input at complete out-of-phase operating conditions (down to phase numbers of 0.5). With an accurate estimation of the volumetric power input near the out-of-phase phenomenon, utilizing the out-of-phase phenomenon as a selection pressure might become possible[20].

Generally, the CFD model confirmed the critical phase number of 0.91 by Azizan et al.[5], below which a complete collapse of the liquid distribution could be observed. But the model results also confirm the more conservative critical phase number of 1.26, originally published by Büchs et al.[4]. Below this number initial effects on liquid distribution and volumetric power input could already be observed. Importantly, the CFD model results emphasized the inherently gradual nature of the transition from in-phase to out-of-phase operating conditions.

It was also shown, that the CFD model could be used to predict the k_La, one of the most important process parameters, sufficiently well. On average, the CFD model results deviated by less than a factor of two from the established correlation by Henzler and Schedel[28]. Tested conditions span three orders of magnitude of the k_La, including in-phase and out-of-phase operating conditions. Lastly, a first investigation into the estimation of shear rates, based on the CFD model, was performed. A computation, based on the calculation of the shear stress according to Soos et al.[80], proved more accurate, than the standard scheme provided in OpenFOAM. Further research into the applicability of the method for the simulation of non-Newtonian fluids is still required.

Contribution statement for chapter 3:

The experiments, results and findings are published as “Combined optical measurement of dissolved oxygen tension (DOT), pH value, biomass and viscosity in shake flasks” in the Biochemical Engineering Journal. Only small modifications have been made for this thesis. The original work was prepared in a joint effort with David Vonester and published under a shared first authorship. Separating the work into individual contributions is virtually impossible. Both first authors contributed equally to experiments, analysis, visualization, drafting, writing and revisions of the manuscript. The experimental work was supported by Marc Tüschenbönner during his master thesis (Fig. 3-4, Fig. 3-8 and experiments in the appendix) and Maximilian Hoffmann in his position as student assistant (Fig. 3-5, Fig. 3-6 and Fig. 3-7). Maximilian Hoffmann was supervised by David Vonester and Marc Tüschenbönner by myself. The valuable work of Maximilian and Marc is greatly appreciated.

Chapter 3

3 Novel Online Monitoring Technique for Shake Flasks

3.1 Background

Shake flasks are widely used in the early stages of bioprocess development e.g., in strain selection or media optimization. Online monitoring of cultivations during these steps is highly advantageous[87,88]. The respiratory activity monitoring system (RAMOS) (HiTec Zang GmbH, Herzogenrath, Germany) and the transfer-rate online measurement device (TOM) (Adolf Kühner AG, Birsfelden, Switzerland) both target the gaseous headspace and enable the recording of the oxygen transfer rate (OTR) and carbon dioxide transfer rate (CTR) by measuring partial pressures in the headspace[89–91]. Other approaches enable online measurements of the pH value, dissolved oxygen tension (DOT), viscosity and biomass by monitoring the liquid phase: Monitoring of the pH value is achieved with fluorescent pH-sensitive spots[92]. Spots are glued to the inside of the shake flasks and optically read out from the outside of the shake flask. The DOT can be measured in a similar fashion with fluorescent, oxygen-sensitive spots[93–96]. Combined measurements of the DOT and pH value in shake flasks were performed by Schneider et al.[97]. They used the commercially available Shake Flask Reader (SFR) (PreSens Precision Sensing GmbH, Regensburg, Germany)[97]. Hansen et al.[98] and Flitsch et al.[99] found that DOT spots, which are glued at a fixed position in the shake flask, are not suitable. Due to the rotation of the shake flasks, and, hence, the resulting rotation of the liquid phase, a fixed spot is not in constant contact with the bulk liquid during a revolution of the shake flask. This leads to a mixed signal and an overestimation of DOT values by 5 – 28 %

air saturation[98,99]. Notably, the necessity of a constant contact with the bulk liquid is apparently unique to the DOT spots and has not been described for pH spots. As an alternative to DOT spots, fluorescent oxygen-sensitive nanoparticles can be used and were introduced by Borisov & Klimant[100]. Flitsch et al.[99] and Ladner et al.[66] used commercially available oxygen-sensitive Oxnano nanoparticles (PyroScience GmbH, Aachen, Germany) in shake flask cultivations. Nanoparticles can be added directly to the cultivation medium, ensuring a constant contact between the oxygen-sensitive component and the bulk liquid. The optical sensor is still in a fixed position on the outside of the shake flask. Hence, the optical sensor alternates between measuring the DOT in the rotating bulk liquid and liquid film[66,99]. Tracking of the position of the bulk liquid allowed Ladner et al. to only trigger DOT measurements of the Oxnano nanoparticles, when the bulk liquid was in front of the sensor[66].

The rotation of the bulk liquid can also be exploited to measure the viscosity in shake flask experiments[64,66,67]. The position of the bulk liquid, relative to direction of the centrifugal force, depends on the liquid's viscosity. The effects of the viscosity on the rotating liquid in shake flasks has been explored in detail in chapter 2. With an increase in viscosity, the bulk liquid is shifted against the shaking direction relative to the centrifugal force. This shift was first used to determine the viscosity by Sieben et al.[64]. Ladner et al.[66] used the same principle to determine the viscosity in shake flask experiments by utilizing the signal intensity of Oxnano nanoparticles.

Recently, non-invasive online monitoring of the biomass via scattered light, specifically backscatter, were performed in various shake flask experiments using adapted versions of the commercially available SFR or SFR vario systems[101–106]. Similar to DOT measurements with nanoparticles, the scattered light measurement in shake flasks is heavily affected by the position of the rotating bulk liquid. Schmidt-Hager et al.[106] presented a modified version of the SFR, extended by a scattered light sensor. This device is capable of triggering the angular measurement time point of the scattered light measurement in the rotating bulk liquid. However, this is only possible for water-like, non-changing viscosities. Ude et al.[103] further applied the device to cultivations of bacteria, fungi, yeasts and mammalian cells. Mao et al.[107] presented a device, also capable of triggering the scattered light measurement at water-like viscosities.

As discussed, various online monitoring systems for the DOT, pH and scattered light in shake flasks are already commercially available. The Cell Growth Quantifier (CGQ) from sbi Scientific Bioprocessing enables the monitoring of biomass by scattered light measurements[108]. PreSens Precision Sensing GmbH offers the SFR and SFR vario, which enable monitoring of

DOT and pH and monitoring of DOT, biomass, pH or CO_2, respectively[109,110]. PyroScience GmbH currently offers pH and DOT spots and Oxnano nanoparticles for DOT measurements, which can be applied to shake flasks[111].

In this work, the already available pH spots and Oxnano nanoparticles from PyroScience were combined with a newly developed scattered light sensor and viscosity monitoring in a single system for shake flasks. This new system is termed ShakeVisc. It stands out from existing devices in several aspects. The CGQ by default conducts untriggered scattered light measurements at 521 nm[112]. In contrast, scattered light measurements of the ShakeVisc system are triggered to the optimal angular position of the rotating bulk liquid and operate at 620 nm. At this wavelength the impact of color changes of the medium is minimized[113]. The SFR and SFR vario utilize spots for monitoring of the DOT. To avoid the overestimation of DOT measurements that is inevitably caused by DOT spots[98,99], the ShakeVisc system utilizes Oxnano nanoparticles suspended in the culture broth. The SFR vario is capable of triggering scattered light measurements, but only at water-like, non-changing viscosities. The ShakeVisc system presented in this work is capable of triggering scattered light measurements also at changing and elevated viscosities. Additionally, there is no commercially available system for online measurement of the viscosity in shake flasks. Monitoring the viscosity is of great interest, when working with filamentous microorganisms and liquid systems with viscous substrates or products[67,114–118]. The ShakeVisc system can be combined with a RAMOS or TOM and provides an unprecedented number of online signals (DOT, pH, scattered light, viscosity, OTR, CTR and respiratory quotient) for shake flasks.

3.2 Materials and Methods

3.2.1 Microorganisms and media

All pre-cultures and main-cultures were carried out in 250 mL RAMOS shake flasks and standard shake flasks at a shaking diameter of 50 mm in a climo-shaker ISFX-1 (Adolf Kühner AG, Biersfelden, Switzerland). Media were inoculated at the start of experiments to the optical densities detailed below.

Pre-cultures and main-cultures of Escherichia coli pET11b AmpR were carried out in Wilms-MOPS medium. The Wilms-MOPS medium contains 6.98 g/L $(NH_4)_2SO_4$, 3 g/L K_2HPO_4, 2 g/L Na_2SO_4 and 41.85 g/L (N-morpholino)-propane sulfonic acid (MOPS). The pH was adjusted to 7.5 with NaOH. The medium was subsequently heat-sterilized and cooled down. Prior to the start of the experiment, the following solutions were added to the Wilms-MOPS medium: 10 mL/L of a heat sterilized 50 g/L $MgSO_4 \cdot 7H_2O$ stock solution, 40 mL/L of a heat sterilized 500 g/L glucose stock solution, 1 mL/L of a sterile filtrated 100 g/L ampicillin sodium salt stock solution, 1 mL/L of a sterile filtrated 10 g/L thiamine hydrochloride stock solution and 1 mL/L of sterile filtrated trace elements solution. The trace elements solution contains 0.54 g/L $ZnSO_4 \cdot 7H_2O$, 0.48 g/L $CuSO_4 \cdot 5H_2O$, 0.3 g/L $MnSO_4 \cdot H_2O$, 0.54 g/L $CoCl_2 \cdot 6H_2O$, 41.76 g/L $FeCl_3 \cdot 6H_2O$, 1.98 g/L $CaCl_2 \cdot 2H_2O$ and 33.4 g/L $Na_2EDTA \cdot 2H_2O$. The media composition as tables are included in Appendix 20 to Appendix 23Appendix 28. All cultivations were performed in RAMOS shake flasks and standard shake flasks with a filling volume of 10 mL and a shaking frequency of 350 rpm at a temperature of 37°C. The pre-culture was inoculated from a cryogenic culture to an OD600 of 0.2. The cells were harvested approximately after 7 h in the exponential growth phase and the main-culture was inoculated to an OD600 of 0.5.

Pre-cultures and main-cultures of *Paenibacillus polymyxa* DSM 365 were conducted in MM1P100 medium. The MM1P100 medium contains 5 g/L casein peptone (Carl Roth GmbH & Co., Karlsruhe, Germany), 1.33 g/L $MgSO_4$, 1.67 g/L KH_2PO_4, 0.05 g/L $CaCl_2 \cdot 2H_2O$, 10 mL/L of vitamin solution RMPI 1640 (100x) (Sigma Aldrich, St. Louis, United States) and 1 mL/L of trace solution (1000x). All components were prepared as individual stock solutions. The pH of the KH_2PO_4 solution was adjusted to 7.0 by using KOH. The trace element solution and KH_2PO_4 solution were sterile filtrated. All other solutions were heat sterilized. The trace element solution (1000x) contains 2.5 g/L $FeSO_4 \cdot 7H_2O$, 2.1 g/L $C_4H_4Na_2O_6 \cdot 2H_2O$, 1.8 g/L $MnCl_2 \cdot 4H_2O$, 0.075 g/L $CoCl_2 \cdot 6H_2O$, 0.031 g/L $CuSO_4 \cdot 7H_2O$, 0.258 g/L H_3BO_3, 0.023 g/L

Na_2MoO_4 and 0.021 g/L $ZnCl_2$. For pre-cultures, the medium was prepared with a glucose concentration of 17.5 g/L and for main-cultures with a glucose concentration of 30 g/L, according to Sieben[119]. Appendix 24 and Appendix 25 contain the media composition as tables. Pre-cultures were cultivated in RAMOS shake flasks with a filling volume of 30 mL and a shaking frequency of 300 rpm at a temperature of 30°C. Pre-cultures were inoculated to an OD600 of 0.1 from a cryogenic culture. After approximately 9 h, the cells were harvested in the exponential growth phase and the main-culture was inoculated to an OD600 of 0.5. Main-cultures were carried out in RAMOS shake flasks and standard shake flasks under the same conditions as the pre-cultures, but at a shaking frequency of 200 rpm.

Pre-cultures of Xanthomonas campestris B100 were conducted in Yeast-Malt (YM) medium and were prepared according to Sieben[119]. YM medium contains 10 g/L glucose, 3 g/L yeast extract (Carl Roth GmbH & Co., Karlsruhe, Germany), 3 g/L malt extract (Sigma Aldrich, St. Louis, United States), 5 g/L peptone (Carl Roth GmbH & Co., Karlsruhe, Germany) and 30 g/L MOPS. Appendix 26 contains the medium composition as a table. Complex and non-complex components were prepared with a 10-fold concentration and heat sterilized separately. YM medium was completed by mixing complex and non-complex components and diluting with heat sterilized deionized water. Pre-cultures were inoculated from a cryogenic culture to an OD600 of 0.1. Pre-cultures and main-cultures were carried out with a filling volume of 20 mL and a shaking frequency of 300 rpm at a temperature of 30°C. After 19 - 24 h, main-cultures were inoculated from the pre-culture to an OD600 of 0.5. For the main-cultures, Glucose-Yeast (GY) medium was used, prepared according to Sieben[119]. GY medium contains 25 g/L glucose, 25 g/L yeast extract (Carl Roth GmbH & Co., Karlsruhe, Germany), 2 g/L KH_2PO_4, 0.205 g/L $MgSO_4 \cdot 7H_2O$ and 30 g/L MOPS. Appendix 27 contains the medium composition as a table. Complex and non-complex components were prepared with a 10-fold concentration and heat sterilized separately. GY medium was completed by mixing complex and non-complex components and diluting with heat sterilized deionized water.

3.2.2 Offline analysis

Offline samples were taken from standard shake flasks with paper plugs cultivated in parallel with the ShakeVisc module on the same lab shaker. Each shake flask was sampled two times at most, usually only once, and subsequently discarded. The OD600 was measured with a photometer (Genesys 20, Thermo Scientific, Dreieich, Germany). If not otherwise stated, measurements were performed in triplicate. Samples were diluted with a 9 g/L NaCl solution

to an OD600 of 0.1 - 0.3. The offline pH value of the cultivation broth was measured with a pH meter (HI221 Microprocessor pH Meter, Hanna Instruments, Vöhringen, Germany) at room temperature. If not otherwise stated, measurements were performed as duplicates. The offline viscosity was measured with a rheometer (Physica MCR 301, Anton Paar GmbH, Ostfildern-Scharnhausen, Germany) at the respective cultivation temperature as triplicates, unless otherwise stated. A cone-plate system (CP50-0.5/TG, cone truncation 56 µm, cone angle 0.475°) was used. A logistic shear rate ramp of 10 – 5000 s^{-1} was applied. Since viscous cultivation broths are typically of non-Newtonian behavior, the apparent viscosity is dependent on the effective average shear rate in the shake flask. Therefore, the shear rate in the shake flask at each individual sampling point must be calculated as the shear rate is dependent on the viscosity and strictly speaking, on the flow consistency index K. Hence, the shear rates in shake flasks were calculated individually for each sampling point under cultivation conditions. Subsequently, the apparent viscosities were derived from offline rheometer measurements. The procedure is described by Giese et al.[7] and Sieben et al.[64]. When measurements were performed as triplicates, error bars represent the standard deviation. When measurements were performed as duplicates, error bars represent minimum and maximum values.

3.2.3 Measurement device

A computer-aided design (CAD) drawing of the newly developed ShakeVisc module is shown in Fig. 3-1. The base plate contains an acceleration sensor, a microcontroller and a port for data communication with a computer. Three optical sensors for monitoring DOT, biomass, pH value and viscosity are arranged at an angle of 120° to each other and are attached to the shake flask at the point of the widest diameter. This position corresponds to a height of 16 mm, measured from the bottom of the shake flask. To measure the DOT signal, oxygen-sensitive Oxnano nanoparticles (PyroScience GmbH, Aachen, Germany) were used. The Oxnano nanoparticles contain oxygen sensitive dyes and have a hydrophilic vinylpyrrolidone shell. The measurement principle relies on the oxygen-depending quenching behavior of the fluorescent dyes[100,120]. To read out the fluorescence signal, an optoelectronic sensor with an excitation wavelength of 610 – 630 nm was used. The emission wavelength was measured in the near-infrared range with a wavelength of 760 – 790 nm. For online monitoring of the pH value, self-adhesive pH sensor spots (PyroScience GmbH, Aachen, Germany) were used. The pH sensor spots include two fluorescent dyes. One dye is pH insensitive, whereas the other dye shows a pH sensitive fluorescence behavior[111]. To read out the fluorescence signal of the pH spot, an additional optoelectronic sensor with an excitation wavelength of 610 – 630 nm was used. The emission

wavelength was also measured in the near-infrared range with a wavelength of 760 – 790 nm. The biomass signal was correlated to the online monitored scattered light signal. Therefore, a third optoelectronic sensor with a wavelength of 610 – 630 nm was used, and the backscattered light was recorded. The online measured viscosity was derived from the shift of the bulk liquid in relation to the centrifugal acceleration, described in chapter 3.2.4.

Fig. 3-1: Prototype of ShakeVisc module for online monitoring of dissolved oxygen tension, pH value, biomass and viscosity with three optical sensors.

One optical sensor is used with Oxnano nanoparticles, dispersed in the liquid phase, to monitor the DOT. A second optical sensor, in conjunction with a self-adhesive pH spot, is used to measure the pH value. The pH spot is attached to the inner wall of the shake flask. The third optical sensor monitors the biomass by scattered light measurements. Online monitoring of the viscosity does not require its own sensor but can be performed based on the DOT or scattered light sensor. The optical sensors were arranged at an angle of 120° to each other and were attached to the shake flask at the point of the widest diameter (16 mm from bottom of the shake flasks). To allow for triggering of the optical sensors, when the rotating bulk liquid is in front of the sensor, the ShakeVisc module is equipped with an acceleration sensor. Alternatively, a hall sensor is attached to the lab shaker. The power supply and cables are not shown.

The ShakeVisc module was combined with a RAMOS device, as shown in Fig. 3-2. The measurement principle of the RAMOS technology is described elsewhere[90,121]. A computer was used for data recording and evaluation. Additionally, cultivation in shake flasks for manual sampling and offline measurements were cultivated on the same lab shaker.

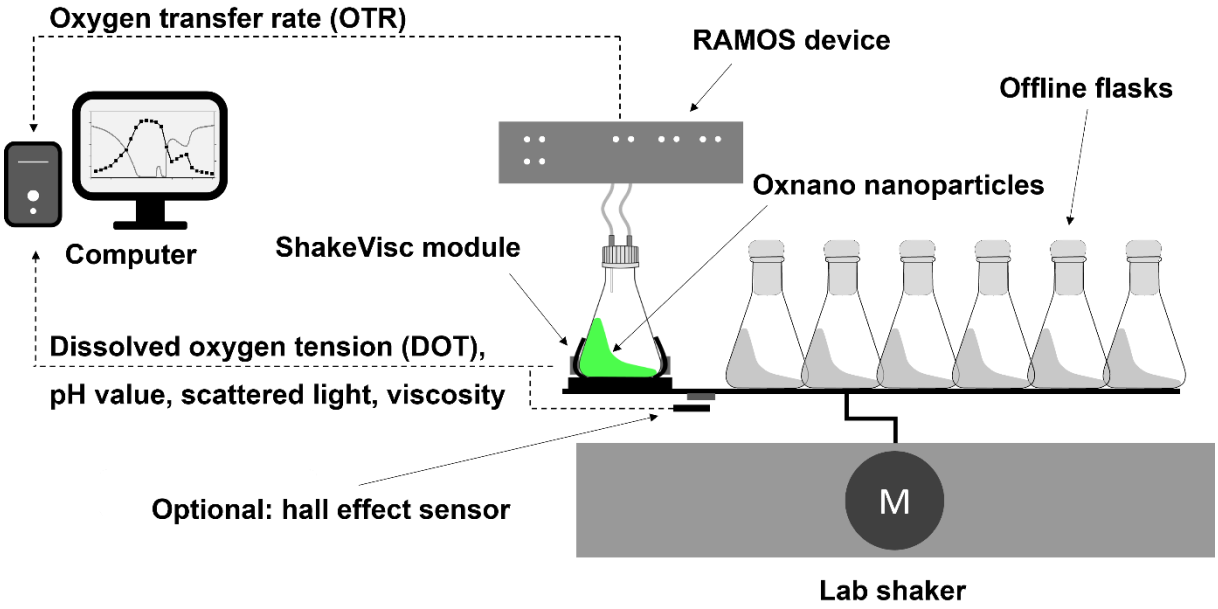

Fig. 3-2: Experimental setup for online measurement of dissolved oxygen tension, pH value, biomass and viscosity with the ShakeVisc module and online measurement of oxygen transfer rate with a RAMOS device.

The optical sensors in the ShakeVisc module are arranged at an angle of 120° to each other. Additionally, offline shake flasks for manual sampling and offline analysis are cultivated in parallel in the same temperature controlled shaker cabinet. To allow for triggering of the measurement of the rotating bulk liquid, the ShakeVisc module is equipped with an acceleration sensor. Alternatively, a hall effect sensor is attached to the lab shaker.

3.2.4 Detection of the leading edge of the rotating bulk liquid

To accurately monitor cultivations, measurement of the DOT must be performed in the rotating bulk liquid[98,99]. Therefore, the movement of the bulk liquid was monitored based on the fluorescent signal intensity of the Oxnano nanoparticles suspended in the cultivation broth. With this information, the leading edge of the rotating bulk liquid can be identified and the measurement of the DOT in the bulk liquid can be triggered. The measurement of the scattered light signal was triggered in the same fashion. The principle of the tracking the bulk liquid and determination of the trigger point is shown in Fig. 3-3.

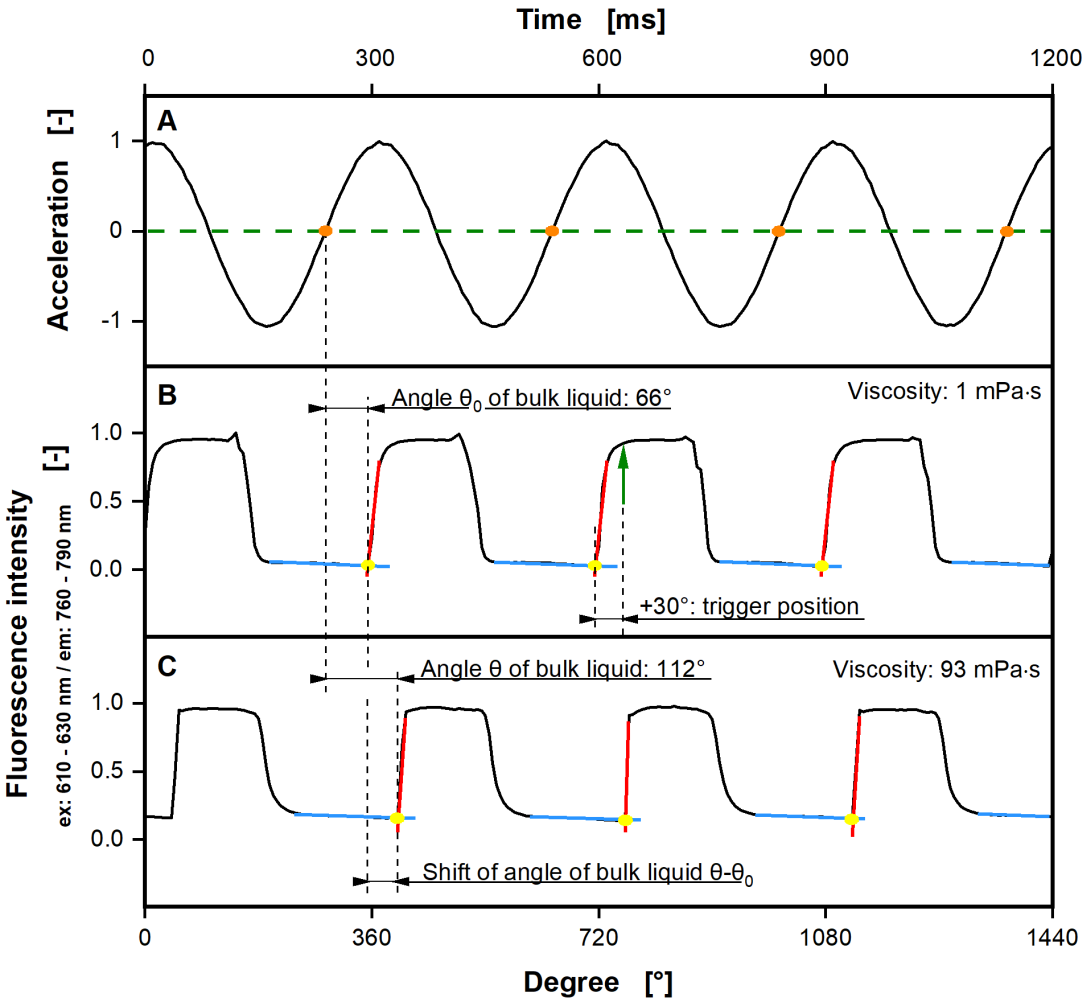

Fig. 3-3: Detection principle of the shift of the angle of the leading edge of the rotating bulk liquid θ-θ_0.

θ_0 marks the angle at the beginning of the cultivation, whereas θ marks the angle at any other time point. (A) Normalized signal of the acceleration sensor of four consecutive rotations. The intersection of the rising slope with the zero level (horizontal dashed green line) marks the first point used for the detection of the angle of the leading edge of the rotating bulk liquid (orange dots). (B) Normalized intensity signal of Oxnano nanoparticles in cultivation broth of four consecutive rotations at low viscosity of 1 mPa•s. The rising slope indicates the leading edge of the rotating bulk liquid. The falling slope indicates the following tail of the rotating bulk liquid. Intersection (yellow dots) of the base signal (blue solid line) with the rising slope of the signal of the rotating bulk liquid (red solid line) indicates the second point used for the detection of the angle θ_0 of bulk liquid. The trigger position for measurement of dissolved oxygen tension (DOT) and scattered light is located 30° after the leading edge of the rotating bulk liquid. For clarity, the trigger position is marked in the subsequent rotation of the bulk liquid (vertical green arrow). (C) Normalized intensity signal of Oxnano nanoparticles in cultivation broth of four consecutive rotations at elevated viscosity of 93 mPa•s. Due to the increased viscosity, the angle θ of bulk liquid increases from 66° to 112°. The shift of angle of bulk liquid θ-θ_0 is used as a correlation to viscosity. Cultivation of *Paenibacillus polymyxa*, filling volume (V_L) = 30 mL, shaking frequency (n) = 200 rpm, shaking diameter (d_0) = 50, temperature (T) = 37°C, 0.2 mg/mL Oxnano nanoparticles.

In Fig. 3-3A, the signal of the acceleration sensor, integrated in the ShakeVisc module, is shown for four consecutive rotations. For a shaking frequency of 200 rpm, one rotation of the bulk liquid (360°) takes 300 ms. The intersection of the rising slope of the acceleration signal with

the zero level (horizontal green dashed line) marks the reference point used for the detection of the leading edge of the rotating bulk liquid (orange dots). In Fig. 3-3B, the normalized fluorescence intensity of the Oxnano nanoparticles in the rotating bulk liquid is shown for four consecutive rotations at a water-like viscosity of 1 mPa•s. The rising slope (red solid line) indicates the leading edge of the rotating bulk liquid. The falling slope indicates the following tail of the rotating bulk liquid. The base signal is indicated by the blue solid line. The intersection of the base signal and the rising slope of the leading edge (yellow dots) is defined as the characteristic value of the leading edge. The difference between this characteristic value of the leading edge and the reference point of the acceleration sensor (orange dots) in Fig. 3-3A is calculated as the angle θ of the bulk liquid. The angle θ_0 of the bulk liquid characterizes this angle at the beginning of the cultivation. In this example, the difference between the reference point (orange dots) and the second point (yellow dots) is an angle of 66°. The trigger position for measurement of DOT and scattered light is located 30° after the leading edge of the rotating bulk liquid (vertical green arrow in Fig. 3-3B). In Fig. 3-3C, the normalized fluorescence intensity of the Oxnano nanoparticles in the rotating bulk liquid is shown for four consecutive rotations at an elevated viscosity of 93 mPa•s. The detection of the leading edge of the rotating bulk liquid takes place analogously to Fig. 3-3B. Due to increased internal friction in the rotating bulk liquid, caused by the elevated viscosity, the angle θ of bulk liquid increased to 112°. A schematic view of the position of the rotating bulk liquid at two different exemplary viscosities with illustration of the angle θ of the bulk liquid can be seen in Appendix 19. As discussed previously and shown by Sieben et al.[64] and Ladner et al.[66], the shift of the angle θ of the bulk liquid correlates to the change in viscosity of Newtonian and non-Newtonian fluids. Thus, the shift of angle of bulk liquid θ-θ_0 is introduced and used as an online monitoring signal for the viscosity. In this example, an increase in viscosity from 1 mPa•s to 93 mPa•s leads to a shift of the angle of the bulk liquid θ-θ_0 of 46° (see Fig. 3-3C). It is also possible to perform a calibration of the viscosity measurement of the ShakeVisc system. This calibration must be performed for each cultivation condition (e.g., filling volume, shaking frequency, temperature, etc.). An example is shown in Appendix 28 and Appendix 29. Alternatively, calibration could also be performed using CFD data. CFD can be used to reliably predict the liquid movement and position of the leading edge, as demonstrated in chapter 2.

3.2.5 Calibration of pH and DOT sensors

Self-adhesive pH sensor spots (PyroScience GmbH, Aachen, Germany) were glued on the inner glass wall of the RAMOS flasks at the point of the largest inner diameter. The RAMOS flasks

were then autoclaved at 121°C for 20 min. Prior to each experiment, the pH sensor spots were soaked overnight in sterile deionized water. Subsequently, if not otherwise stated, a calibration of the pH sensor spots was performed. Therefore, under sterile conditions, calibrations were conducted with a pH 2 and a pH 11 buffer solution. Firstly, sterile pH 2 buffer solution was filled in the RAMOS flasks and was tempered at the respective cultivation temperature. Then, the pH calibration was performed. RAMOS flasks were rinsed twice with sterile deionized water after the pH 2 calibration. Subsequently, pH 11 buffer solution was filled in the RAMOS flasks and tempering, calibration and rinsing with sterile deionized water were repeated. Furthermore, depending on the experiment, the offline measured pH value at the beginning of the cultivation was used to recalibrate a possible offset of the online measured pH value, to increase the accuracy of the online measurement.

Oxnano nanoparticles for the DOT measurements (PyroScience GmbH, Aachen, Germany) were prepared in stock suspension of 5 mg/mL by mixing dried Oxnano nanoparticles with deionized water. Some batches of Oxnano nanoparticles did not fully disperse in deionized water but remained in small clumps. In these cases, stock solutions were treated with ultrasonication until the Oxnano nanoparticles were completely dispersed. For ultrasonication, a sonic dismembrator (Fisherbrand^{TM} Model 120 Sonic dismembrator, Fisher Scientific GmbH, Schwerte, Germany) was used. The amplitude was set to 80 % and ultrasonication was conducted for a total of 10 min, with repetitive cycles of 4 s of treatment, followed by 4 s of pause. During ultrasonication, the sample was stored on ice. Afterwards, the prepared stock suspension was sterilized by autoclaving at 121°C for 20 min. Sterile Oxnano nanoparticles stock suspension was then added to the cultivation media, during final media preparation at a final concentration of 0.2 mg/mL for all experiments. Added Oxnano nanoparticle stock solution replaced the required volume of deionized water in media compositions to avoid dilution effects. The volume of left out deionized water corresponds to the volume of added Oxnano nanoparticles stock suspension. Prior to the experiment, the DOT was calibrated to 100 % air saturation. Therefore, the prepared cultivation medium containing the Oxnano nanoparticles was filled in RAMOS flasks and was shaken and tempered at cultivation conditions. When the oxygen concentration in the air and liquid phase were in equilibrium, the DOT calibration was conducted.

3.2.6 Relevance of the out-of-phase phenomenon for cultivations at elevated viscosities

Cultivations at elevated viscosities, as they are presented in this chapter, might be affected by the out-of-phase phenomenon. Effects of elevated viscosity on shake flasks experiments has been explored in great depth with the help of CFD in chapter 2 of this thesis. In short, the out-of-phase phenomenon describes experimental conditions in shake flasks, under which the centrifugal force from the orbital shaking motion is too weak to accelerate the bulk liquid. The bulk liquid in the shake flasks does not follow the shaking motion of the lab shaker anymore and essentially sticks to the bottom of the shake flask. Büchs et al.[3,4] first described the out-of-phase phenomenon and the resulting, negative effects on shake flask experiments. Although the shift from in-phase to out-of-phase is a steady process, as shown in chapter 2, Büchs et al.[4] developed the dimensionless phase number. They aimed at quantifying for practical use the order of magnitude to which a shake flask experiment is out-of-phase with the shaking motion. They derived a critical phase number of 1.26, characterizing experimental conditions with phase numbers below 1.26 as out-of-phase. Azizan et al.[5] later reassessed the out-of-phase phenomenon and found a critical phase number of 0.91, characterizing conditions with a significant change of the liquid shape and flow. While Büchs et al.[4] derived their critical phase number from measurements of the volumetric power input in shake flasks, Azizan et al.[5] used recorded liquid distributions as the basis for their critical phase number. The definition of the phase number is given in Eq. 25 in chapter 2 of this thesis.

3.3 Results and Discussion

3.3.1 Non-triggered DOT, scattered light and pH measurements

To emphasize the necessity of using a trigger signal for optimal online monitoring with the ShakeVisc module, a non-triggered online monitoring of an *E. coli* cultivation is shown in Fig. 3-4. As discussed previously, the online monitoring of viscosity is only enabled by tracking the bulk liquid position, hence, it is not possible in the non-triggered setup.

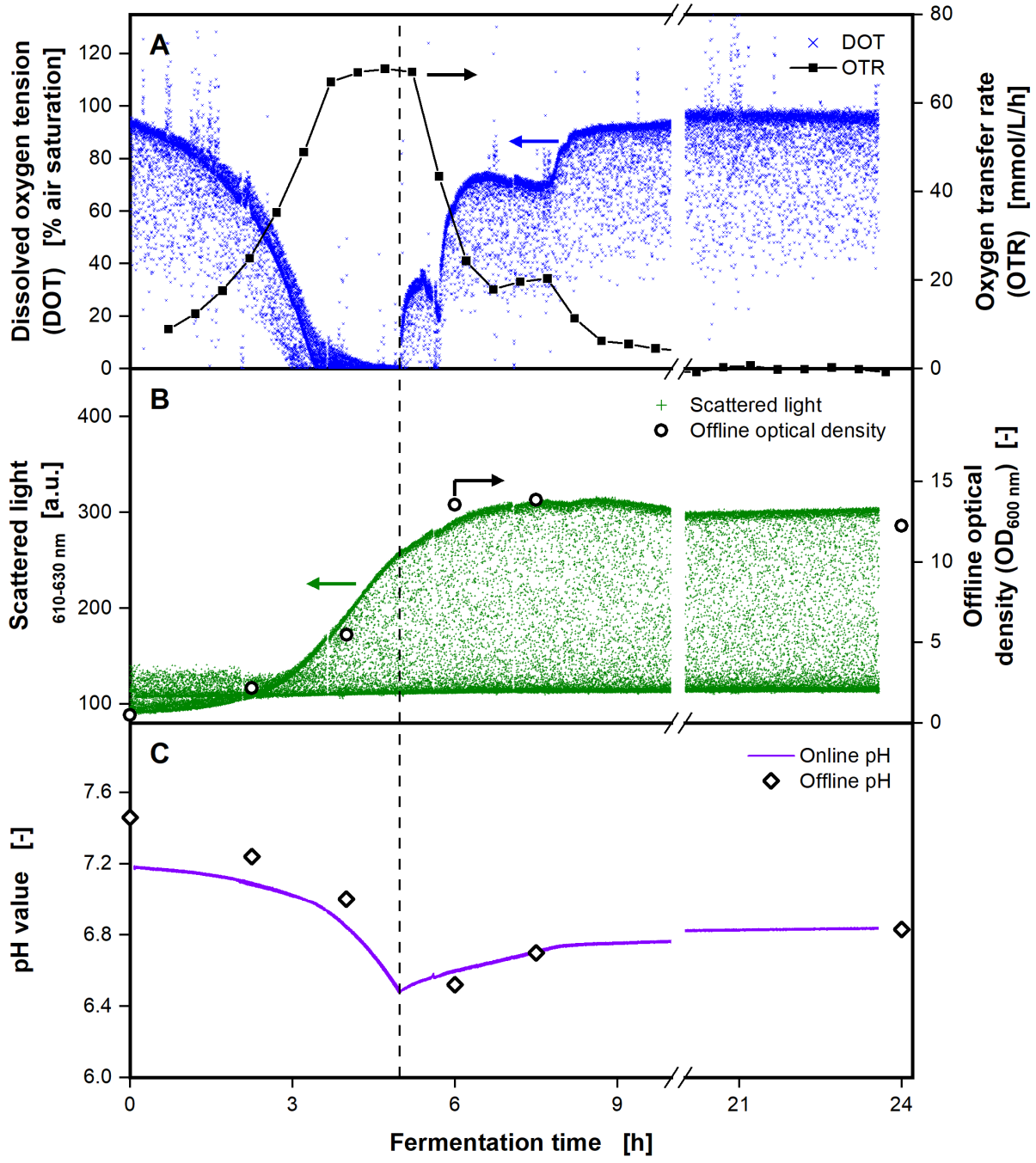

Fig. 3-4: Online monitoring of an *Escherichia coli* cultivation with a non-triggered ShakeVisc device and a RAMOS device.

(A) Online monitoring of dissolved oxygen tension (DOT) and oxygen transfer rate (OTR), with Oxnano nanoparticles and a RAMOS device, respectively. The DOT was calibrated to 100 % in the inoculated medium prior to starting the monitoring. (B) Online monitoring of scattered light, compared to optical density measurements from offline samples at 600 nm. (C) Online monitoring of the pH value with pH sensitive spots, compared to pH measured from offline samples. The pH spot was calibrated at pH 2 and 11 before the cultivation. All offline samples were taken from shake flasks cultivated in parallel. The vertical dashed line indicates the sudden change in the trend of DOT and pH value after 5 hours. Cultivation conditions: Wilms-MOPS medium with 20 g/L glucose, 0.2 mg/mL Oxnano nanoparticles, range of pH spot = 6 – 8, initial pH = 7.5, initial OD_{600} = 0.5, shaking frequency (n) = 350 rpm, filling volume (V_L) = 10 mL, shaking diameter (d_0) = 50 mm, temperature (T) = 37°C. Offline optical density OD_{600} and offline pH was measured in single measurement.

Most of the DOT measurements closely mirror the recorded OTR, as can be seen in the thick upper boundary of data points in Fig. 3-4A. However, many data points do not follow this trend and mostly show lower DOT values. Due to the rotation of the bulk liquid and the non-triggered measurement, only a portion of the data points are taken when the rotating bulk liquid is in front of the sensor. Remaining measurements occur when the liquid film is in front of the sensor. While the thick upper boundary of DOT values represents the bulk liquid, the rest of the data points represent the liquid film. However, as previously discussed, the DOT in the liquid film is expected to be higher or at least equal to the rotating bulk liquid, but never lower[1,2]. The underestimation of the measured DOT in the liquid film, compared to the literature, is caused by the small number of Oxnano nanoparticles and, hence, low signal intensity in the liquid film. The signal intensity in the liquid film is at approximately 1 mV (see lower boundary in Appendix 30). In contrast, measurements in the bulk liquid led to significantly higher signal intensities of up to 125 mV. Importantly, the signal intensity in the bulk exceeds the threshold value of 25 mV during the first 15 h of cultivation. The signal intensity in the bulk liquid only falls below 25 mV to roughly 22 mV during the last hours of cultivation. Beneath a signal intensity of 25 mV the DOT determined by the Oxnano nanoparticles system is influenced by the signal intensity. Above 25 mV the DOT determined by the Oxnano nanoparticle system is entirely independent from the signal intensity and can be determined solely by the phase shift.

Yet, as stated above, most DOT values mirror the OTR. In the first 4 h, during the exponential growth of the organism, an exponential decrease from 95 % air saturation is observed. Then, oxygen becomes limiting in the cultivation as the saturation drops to 0 %. The same observations can be drawn from the OTR. DOT and OTR, however, do not agree on the duration of the oxygen limitation. The OTR drops from the maximum value of 67 mmol/L/h after 5.5 h, while the DOT suggests a slightly shorter oxygen limitation phase until 5 h. After the oxygen limitation and complete depletion of the glucose, further products are metabolized[122]. The OTR drops from the oxygen limitation to a second plateau at roughly 20 mmol/L/h after 6 h and

remains there for approximately 1.5 h. This second OTR peak is known to represent the consumption of acetate, which is produced by *E. coli* at DOT values below 30 % air saturation[123]. In contrast to the OTR, an additional peak can be recognized in the recorded DOT after the oxygen limitation. Over a duration of 1 hour, the DOT increases up to 35 % air saturation, before decreasing again to approximately 20 %. This feature is concealed by the relatively low measurement frequency of the quasi-continuous OTR measurement by the RAMOS device in the presented cultivation. In this experiment, one data point is acquired every 30 minutes by the RAMOS device. However, by coincidence, in a similar cultivation, this first temporary increase in DOT after the oxygen limitation was detected by the RAMOS device (see Appendix 31). This temporary increase in DOT must represent some produced organic acid or other substance. Following this peak, between hours 6 and 7.5 of the fermentation, the DOT shows a plateau at about 70 % air saturation during the consumption of acetate, mirroring the OTR again. After the depletion of acetate, the metabolic activity quickly slows down until 8 h, finally reaching an OTR of 0 mmol/L/h and DOT of 100 % air saturation after 20 h.

The scattered light measurements in Fig. 3-4B are affected by the missing trigger in the same way as the DOT measurement in Fig. 3-4A. However, in contrast to the DOT, the recorded scattered light is enclosed in two distinct boundaries. A nearly constant, lower boundary at approximately 110 a.u. represents measurements in the liquid film. An upper boundary, which increases over the fermentation time, represents measurements in the rotating bulk liquid. Interestingly, during the first 2.5 h of fermentation, the scattered light signal from the rotating bulk liquid is lower than from the liquid film.

Results from the scattered light module support the conclusions drawn from the DOT and OTR signals. The scattered light exponentially increases in the first 4 h from 90 to 180 a.u.. Subsequently, during the oxygen limitation, the scattered light increases nearly linearly to 270 a.u.. Then, the scattered light begins to level off, reaching its maximal value of 310 a.u. after acetate is consumed at approximately 6 h. The scattered light remains nearly constant until the end of cultivation after 24 h, only declining slightly to 300 a.u.. This course of the biomass is confirmed by the offline optical density measurements, which were taken every 2 h for the first 8 h and after 24 h.

Lastly, the online pH was measured and compared to conventional offline pH measurements, as shown in Fig. 3-4C. As expected, the online measurement of the pH value is, in contrast to DOT and scattered light, not affected by the shaking motion. It indicates reliable online values with low noise. The recorded online pH drops slightly during the first 4 h of exponential growth,

from a pH of 7.2 to 7.0. Afterwards, a sharp decrease of the online pH during the oxygen limitation (see Fig. 3-4A) to a pH of 6.45 is observed. This acidification matches the already discussed formation of mostly acetate by *E. coli* during oxygen limitation[123]. Following this pH minimum, the online pH slowly starts increasing again, reaching a nearly constant pH of 6.75 after 9 h. Until 24 h, the pH further increased slightly to a value of 6.8. The increasing pH fits the already discussed consumption of products like acetate, following the depletion of glucose. Over the entire duration of the cultivation, the offline pH measurements closely follow the trajectory of the online pH. However, the offline pH is roughly 0.1 to 0.2 pH units higher than the online signal during the first 4 h of cultivation and 0.05 pH units lower at 6 h. It should be noted that the minimal online pH value and, therefore, the switch from production to consumption of acidic components occurs after 5 h. This precisely matches and confirms the shorter oxygen limitation indicated by the DOT (see vertical dashed line in Fig. 3-4), compared to the OTR.

Despite the alternating signal for DOT and scattered light, due to the missing trigger signal, the online signals of the bulk liquid are already reproducible and closely correlated with the available reference signals, i.e., OTR, offline optical density and offline pH measurements. The online monitoring of the ShakeVisc system, however, is far superior in terms of measurement frequency, compared to offline sampling and the quasi-continuous OTR. Compared to the OTR, the increased frequency of the DOT measurement unveiled the consumption of an additional carbon source, between 5 – 6 h of the presented *E. coli* cultivation.

3.3.2 Triggered sensors reveal metabolic shift in *E. coli*

In the following experiments, the ShakeVisc system is upgraded with a trigger signal, to selectively monitor only the rotating bulk liquid. Using an acceleration sensor and the fluorescence intensity signal of the Oxnano nanoparticles, the leading-edge position of the bulk liquid was detected. The principle of detecting the leading edge of the rotating bulk liquid by using the fluorescence signal of the Oxnano nanoparticles are discussed in chapter 3.2.4. The results of the triggered *E. coli* cultivation are presented in Fig. 3-5.

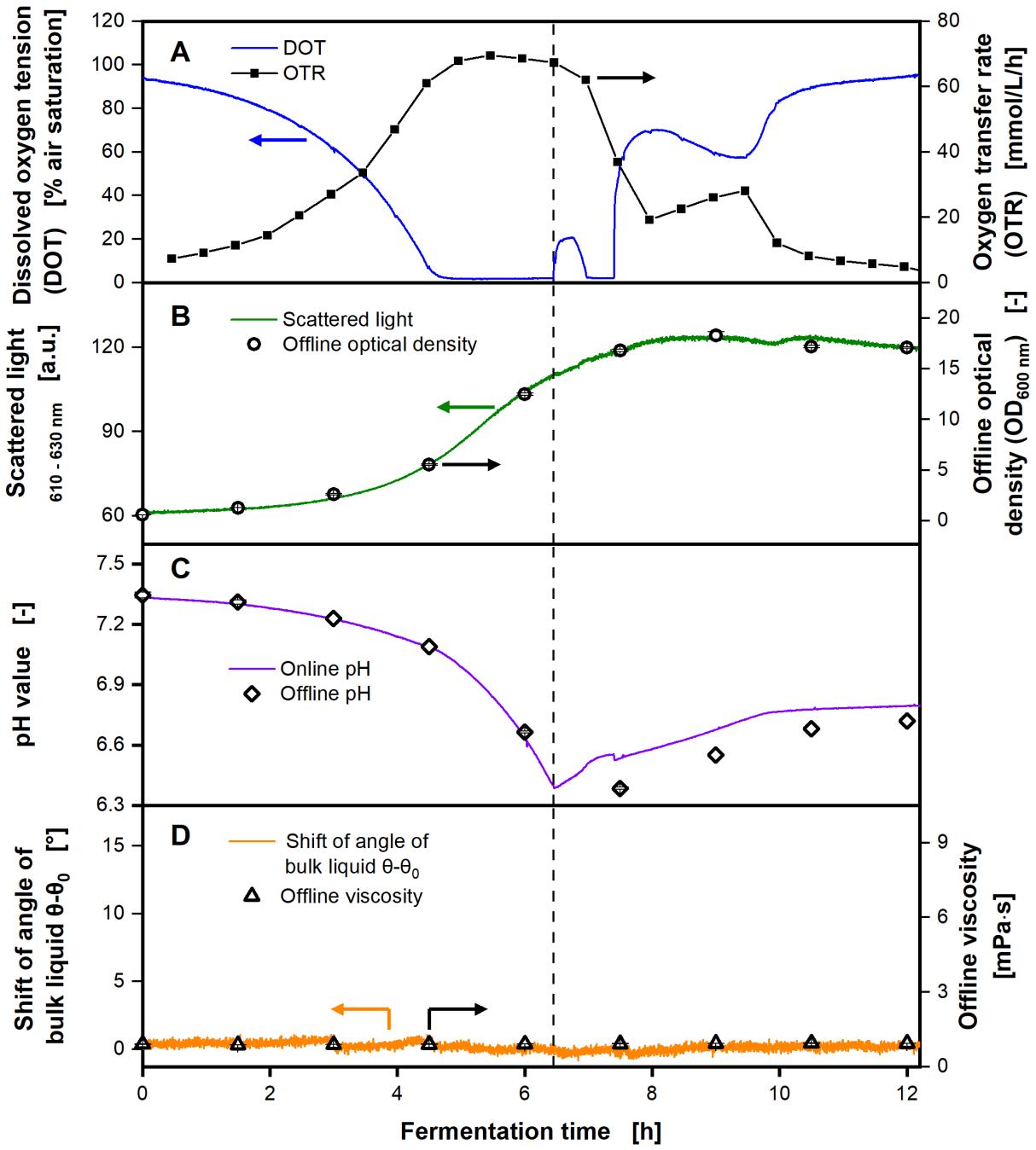

Fig. 3-5: Online monitoring of an *Escherichia coli* cultivation with a triggered ShakeVisc device and a RAMOS device.

(A) Online monitoring of dissolved oxygen tension (DOT) and oxygen transfer rate (OTR), with Oxnano nanoparticles and a RAMOS device, respectively. The DOT was calibrated to 100 % in the non-inoculated medium prior to starting the monitoring. (B) Online monitoring of scattered light, compared to optical density measurements from offline samples at 600 nm. (C) Online monitoring of the pH value with pH sensitive spots, compared to offline pH, measured from offline samples. The pH spot was calibrated at pH 2 and 11 before the cultivation. Additionally, a pH-offset calibration was performed. (D) Online monitoring of the shift of angle of bulk liquid θ-θ_0, compared to the offline viscosity, measured from offline samples with a rheometer. All offline samples were taken from separate shake flasks, cultivated in parallel. The vertical dashed line indicates the sudden change in the trend of DOT and pH after 6.5 hours. Triggering of the measurement of the bulk liquid was enabled by an acceleration sensor, according to the illustration in Fig. 3-3B. Cultivation conditions: Wilms-MOPS medium with 20 g/L glucose, 0.2 mg/mL Oxnano nanoparticles, range of pH spot = 6 – 8, initial pH = 7.5, initial OD_{600} = 0.5, shaking frequency (n) = 350 rpm, filling volume (V_L) = 10 mL, shaking diameter (d_0) = 50 mm, temperature (T)

= 37°C. Standard deviation is barely visible, as it is smaller than the data points. Offline viscosity measurements were performed in duplicate.

In Fig. 3-5A, the online monitored DOT and OTR signals are shown. In contrast to the untriggered measurement (see Fig. 3-4), it is striking that the DOT value now shows a sharply defined course. Since all measurements take place in the rotating bulk liquid, no more outliers are present. The courses of DOT and OTR resemble those of the untriggered *E. coli* cultivation (see Fig. 3-4).

In Fig. 3-5B, the online monitored scattered light signal is compared to the offline measured optical density. Like the DOT signal, the successful triggering of measurements leads to a sharply defined scattered light signal without any outliers. The course of the triggered scattered light signal matches with the upper boundary layer of the scattered light signal of the untriggered scattered light measurement (see Fig. 3-4B). The online monitored scattered light signal perfectly correlates to the offline measured OD_{600} samples. Moreover, by using the data of the online monitored OTR and the online monitored scattered light, it is possible to calculate the online monitored specific oxygen uptake rate (qO_2) (see Appendix 32). During the initial exponential growth phase, OTR and scattered light values are increasing. During this phase, as shown in the supplement (see Appendix 33 to Appendix 38), the calculated qO_2 values correlate well with qO_2 values from literature. This is a further validation of the measurements conducted with the ShakeVisc system.

In Fig. 3-5C, the online monitored pH value is compared to the offline measured pH value. The online monitored pH value is similar to the course of the online monitored pH value in the untriggered *E. coli* cultivation (see Fig. 3-4C). The pH values measured offline match the course of the online measured pH values. At the beginning of the cultivation, the online and offline measured values perfectly match each other, until the pH value reaches its minimum value of 6.4, after a cultivation time of 6.5 h. Afterwards, a slight deviation in online and offline measured pH values with a maximum deviation of 0.15 is apparent. Subsequently, with increasing pH values, the gap between both values diminishes, leading to a deviation of only 0.07 at the end of the cultivation. Most likely, the performance of the sensor spot is superior near its pK_a value and additional changes in the composition of the cultivation medium over the course of the cultivation might affect the pH sensor.

In Fig. 3-5D, the shift of angle of bulk liquid θ-θ_0 (see Fig. 3-3) is compared to the offline measured viscosity. Enabled by monitoring the signal intensity of the Oxnano nanoparticles,

suspended in the cultivation broth, the leading edge of the rotating bulk liquid can precisely be determined (see Appendix 39). The shift of the angle of the bulk liquid θ-θ_0 stays at the same level during the cultivation and can be correlated to the apparent viscosity in the shake flask. Offline samples of the cultivation broth, measured with a rheometer as duplicates, perfectly correlate to the online signal, showing constant water-like viscosities of about 0.9 mPa·s.

To investigate the origin of the DOT peak in Fig. 3-5A during the oxygen limitation, after a fermentation time of 6.5 h, an additional fermentation with multiple sampling steps during the relevant period was conducted (see Appendix 31). The results of the HPLC measurement are presented in Fig. 3-6.

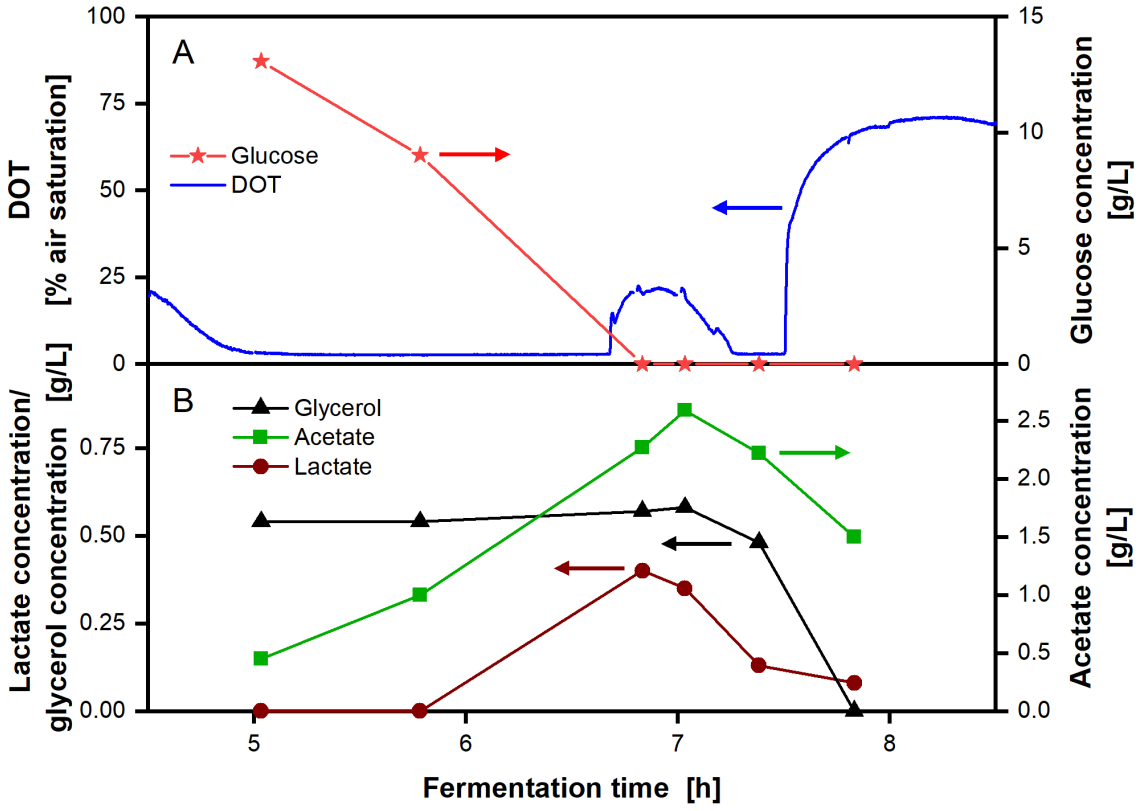

Fig. 3-6: Offline sampling of an *Escherichia coli* cultivation during the period of oxygen limitation.

All samples were taken from shake flasks, cultivated in parallel. Samples were immediately stored on ice, to stop metabolic activities. Triggering of the measurement of the bulk liquid was enabled by an acceleration sensor, according to the illustration in Fig. 3-3B. Cultivation conditions: Wilms-MOPS medium with 20 g/L glucose, 0.2 mg/mL Oxnano nanoparticles, range of pH spot = 6 – 8, initial pH = 7.5, initial OD_{600} = 0.5, shaking frequency (n) = 350 rpm, filling volume (V_L) = 10 mL, shaking diameter (d_0) = 50 mm, temperature (T) = 37°C. All online and offline data of this cultivation are shown in Appendix 31.

In Fig. 3-6A, it becomes apparent that glucose is entirely consumed at the end of the oxygen limitation, after a fermentation time of approximately 6.5 h. Thus, the highly time-resolved DOT measurement, enabled by the ShakeVisc device, allows the precise detection of the time point of glucose depletion. If, on the other hand, only the OTR data, provided by the RAMOS technique, is regarded (see Fig. 3-5A), the exact time point of glucose depletion might be missed. However, as already stated, in a similar cultivation (see Appendix 31), by coincidence, the exact time point of glucose depletion was detected. During the first part of the oxygen limitation, significant amounts of acetate are formed (see Fig. 3-6B). Also, lactate is produced at the end of the first part of oxygen limitation. The detected amounts of glycerol (0.5 g/L) are likely carryovers from the pre-culture, since the pre-culture was inoculated with a glycerol-containing cryogenic culture (Estimations of glycerol carryover can be seen in Appendix 40). The consumption of acids (acetate and lactate) started at the end of the first period of oxygen limitation. It is also indicated by the increase of the pH value (see Appendix 31). During the second period of oxygen limitation, glycerol, lactate, and acetate seem to be consumed simultaneously. At the end of the second oxygen limitation, glycerol is entirely exhausted. The remaining amounts of acetate are consumed during the increase of the DOT after 7.5 h. It could be shown that the DOT peak of 20 % during the oxygen limitation can be traced back to glycerol carryovers from the pre-culture. This emphasizes the necessity of washing the pre-culture, when defined cultivation conditions have to be ensured. Presumably, the influence of glycerol carryovers on the DOT could not be detected by Flitsch et al.[99], since two subsequent pre-cultures were conducted, diluting the remaining glycerol. This effect remains non-disclosed by the quasi-continuous measuring principle of the RAMOS device. In contrast, the highly time-resolved DOT measurement demonstrates the capabilities of the ShakeVisc device.

3.3.3 Online viscosity monitoring based on Oxnano nanoparticles

In a subsequent experiment, the ShakeVisc system was applied to a cultivation of *Paenibacillus polymyxa,* which is a natural producer of extracellular polysaccharides and, thus, leads to changes in the viscosity during the cultivation. The results are shown in Fig. 3-7. The results of a non-triggered *Paenibacillus polymyxa* cultivation are shown in the supplement in Appendix 41.

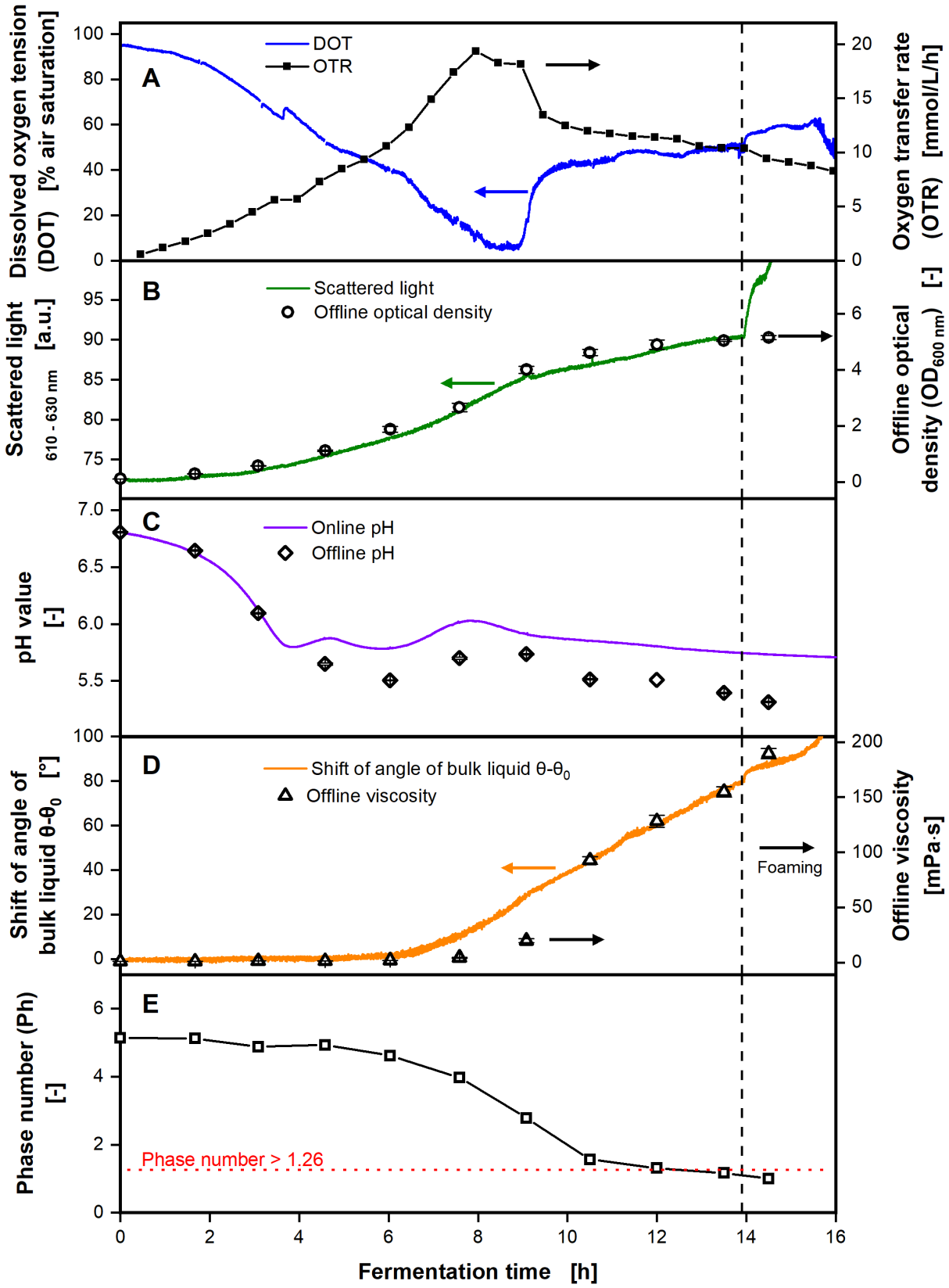

Fig. 3-7: Online monitoring of a *Paenibacillus polymyxa* cultivation with a triggered ShakeVisc device and a RAMOS device.

(A) Online monitoring of dissolved oxygen tension (DOT) and oxygen transfer rate (OTR), with Oxnano nanoparticles and a RAMOS device, respectively. The DOT was calibrated to 100 % in the non-inoculated medium prior to starting the monitoring. (B) Online monitoring of scattered light, compared to optical density measurements from offline samples at 600 nm. (C) Online monitoring of the pH value with pH

sensitive spots, compared to offline pH, measured from offline samples. The pH spot was not calibrated before the cultivation. (D) Online monitoring of the shift of angle of bulk liquid θ-θ_0, compared to the offline viscosity, measured from offline samples with a rheometer. (E) Phase number (Ph) according to Eq. 25 calculated from offline measured viscosity. The horizontal red dotted line marks the critical phase number of 1.26. The vertical dashed line indicates the beginning of foaming of the cultivation, associated by the sharp increase in scattered light signal (B). All offline samples were taken from shake flasks, cultivated in parallel. Triggering of the measurement of the bulk liquid was enabled by an acceleration sensor, according to the illustration in Fig. 3-3B. Cultivation conditions: MM1P100 medium with 30 g/L glucose, 0.2 mg/mL Oxnano nanoparticles, range of pH spot = 5 – 7, initial pH = 7, initial OD_{600} = 0.5, shaking frequency (n) = 200 rpm, filling volume (V_L) = 30 mL, shaking diameter (d_0) = 50 mm, temperature (T) = 30°C. Standard deviation is barely visible, as it is smaller than the data points.

In Fig. 3-7A, the course of the DOT and OTR are depicted over the fermentation time. During the first 8 h of cultivation, the DOT continuously decreases until reaching a value of 5 % air saturation. The DOT remains at this level for 1 h and sharply starts increasing afterwards up to a DOT value of 40 %. Subsequently, the DOT further increases slightly. After 14 h, the online monitored shake flask and all remaining offline shake flasks started foaming, indicated by the dashed black vertical line. A picture of the foaming shake flasks at the end of the cultivation is provided in the supplement in Appendix 42. This effect is also visible in the DOT signal, as the DOT value suddenly increases. After this time point, the DOT is no longer reliable. The OTR values mirror the DOT values. However, the time point of foaming is not apparent in the OTR signal.

In Fig. 3-7B, the online monitored scattered light and the offline measured optical density OD_{600} are shown. During the first 9 h, as the DOT is decreasing and remains at a low level, the scattered light signal rises from 70 a.u. to 85 a.u. with an increasing slope. When the DOT starts to increase at the end of the oxygen limitation, the scattered light signal also increases further up to 90 a.u., but with a reduced slope. The online-measured scattered light signal perfectly matches the offline-measured optical density. The time point of foaming, indicated by the vertical black dashed line, is clearly visible in the scattered light signal, associated with a sharp increase in the measured value. Similar to the DOT value, the scattered light signal can no longer be used to reliably monitor the biomass.

In Fig. 3-7C, the online monitored pH value is compared to the offline measured pH value. The online measured pH value decreases exponentially during the first 4 h of the cultivation. Subsequently, the pH value fluctuates around a value of about 5.9 for 4 h. Afterwards, the online pH value slowly declines until the end of the cultivation. The time point, when the initial decline of the online pH value stops after 4 h, is associated with the DOT signal. At this time point, a small peak in the DOT signal is visible, indicating a switch in metabolic activity (see Fig. 3-7A).

The offline measured pH values follow the course of the online monitored pH value. Although both measures perfectly match at the beginning of the cultivation, a slight deviation becomes apparent throughout the later part of the cultivation. Thus, after 4 h, the offline measured pH value is consistently lower than the online monitored pH value, showing a deviation of about 0.4 units. This discrepancy can be traced back to the calibration of the pH sensor spot. Due to the highly laborious procedure for calibrating the pH sensor spot, in this experiment, only an offset calibration at the beginning of the cultivation was conducted. Thus, both pH values match at the beginning of the cultivation, when the pH value is close to its original value, but deviate from each other, when the pH value falls. Therefore, a three-point calibration prior to the experiment, to obtain a more accurate measurement, is highly recommended. Hence, when the pH value changes by 1 pH unit, a single offset calibration in combination with the manufacturer's pre-calibration is not sufficient.

In Fig. 3-7D, the online monitored shift of angle of bulk liquid θ-θ_0 is compared to the offline measured viscosity. During the first 6 h of the cultivation, no increase in the shift of angle of bulk liquid θ-θ_0 is visible. Afterwards, the measured value starts increasing linearly. When foaming occurs, a small jump of the shift of the angle of bulk liquid θ-θ_0 is visible. The online measured values closely correlate to the offline measured viscosity. In Fig. 3-7E, the phase number is depicted. The phase number indicates whether a system is in-phase or not. When the phase number falls below 1.26, a system is usually characterized as "out-of-phase", which means that the bulk liquid no longer follows the shaking movement of the shaking machine[4,5,83]. Effects of the out-of-phase phenomenon have been investigated in detail in chapter 2. The out-of-phase phenomenon is generally accompanied by a marked decrease in volumetric power input and oxygen transfer. For most of the fermentation time, the phase number is higher than 1.26. Only shortly before the system starts foaming, the phase number drops below 1.26, indicating that the cultivation broth gets out-of-phase. Hence, the out-of-phase phenomenon is most likely responsible for the foaming. Although the common understanding is that a non-baffled shake flask will never show foaming[88], the opposite could be shown with this cultivation. Presumably, a fraction of the liquid that is no longer in-phase acts as a kind of baffle, leading to foaming.

3.3.1 Online viscosity monitoring based on scattered light

In the previous cultivations of *E. coli* (see Fig. 3-5) and *P. polymyxa* (see Fig. 3-7), the triggering of the measurement and the determination of viscosity was performed by utilizing

the signal intensity of Oxnano nanoparticles. As discussed in the context of Fig. 3-5, the determination of viscosity requires tracking of the rotating bulk liquid. The necessary distinction between bulk liquid and liquid film can also be achieved based on the scattered light signal, which was already apparent in the non-triggered online monitoring of *E. coli* in Fig. 3-4B. In Fig. 3-4B, measurements in bulk and film led to distinctly different scattered light intensities. However, it can also be seen in Fig. 3-4B that a reliable distinction between bulk liquid and film can only be made, after sufficient biomass is formed. In the presented case, this relates to an optical density OD_{600} of roughly 3. Before this threshold of biomass is reached, the scattered light in the bulk liquid is lower or equal to the scattered light in the liquid film, making the distinction difficult, even impossible. It should be noted that at low biomass, a meaningful change in viscosity is unlikely anyway. Hence, the tracking of viscosity is probably not of high interest during the first phase of cultivation.

Fig. 3-8 depicts a cultivation of *Xanthomonas campestris*, where the distinction between bulk liquid and liquid film was not only based on the signal intensity of the Oxnano nanoparticles, but, additionally, on the scattered light signal. Therefore, the online monitored viscosity will be reported for both, the signal intensity of the Oxnano nanoparticles and the scattered light signal intensity. In this cultivation, the acceleration sensor was replaced by a Hall-effect sensor for the position signal. The Hall-effect sensor was previously used by Ladner et al.[66] as the reference signal in shake flask experiments and does not influence the performance of the presented online monitoring. *X. campestris* was cultivated due to its viscous product formation. The produced xanthan gum is a known, viscous, shear-thinning biopolymer[11,12]. A non-triggered cultivation of *X. campestris* is shown in the supplement in Appendix 43.

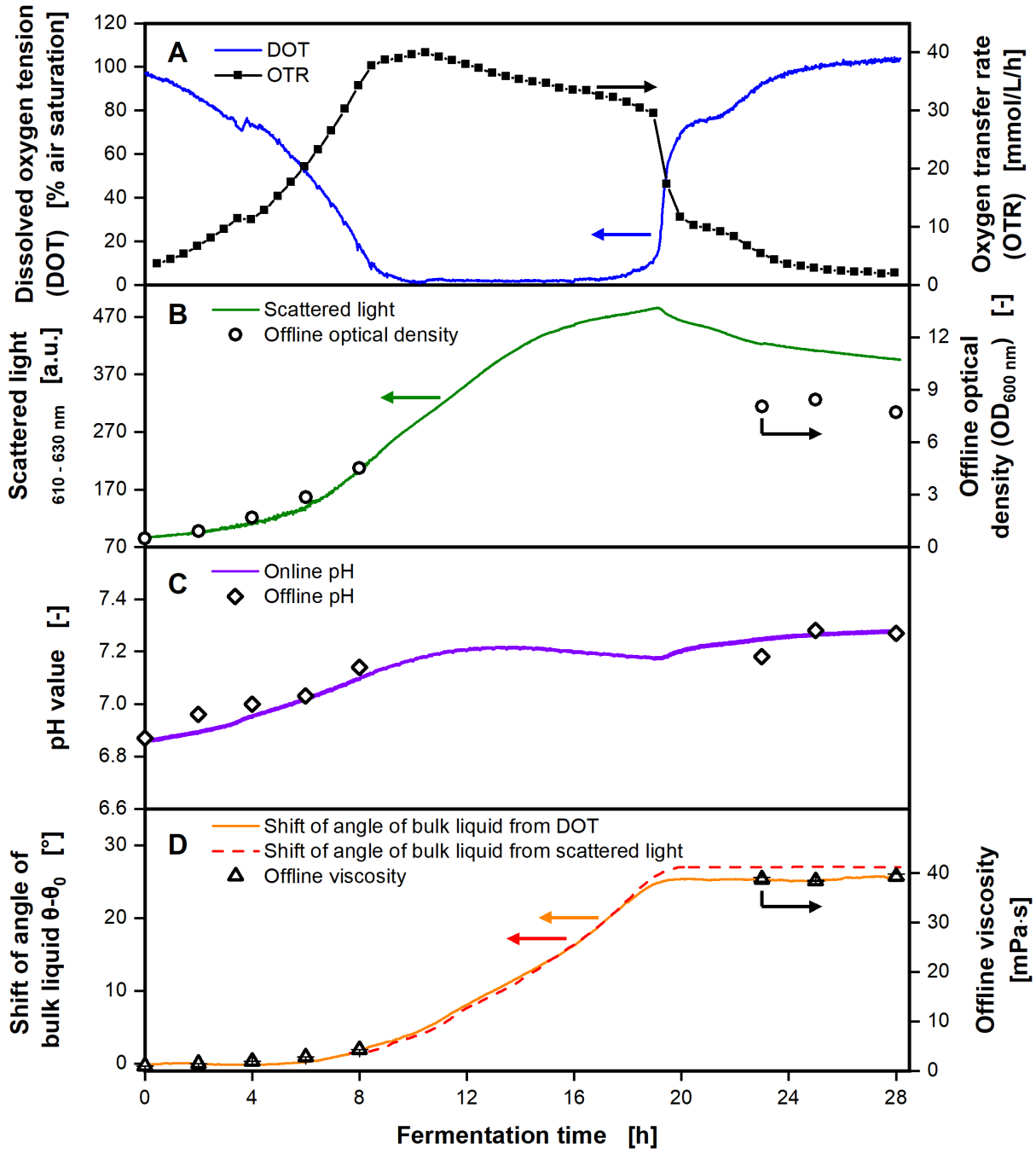

Fig. 3-8: Online monitoring of a *Xanthomonas campestris* cultivation with a triggered ShakeVisc device and a RAMOS device.

(A) Online monitoring of dissolved oxygen tension (DOT) and oxygen transfer rate (OTR), with Oxnano nanoparticles and a RAMOS device, respectively. The DOT was calibrated to 100 % in the inoculated medium prior to starting the monitoring. (B) Online monitoring of scattered light, compared to optical density measurements from offline samples at 600 nm. (C) Online monitoring of the pH value with pH sensitive spots, compared to pH measured from offline samples. The pH spot was calibrated at pH 2 and 11 before the cultivation. (D) Online monitoring of the shift of angle of bulk liquid θ-θ_0, compared to the offline viscosity, measured from offline samples with a rheometer. This shift was monitored via the signal intensity of Oxnano nanoparticles (see Fig. 3-3). In addition, the shift of angle of bulk liquid θ-θ_0 was also determined based on the scattered light signal. All offline samples were taken from shake flasks, cultivated in parallel. Triggering of the measurement of the bulk liquid was enabled by a hall effect sensor. Cultivation conditions: YM medium, 0.2 mg/mL Oxnano nanoparticles, range of pH spot = 6 – 8, initial pH = 6.9, initial OD_{600} = 0.5, shaking frequency (n) = 300 rpm, filling volume (V_L) = 20 mL, shaking

diameter (d_0) = 50 mm, temperature (T) = 30°C. Standard deviation is barely visible, as it is smaller than the data points. Offline optical density OD_{600} and offline pH were measured in single measurement.

Fig. 3-8A depicts the course of the OTR and triggered DOT measurements. The OTR increases exponentially to almost 40 mmol/L/h in the first 8.5 h. Merely, a small plateau of two measurement points at an OTR of 11 mmol/L/h after roughly 4 h, interrupting the exponential increase, can be seen. Similarly, the DOT exponentially decreases in the first 8.5 h from 95 % to nearly 0 % air saturation. Again, a small disturbance in the signal can be seen after 4 h. However, due to the higher measurement frequency of the DOT, the feature is well-defined as a small peak in the DOT. This peak is probably caused by the depletion of some component in the medium. After 8.5 h, an oxygen limitation can be seen in the DOT signal, lasting until about 18.5 h. In the same timeframe, the OTR shows a slightly slanted plateau, decreasing from 40 to 30 mmol/L/h. Such a slanted plateau is generally interpreted as the limitation by a substrate, which is not the main carbon source[90]. Only the online monitored DOT allows the clear identification of the oxygen limitation. Following this plateau, the OTR drops to roughly 10 mmol/L/h, remaining there for about 2 h, before declining to almost 0 mmol/L/h after 28 h. This feature is perfectly mirrored in the DOT signal with an intermittent DOT level of 75 % air saturation before reaching 100 % air saturation, indicating the end of cultivation. Furthermore, sharp, small dips can be seen in the DOT between 6 and 8 h. These dips perfectly coincide with the measurement points of the OTR and are caused by the measurement phases of the RAMOS device. During the measurement phase of the RAMOS device, the air in and outlet are sealed, turning the shake flask into a closed system. Throughout this phase, the oxygen partial pressure in the headspace decreases, therefore, decreasing the driving concentration gradient of oxygen from the gas to the liquid phase. Interestingly, the minute changes in the DOT are captured in the online monitored DOT signal. The described effect can also be seen, to some extent, in the triggered cultivation of *E. coli* in Fig. 3-5.

Fig. 3-8B shows the online monitored scattered light intensity and offline determined optical density. The scattered light exponentially increases from 85 to 240 a.u. during the exponential decline of the DOT in Fig. 3-8A, confirming the exponential growth. During the oxygen limitation, the scattered light increases further, at first linearly, then continuously slower, until reaching 485 a.u. at the end of the oxygen limitation after 18.5 h. Afterwards, the scattered light decreases to 400 a.u. at the end of cultivation. The scattered light declines faster during the DOT and OTR plateau between 20 and 24 h, than during the last 4 h of cultivation. As discussed previously, a decline in the scattered light at the end of cultivation might be explained by either

cell lysis or morphological changes. In this experiment no offline samples were drawn overnight. Optical densities determined during the first 8 h of cultivation correlate with the scattered light intensity. Determined optical densities from 21 h onwards, however, deviate from the scattered light. The scattered light would suggest optical densities of about 11, while optical densities of about 8 were determined offline. Due to the substantial viscosity of the culture broth at the end of cultivation, errors in the volumetric dilution of samples for the offline determination of optical density are very much possible. Notably, online monitored signals are impervious to such flaws in sample handling.

Fig. 3-8C shows the online-monitored and offline-determined pH. The online pH increases from about 6.9 at the start of the cultivation to 7.2 shortly after the oxygen limitation begins (see Fig. 3-8A). During the oxygen limitation, the pH stays nearly constant, slightly declining towards its end to 7.1. With the depletion of the main carbon source after 18.5 h, the pH increases again slightly up to almost 7.3 at the end of cultivation. The offline determined pH differs at most by 0.1 from the online monitored pH.

The online monitored shift of the angle of the bulk liquid θ-θ_0 and the offline determined viscosity are depicted in Fig. 3-8D. The shift of the angle of the bulk liquid θ-θ_0 is 0° for the first 5 h, then starts increasing and rises between 8 and 18.5 h to 25°. Following the depletion of the main carbon source after 18.5 h, the shift of the angle of the bulk liquid θ-θ_0 remains constant at 27° until the end of cultivation. As mentioned before, the shift of the angle of the bulk liquid θ-θ_0 was not only determined based on the signal intensity of the Oxnano nanoparticles (see Fig. 3-3), but also based on the scattered light intensity. The shift of the angle of the bulk liquid θ-θ_0 based on the scattered light intensity is only shown from 8 h onward, because the optical density before this time was too low to accurately discern between bulk liquid and liquid film. The shift of the angle of the bulk liquid θ-θ_0 of both systems aligns almost perfectly between 8 and 18 h. Small, non-relevant differences are observed in the plateau. It should be noted that the trigger position of DOT and scattered light measurements in the bulk liquid are directly dependent on the shift of the angle of the bulk liquid θ-θ_0 (see Fig. 3-3). Therefore, the trigger position can, in principle, also be derived from the scattered light signal intensity. Due to the similarity of the shift of the angle of the bulk liquid θ-θ_0 from Oxnano nanoparticles and scattered light, the trigger position would essentially be the same. Therefore, the triggered scattered light measurement of the bulk liquid can, in the future, be performed entirely independent of the Oxnano nanoparticles particles. The offline determined viscosity confirms the online monitored results. The offline viscosity is constant for the first 4 h and then

slowly increases to 4 mPa·s after 8 h. The offline sample after 23 h shows a viscosity of 40 mPa·s, which remains constant until the end of cultivation. The course of the viscosity also explains the slanted plateau in the OTR during the oxygen limitation in Fig. 3-8A. Giese et al.[23] uncovered how increases in viscosity up to 20 mPa·s, can increase the maximum oxygen transfer capacity in shake flasks. Yet, further elevation of the viscosity lowers the maximum oxygen transfer capacity[23]. In essence, the effect is caused by the modulation of the thickness of liquid films in shake flasks and the oxygen diffusion by the viscosity.

3.4 Conclusion

The ShakeVisc system provides an unprecedented number of online monitoring signals for cultivations in shake flasks. It provides accurate measurements of the scattered light as an indicator for biomass, the DOT, pH value and the shift of angle of bulk liquid θ-θ_0, as a measure of the change of the viscosity during cultivation. For monitoring the DOT, fluorescent oxygen sensitive Oxnano nanoparticles were used instead of DOT spots. This leads to accurate measurements at low DOT levels and allows for tracking of the rotating bulk liquid via the fluorescent signal intensity.

In this study, the ShakeVisc system was tested with cultivations of *E. coli*, *P. polymyxa* and *X. campestris*. The importance of tracking of the rotating bulk liquid was demonstrated with cultivations of *E. coli*. Non-triggered measurements of DOT and scattered light generate data noise, from which the measurement points originating from the rotating bulk liquid can be derived. By triggering, however, DOT and scattered light measurements are only carried out in the rotating bulk liquid. This leads to distinct well-defined DOT and scattered light signals and prevents the generation of mixed signals. The tracking of the rotating bulk liquid also allows for measurement of the shift of angle of the bulk liquid θ-θ_0, which correlates to the viscosity of the cultivation broth. The ShakeVisc system operates at measurement frequencies of roughly 0.1 Hz. This is a vast improvement to offline sampling, but even a significant improvement over the quasi-continuous operation of the RAMOS device. Thus, in the cultivation of *E. coli*, the DOT revealed a second phase of oxygen limitation, which might be missed with the RAMOS device. The measurement frequency and sensitivity of the DOT is even high enough to capture the small impact of the RAMOS measuring phases on the DOT. This effect could be observed for the *X. campestris* cultivation and to some extent in the cultivations of *E. coli*.

For scattered light measurements with the BioLector system in microtiter plates, the wavelength of 620 nm is well established[124]. At this wavelength influences of color changes of the medium are reduced[113]. Therefore, the newly developed scattered light sensor of the ShakeVisc module operates at 620 nm. The scattered light signals precisely correlate with offline optical density measurements, even at elevated viscosities.

The pH value, online measured via pH sensor spots, matches offline measured pH values. Provided by the higher time resolution of the online measurement compared to offline measurements, changes in the course of pH are made visible that would otherwise have

remained hidden. Online and offline measured pH values differ less than 0.4 pH units. Deviations are most likely based on changes in medium composition during cultivation.

In the cultivation of *P. polymyxa*, a cultivation at elevated viscosities of up to 150 mPa·s, the shift of angle of bulk liquid θ-θ_0 correlated precisely with the offline measured viscosity. Foaming, observed at the end of cultivation, is captured as a sudden increase in the scattered light intensity. In combination with the viscosity data, the foaming could be linked to the onset of the out-of-phase phenomenon, due to the high viscosity.

During the cultivations of *E. coli* and *P. polymyxa*, the tracking of the bulk liquid and, hence, triggering and determination of the shift of angle of bulk liquid θ-θ_0 was performed solely based on the Oxnano nanoparticle signal intensity. In the cultivation of *X. campestris*, the option for triggering the measurement was extended by tracking the bulk liquid and determining the shift of angle of bulk liquid θ-θ_0, based additionally on the scattered light intensity. The resulting viscosity monitoring is essentially the same for both approaches. Therefore, Oxnano nanoparticles are, in the future, only necessary, when monitoring of the DOT is desired, but are not required for the monitoring of scattered light and of viscosity changes.

Chapter 4

4 Summary and Outlook

The first goal of this thesis was to establish and verify a CFD model for shake flasks, aimed at simulating fluid flow and predicting volumetric power input, k_La and shear rates. Special interest was given to simulating elevated viscosity, as is usually encountered in cultivations involving biopolymers or fungi, exhibiting disperse growth.

Simulated fluid flows were compared to experimentally determined freeze frames of fluid flow, recorded and kindly provided by Azizan et al.[5,6]. Across all simulated filling volumes, shaking frequencies and viscosities the CFD model closely matched the experimental data in terms of fluid shape and position. Simulations also matched the measurements for liquid film thickness of Hermann[82] at elevated viscosity. The thus verified velocity fields of the CFD simulations were used to calculate volumetric power inputs based on the energy dissipation rate. Resulting volumetric power inputs were compared to experimental values from Büchs et al. and their correlation for volumetric power inputs in shake flasks[3,4]. The average deviation between volumetric power input from CFD simulation and experiment is just 0.18 kW/m^3. This holds true even at small phase numbers, where the volumetric power input correlation by Büchs et al.[3,4] overpredicts volumetric power input. Hence, volumetric power inputs from the CFD simulations were used to modify and improve the correlation for volumetric power as function of the phase number. Furthermore, the k_La was calculated from the CFD simulations to investigate the effects of operating conditions and viscosity on oxygen transfer in shake flask. Results from the CFD simulations were compared to the k_La correlation by Henzler and

Schedel[28]. k_La values form the CFD deviate by less than a factor of two from the k_La correlation by Henzler and Schedel. Notably, the k_La spans almost three orders of magnitude for the investigated operating conditions. Lastly, the shear rate was derived from the CFD simulations. Here, two different ways to calculate the shear rate from the velocity field of CFD simulations were investigated. Firstly, the shear rate was taken as the scalar measure of the strain rate tensor and, secondly, as a function of the largest eigenvalue of the strain rate tensor. Resulting shear rates were compared to the correlation for effective shear rates in shake flasks by Giese et al.[7]. The first approach to calculate the shear rate results in shear rates three to six times smaller than indicated by the correlation by Giese et al.[7]. Fortunately, the second approach resulted in much smaller deviations. At waterlike viscosity shear rates from the CFD were less than three times smaller. At elevated viscosity of above 1 mPa·s the results were on average just 16 % smaller than indicated by the correlation for effective shear rates by Giese et al.[7]. Importantly, the CFD simulations, especially the calculated volumetric power inputs, highlight the inherently gradual transition from in-phase to out-of-phase operating conditions.

CFD simulations offer exciting possibilities in further deepening process understanding and enabling careful planning of experiments in the out-of-phase regime. Continued work in the determination of shear rate is of special interest. CFD simulations presented in this thesis were performed under the assumption of purely Newtonian behavior. However, biopolymers and disperse growing fungi notoriously exhibit non-Newtonian, shear-thinning behavior. Hence, CFD simulations require an accurate approach to calculate shear rates. Furthermore, a recent study by Neuss et al.[125] highlighted the importance of the energy dissipation rate in cell culture. They showed a 40 % reduction of antibody titers for an increase of the average energy dissipation rate from 0.12 W/kg to 3.84 W/kg.

The second part of this thesis was the combination of online monitoring of DOT, biomass, pH and viscosity in a single system called ShakeVisc. The DOT was measured with oxygen sensitive Oxnano nanoparticles, biomass with a newly developed scattered light sensor, pH with pH sensor spots and viscosity as the shift of the angle of the bulk liquid, i.e., the gradual transition from in-phase to out-of-phase operating conditions. Importantly, the DOT and scattered light measurement were triggered according to the shift of the angle of the bulk liquid to ensure measurements within the rotating liquid phase. Additionally, the OTR in shake flasks was measured in parallel with a RAMOS.

The ShakeVisc system operates at a sampling frequency of 0.1 Hz. This is a significant improvement over the semi-continuous operating mode of the RAMOS. The online monitored

DOT clearly revealed a second oxygen limitation in *E. coli* cultivations, which would have been missed in the OTR recorded by the RAMOS. Uncovering this second oxygen limitation allowed for offline sampling precisely during this time, revealing the consumption of glycerol. The consumed glycerol must have been carried over from the cryogenic culture. The scattered light sensor was designed to operate at roughly 620 nm, a wavelength well established in the BioLector system for microtiter plates. Recorded scattered light signals correlated well with the offline determined optical density measurements over the entire cultivation, even under increasing viscosity. Similarly, the pH closely followed the offline determined pH value, deviating less than 0.4 pH units. Online monitoring of the pH, however, provided a vast improvement in sampling frequency. Lastly, the shift of the angle of bulk liquid is closely correlated with offline determined viscosity. It was shown, that the shift of angle of bulk liquid can be determined based on added Oxnano nanoparticles, but also based solely on the recorded scattered light signal.

In the future, attention should be given to the calibration the shift of angle of bulk liquid to the viscosity. This can be done by performing laborious experiments as shown by Sieben et al.[64]. It should, however, also become possible to skip the required experiments in the lab. CFD simulations were proven to accurately predict shape and position of the rotating bulk liquid. Therefore, it should be possible to derive the necessary shift of angle of bulk liquid entirely from CFD simulations.

5 Bibliography

1. Maier, U. & Büchs, J. Characterisation of the gas-liquid mass transfer in shaking bioreactors. *Biochem Eng J* **7**, 99–106 (2001).

2. Maier, U., Losen, M. & Büchs, J. Advances in understanding and modeling the gas–liquid mass transfer in shake flasks. *Biochem Eng J* **17**, 155–167 (2004).

3. Büchs, J., Maier, U., Milbradt, C. & Zoels, B. Power consumption in shaking flasks on rotary shaking machines: I. Power consumption measurement in unbaffled flasks at low liquid viscosity. *Biotechnol Bioeng* **68**, 589–593 (2000).

4. Büchs, J., Maier, U., Milbradt, C. & Zoels, B. Power consumption in shaking flasks on rotary shaking machines: II. Nondimensional description of specific power consumption and flow regimes in unbaffled flasks at elevated liquid viscosity. *Biotechnol Bioeng* **68**, 594–601 (2000).

5. Azizan, A., Sieben, M., Wandrey, G. & Büchs, J. Reassessing the out-of-phase phenomenon in shake flasks by evaluating the angle-dependent liquid distribution relative to the direction of the centrifugal acceleration. *Biotechnol Bioeng* **116**, 2983–2995 (2019).

6. Azizan, A. & Büchs, J. Three-dimensional (3D) evaluation of liquid distribution in shake flask using an optical fluorescence technique. *J Biol Eng* **11**, 28 (2017).

7. Giese, H. *et al.* Effective shear rates in shake flasks. *Chem Eng Sci* **118**, 102–113 (2014).

8. Serra, M., Casas, A., Toubarro, D., Barros, A. N. & Teixeira, J. A. Microbial hyaluronic acid production: a review. *Molecules* **28**, 2084 (2023).

9. Seviour, R. J., McNeil, B., Fazenda, M. L. & Harvey, L. M. Operating bioreactors for microbial exopolysaccharide production. *Crit Rev Biotechnol* **31**, 170–185 (2011).

10. Sparviero, S. *et al.* Yeast extracts from different manufacturers and supplementation of amino acids and micro elements reveal a remarkable impact on alginate production by *A. vinelandii* ATCC9046. *Microb Cell Fact* **22**, 99 (2023).

11. García-Ochoa, F., Santos, V. E., Casas, J. A. & Gómez, E. Xanthan gum: production, recovery, and properties. *Biotechnol Adv* **18**, 549–579 (2000).

12. Palaniraj, A. & Jayaraman, V. Production, recovery and applications of xanthan gum by *Xanthomonas campestris*. *J Food Eng* **106**, 1–12 (2011).

13. Gorin, P. A. J. & Spencer, J. F. T. Exocellular alginic acid from *Azotobacter vinelandii*. *Can J Chem* **44**, 993–998 (1966).

14. Peña C, Galindo, E. & Büchs, J. The viscosifying power, degree of acetylation and molecular mass of the alginate produced by *Azotobacter vinelandii* in shake flasks are determined by the oxygen transfer rate. *Process Biochem* **46**, 290–297 (2011).

15. Füting, P., Barthel, L., Cairns, T. C., Briesen, H. & Schmideder, S. Filamentous fungal applications in biotechnology: a combined bibliometric and patentometric assessment. *Fungal Biol Biotechnol* **8**, 23 (2021).

16. Schuster, E., Dunn-Coleman, N., Frisvad, J. C. & Van Dijck, P. W. M. On the safety of *Aspergillus niger* - a review. *Appl Microbiol Biotechnol* **59**, 426–35 (2002).

17. Weber, S. S., Bovenberg, R. A. L. & Driessen, A. J. M. Biosynthetic concepts for the production of β-lactam antibiotics in *Penicillium chrysogenum*. *Biotechnol J* **7**, 225–36 (2012).

18. Behera, B. C. Citric acid from *Aspergillus niger*: a comprehensive overview. *Crit Rev Microbiol* **46**, 727–749 (2020).

19. Wucherpfennig, T., Kiep, K. A., Driouch, H., Wittmann, C. & Krull, R. Morphology and rheology in filamentous cultivations. *Adv Appl Microbiol* **72**, 89–136 (2010).

20. Peter, C. P., Lotter, S., Maier, U. & Büchs, J. Impact of out-of-phase conditions on screening results in shaking flask experiments. *Biochem Eng J* **17**, 205–215 (2004).

21. Kawase, Y. & Moo-young, M. Mass transfer at a free surface in stirred tank bioreactors. *Chemical Engineering Research & Design* **68**, 189–194 (1990).

22. Gnielinski, V. *Berechnung mittlerer Wärme- und Stoffübergangskoeffizienten an laminar und turbulent überströmten Einzelkörpern mit Hilfe einer einheitlichen Gleichung* [Calculation of mean heat and mass transfer coefficients on laminar and turbulent overflown bodies with a unified equation]. *Forsch Ingenieurwes* **41**, 145–153 (1975).

23. Giese, H. *et al.* Liquid films on shake flask walls explain increasing maximum oxygen transfer capacities with elevating viscosity. *Biotechnol Bioeng* **111**, 295–308 (2014).

24. Van Suijdam, J. C., Kossen, N. W. F. & Joha, A. C. Model for oxygen transfer in a shake flask. *Biotechnol Bioeng* **20**, 1695–1709 (1978).

25. Veglio, F., Beolchini, F. & Ubaldini, S. Empirical models for oxygen mass transfer: a comparison between shake flask and lab-scale fermentor and application to manganiferous ore bioleaching. *Process Biochem* **33**, 367–376 (1998).

26. Nikakhtari, H. & Hill, G. A. Modelling oxygen transfer and aerobic growth in shake flasks and well-mixed bioreactors. *Can J Chem Eng* **83**, 493–499 (2008).

27. Veljković, V., Nikolić, S., Lazic, M. & Engler, C. R. Oxygen transfer in flasks shaken on orbital shakers. *Hem Ind* **49**, 265–272 (1995).

28. Henzler, H.-J. & Schedel, M. Suitability of the shaking flask for oxygen supply to microbiological cultures. *Bioprocess Eng* **7**, 123–131 (1991).

29. Santos-Moreau, V., Lopes, J. C. B. & Fonte, C. P. Estimation of k_La values in bench-scale stirred tank reactors with self-inducing impeller by multiphase CFD simulations. *Chem Eng Technol* **42**, 1545–1554 (2019).

30. Wutz, J. *et al.* Predictability of k_La in stirred tank reactors under multiple operating conditions using an Euler–Lagrange approach. *Eng Life Sci* **16**, 633–642 (2016).

31. Hofmann, S. *et al.* Lagrangian sensors in a stirred tank reactor: Comparing trajectories from 4D-Particle Tracking Velocimetry and Lattice-Boltzmann simulations. *Chem Eng J* **449**, 137549 (2022).

32. Weiland, C. *et al.* Computational study of three-dimensional Lagrangian transport and mixing in a stirred tank reactor. *Chem Eng J Adv* **14**, 100448 (2023).

33. Fitschen, J. *et al.* Novel evaluation method to determine the local mixing time distribution in stirred tank reactors. *Chem Eng Sci* **10**, 100098 (2021).

34. Kuschel, M. & Takors, R. Simulated oxygen and glucose gradients as a prerequisite for predicting industrial scale performance a priori. *Biotechnol Bioeng* **117**, 2760–2770 (2020).

35. Azargoshasb, H., Mousavi, S. M., Jamialahmadi, O., Shojaosadati, S. A. & Mousavi, S. B. Experiments and a three-phase computational fluid dynamics (CFD) simulation coupled with population balance equations of a stirred tank bioreactor for high cell density cultivation. *Can J Chem Eng* **94**, 20–32 (2016).

36. Gimbun, J., Rielly, C. D. & Nagy, Z. K. Modelling of mass transfer in gas–liquid stirred tanks agitated by Rushton turbine and CD-6 impeller: A scale-up study. *Chem Eng Res Des* **87**, 437–451 (2009).

37. Montante, G., Moštěk, M., Jahoda, M. & Magelli, F. CFD simulations and experimental validation of homogenisation curves and mixing time in stirred Newtonian and pseudoplastic liquids. *Chem Eng Sci* **60**, 2427–2437 (2005).

38. Morchain, J., Gabelle, J. C. & Cockx, A. A coupled population balance model and CFD approach for the simulation of mixing issues in lab-scale and industrial bioreactors. *AIChE Journal* **60**, 27–40 (2014).

39. Liu, Y. *et al.* Quantitative evaluation of the shear threshold on *Carthamus tinctorius L.* cell growth with computational fluid dynamics in shaken flask bioreactors. *Biochem Eng J* **113**, 66–76 (2016).

40. Li, C. *et al.* CFD analysis of the turbulent flow in baffled shake flasks. *Biochem Eng J* **70**, 140–150 (2013).

41. Zhang, H., Williams-Dalson, W., Keshavarz-Moore, E. & Shamlou, P. A. Computational-fluid-dynamics (CFD) analysis of mixing and gas–liquid mass transfer in shake flasks. *Biotechnol Appl Biochem* **41**, 1–8 (2005).

42. Mehmood, N., Olmos, E., Marchal, P., Goergen, J.-L. & Delaunay, S. Relation between pristinamycins production by *Streptomyces pristinaespiralis*, power dissipation and volumetric gas–liquid mass transfer coefficient, k_La. *Process Biochemistry* **45**, 1779–1786 (2010).

43. Li, X., Scott, K., Kelly, W. J. & Huang, Z. Development of a Computational Fluid Dynamics Model for Scaling-up Ambr Bioreactors. *Biotechnol Bioprocess Eng* **23**, 710–725 (2018).

44. Lu, Z., Li, C., Fei, L., Zhang, H. & Pan, Y. Effect of baffle structure on flow field characteristics of orbitally shaken bioreactor. *Bioprocess Biosyst Eng* **44**, 563–573 (2021).

45. Zhang, H., Lamping, S. R., Pickering, S. C. R., Lye, G. J. & Shamlou, P. A. Engineering characterisation of a single well from 24-well and 96-well microtitre plates. *Biochem Eng J* **40**, 138–149 (2008).

46. Wutz, J., Steiner, R., Assfalg, K. & Wucherpfennig, T. Establishment of a CFD-based kLa model in microtiter plates to support CHO cell culture scale-up during clone selection. *Biotechnol Prog* **34**, 1120–1128 (2018).

47. Montes-Serrano, I., Satzer, P., Jungbauer, A. & Dürauer, A. Characterization of hydrodynamics and volumetric power input in microtiter plates for the scale-up of downstream operations. *Biotechnol Bioeng* **119**, 523–534 (2022).

48. He, S. *et al.* Development of a novel microplate for high-throughput screening and optimization of DHA producing strains based on CFD technology. *Biotechnol J* (2023) doi:10.1002/biot.202300169.

49. Discacciati, M. *et al.* Numerical simulation of orbitally shaken viscous fluids with free surface. *Int J Numer Methods Fluids* **71**, 294–315 (2013).

50. Hansen, S. *et al.* Implementation of perforated concentric ring walls considerably improves gas-liquid mass transfer of shaken bioreactors. *Front Bioeng Biotechnol* **10**, 720 (2022).

51. Zhu, L., Chen, W. & Zhao, C. Analysis of hollow wall effect on the fluid dynamics in the orbitally shaken bioreactors. *Sci Rep* **12**, (2022).

52. Alberini, F., Liu, L., Stitt, E. H. & Simmons, M. J. H. Comparison between 3-D-PTV and 2-D-PIV for determination of hydrodynamics of complex fluids in a stirred vessel. *Chem Eng Sci* **171**, 189–203 (2017).

53. Gabriele, A., Tsoligkas, A. N., Kings, I. N. & Simmons, M. J. H. Use of PIV to measure turbulence modulation in a high throughput stirred vessel with the addition of high Stokes number particles for both up- and down-pumping configurations. *Chem Eng Sci* **66**, 5862–5874 (2011).

54. Escudié, R. & Liné, A. Experimental analysis of hydrodynamics in a radially agitated tank. *AIChE Journal* **49**, 585–603 (2003).

55. Romano, M. G., Alberini, F., Liu, L., Simmons, M. J. H. & Stitt, E. H. 3D-PTV flow measurements of Newtonian and non-Newtonian fluid blending in a batch reactor in the transitional regime. *Chem Eng Sci* **246**, 116969 (2021).

56. Cheng, Y. & Diez, F. J. A 4D imaging tool for Lagrangian particle tracking in stirred tanks. *AIChE Journal* **57**, 1983–1996 (2011).

57. Thomas, J. M. D., Chakraborty, A., Berson, R. E., Shakeri, M. & Sharp, M. K. Validation of a CFD model of an orbiting culture dish with PIV and analytical solutions. *AIChE Journal* **63**, 4233–4242 (2017).

58. Weheliye, W., Yianneskis, M. & Ducci, A. On the fluid dynamics of shaken bioreactors-flow characterization and transition. *AIChE Journal* **59**, 334–344 (2013).

59. Palacios-Morales, C. *et al.* The flow inside shaking flasks and its implication for mycelial cultures. *Chem Eng Sci* **152**, 163–171 (2016).

60. Zhu, L. *et al.* Fluid dynamics of flow fields in a disposable 600-mL orbitally shaken bioreactor. *Biochem Eng J* **129**, 84–95 (2018).

61. Zhu, L. *et al.* Fluid dynamics of a pilot-scale OrbShake bioreactor under different operating conditions. *J Chem Technol Biot* **97**, 1027–1036 (2022).

62. Seletzky, J. *et al.* A simple and inexpensive method for investigating microbiological, enzymatic, or inorganic catalysis using standard histology and microbiology laboratory equipment: assembly, mass transfer properties, hydrodynamic conditions and evaluation. *Biotech Histochem* **81**, 133–138 (2006).

63. Tan, R.-K., Eberhard, W. & Büchs, J. Measurement and characterization of mixing time in shake flasks. *Chem Eng Sci* **66**, 440–447 (2011).

64. Sieben, M., Hanke, R. & Büchs, J. Contact-free determination of viscosity in multiple parallel samples. *Sci Rep* **9**, 8335 (2019).

65. Ottow, W., Kuemmel, A. & Büchs, J. Shaking flask: flow simulation and validation. in *Conference on Transport Phenomena with Moving Boundaries* 270–279 (VDI Fortschrittsberichte, Berlin, 2004).

66. Ladner, T., Flitsch, D., Lukacs, M., Sieben, M. & Büchs, J. Combined dissolved oxygen tension and online viscosity measurements in shake flask cultivations via infrared fluorescent oxygen-sensitive nanoparticles. *Biotechnol Bioeng* **116**, 3215–3227 (2019).

67. Hoffmann, K. *et al.* Online measurement of the viscosity in shake flasks enables monitoring of γ-PGA production in depolymerase knockout mutants of *Bacillus subtilis* with the phosphate-starvation inducible promoter P_{pst}. *Biotechnol Prog* **39**, (2023).

68. OpenFOAM Foundation. https://openfoam.org/.

69. Heyns, J. A. & Oxtoby, O. F. Modelling surface tension dominated multiphase flows using the VOF approach. in *In 6th European Conference on Computational Fluid Dynamics* (Barcelona, Spain, 2014).

70. Brackbill, J. U., Kothe, D. B. & Zemach, C. A continuum method for modeling surface tension. *J Comput Phys* **100**, 335–354 (1992).

71. Peter, C. P., Suzuki, Y. & Büchs, J. Hydromechanical stress in shake flasks: Correlation for the maximum local energy dissipation rate. *Biotechnol Bioeng* **93**, 1164–1176 (2006).

72. Menter, F. R., Kuntz, M. & Langtry, R. Ten years of industrial experience with the SST turbulence model. *4th International Symposium on Turbulence, Heat and Mass Transfer* 625–632 (2003).

73. Verein deutscher Ingenieure. *VDI-Wärmeatlas*. *Springer* (Springer Vieweg Verlag, Berlin, Heidelberg, 2013).

74. Büchs, J., Maier, U., Lotter, S. & Peter, C. P. Calculating liquid distribution in shake flasks on rotary shakers at waterlike viscosities. *Biochem Eng J* **34**, 200–208 (2007).

75. Greenshields, C. *OpenFOAM v9 User Guide*. (The OpenFOAM Foundation, London, 2021).

76. Evans, R., Dal Poggetto, G., Nilsson, M. & Morris, G. A. Improving the interpretation of small molecule diffusion coefficients. *Anal Chem* **90**, 3987–3994 (2018).

77. Lamont, J. C. & Scott, D. S. An eddy cell model of mass transfer into the surface of a turbulent liquid. *AIChE Journal* **16**, 513–519 (1970).

78. Soh, G. Y., Yeoh, G. H. & Timchenko, V. An algorithm to calculate interfacial area for multiphase mass transfer through the volume-of-fluid method. *Int J Heat Mass Transf* **100**, 573–581 (2016).

79. OpenFOAM v9 github. https://github.com/OpenFOAM/OpenFOAM-9.

80. Soos, M., Ehrl, L., Bäbler, M. U. & Morbidelli, M. Aggregate breakup in a contracting nozzle. *Langmuir* **26**, 10–18 (2010).

81. Gaden, E. L. Improved shaken flask performance. *Biotechnol Bioeng* **4**, 99–103 (1962).

82. Hermann, R. Entwicklung Und Anwendung Optischer Methoden Zur Charakterisierung von Kleinkulturbioreaktoren *[Development and Application of Optical Methods for the Characterization of Small Scale Bioreactors]*. (Shaker Verlag, Aachen, 2002).

83. Büchs, J., Lotter, S. & Milbradt, C. Out-of-phase operating conditions, a hitherto unknown phenomenon in shaking bioreactors. *Biochem Eng J* **7**, 135–141 (2001).

84. Meier, K. *et al.* Correlation for the maximum oxygen transfer capacity in shake flasks for a wide range of operating conditions and for different culture media. *Biochem Eng J* **109**, 228–235 (2016).

85. Calderbank, P. H. & Moo-Young, M. B. The continuous phase heat and mass-transfer properties of dispersions. *Chem Eng Sci* **16**, 39–54 (1961).

86. Fortescue, G. E. & Pearson, J. R. A. On gas absorption into a turbulent liquid. *Chem Eng Sci* **22**, 1163–1176 (1967).

87. Klöckner, W. & Büchs, J. Advances in shaking technologies. *Trends Biotechnol* **30**, 307–314 (2012).

88. Büchs, J. Introduction to advantages and problems of shaken cultures. *Biochem Eng J* **7**, 91–98 (2001).

89. Dinger, R. *et al.* Device for respiration activity measurement enables the determination of oxygen transfer rates of microbial cultures in shaken 96-deepwell microtiter plates. *Biotechnol Bioeng* **119**, 881–894 (2022).

90. Anderlei, T. & Büchs, J. Device for sterile online measurement of the oxygen transfer rate in shaking flasks. *Biochem Eng J* **7**, 157–162 (2001).

91. Flitsch, D. *et al.* Respiration activity monitoring system for any individual well of a 48-well microtiter plate. *J Biol Eng* **10**, 1–14 (2016).

92. Scheidle, M., Klinger, J. & Büchs, J. Combination of On-line pH and Oxygen Transfer Rate Measurement in Shake Flasks by Fiber Optical Technique and Respiration Activity MOnitoring System (RAMOS). *Sensors 2007, Vol. 7, Pages 3472-3480* **7**, 3472–3480 (2007).

93. Gupta, A. & Rao, G. A study of oxygen transfer in shake flasks using a non-invasive oxygen sensor. *Biotechnol Bioeng* **84**, 351–358 (2003).

94. Tolosa, L., Kostov, Y., Harms, P. & Rao, G. Noninvasive measurement of dissolved oxygen in shake flasks. *Biotechnol Bioeng* **80**, 594–597 (2002).

95. Shanmugam, M. K., Sriman, S. & Gummadi, S. N. Online measurement of dissolved oxygen in shake flask to elucidate its role on caffeine degradation by *Pseudomonas sp. Indian Chemical Engineer* **64**, 162–170 (2022).

96. Ries, C., John, G., John, C., Eibl, R. & Eibl, D. A shaken disposable bioreactor system for controlled insect cell cultivations at milliliter-scale. *Eng Life Sci* **10**, 75–79 (2010).

97. Schneider, K., Schütz, V., John, G. T. & Heinzle, E. Optical device for parallel online measurement of dissolved oxygen and pH in shake flask cultures. *Bioprocess Biosyst Eng* **33**, 541–547 (2010).

98. Hansen, S., Kensy, F., Käser, A. & Büchs, J. Potential errors in conventional DOT measurement techniques in shake flasks and verification using a rotating flexitube optical sensor. *BMC Biotechnol* **11**, (2011).

99. Flitsch, D., Ladner, T., Lukacs, M. & Büchs, J. Easy to use and reliable technique for online dissolved oxygen tension measurement in shake flasks using infrared fluorescent oxygen-sensitive nanoparticles. *Microb Cell Fact* **15**, 1–11 (2016).

100. Borisov, S. M. & Klimant, I. Luminescent nanobeads for optical sensing and imaging of dissolved oxygen. *Microchimica Acta* **164**, 7–15 (2009).

101. Bruder, S., Reifenrath, M., Thomik, T., Boles, E. & Herzog, K. Parallelised online biomass monitoring in shake flasks enables efficient strain and carbon source dependent growth characterisation of *Saccharomyces cerevisiae*. *Microb Cell Fact* **15**, 127 (2016).

102. Bauer, I., Abt, B., Yap, A., Leuchtle, B. & Haas, H. Online Biomass Monitoring Enables Characterization of the Growth Pattern of *Aspergillus fumigatus* in Liquid Shake Conditions. *Journal of Fungi* **8**, 1013 (2022).

103. Ude, C. *et al.* Application of an Online-Biomass Sensor in an Optical Multisensory Platform Prototype for Growth Monitoring of Biotechnical Relevant Microorganism and Cell Lines in Single-Use Shake Flasks. *Sensors 2014, Vol. 14, Pages 17390-17405* **14**, 17390–17405 (2014).

104. Maschke, R. W., John, G. T. & Eibl, D. Monitoring of Oxygen, pH, CO2, and Biomass in Smart Single-Use Shake Flasks. *Chemie Ingenieur Technik* **94**, 1995–2001 (2022).

105. Ebert, F. V., Reitz, C., Cruz-Bournazou, M. N. & Neubauer, P. Characterization of a noninvasive on-line turbidity sensor in shake flasks for biomass measurements. *Biochem Eng J* **132**, 20–28 (2018).

106. Schmidt-Hager, J. *et al.* Noninvasive online biomass detector system for cultivation in shake flasks. *Eng Life Sci* **14**, 467–476 (2014).

107. Mao, J. *et al.* A noninvasive online system for biomass monitoring in shaker flasks using backward scattered light. *Biotechnology and Bioprocess Engineering* **22**, 161–169 (2017).

108. sbi Scientific Bioprocessing Cell Growth Quantifier (CGQ). https://www.scientificbio.com/cgq/.

109. PreSens Precision Sensing GmbH SFR Shake Flask Reader. https://www.presens.de/products/detail/sfr-shake-flask-reader.

110. Pretzner, B. *et al.* Predictive monitoring of shake flask cultures with online estimated growth models. *Bioengineering* **8**, 177 (2021).

111. PyroScience GmbH, PyroScience homepage.

112. sbi Scientific Bioprocessing Cell Growth Quantifier (CGQ) technical specifications.

113. Shuler, M. L. ; K. F. *Bioprocess Engineering Basic Concepts*. (Prentice Hall Inc., 2002).

114. Carignatto, C. R. R., Oliveira, K. S. M., de Lima, V. M. G. & de Neto, P. O. New Culture Medium to Xanthan Production by *Xanthomonas campestris pv. campestris*. *Indian J Microbiol* **51**, 283–288 (2011).

115. Peña, C., Campos, N. & Galindo, E. Changes in alginate molecwlar mass distributions, broth viscosity and morphology of *Azotobacter vinelandii* cultured in shake flasks. *Appl Microbiol Biotechnol* **48**, 510–515 (1997).

116. Ndao, A., Sellamuthu, B., Kumar, L. R., Tyagi, R. D. & Valéro, J. R. Biopesticide production using *Bacillus thuringiensis kurstaki* by valorization of starch industry wastewater and effluent from aerobic, anaerobic digestion. *Systems Microbiology and Biomanufacturing* **1**, 494–504 (2021).

117. Wucherpfennig, T., Lakowitz, A. & Krull, R. Comprehension of viscous morphology-Evaluation of fractal and conventional parameters for rheological characterization of *Aspergillus niger* culture broth. *J Biotechnol* **163**, 124–132 (2013).

118. Bliatsiou, C. *et al.* Rheological characteristics of filamentous cultivation broths and suitable model fluids. *Biochem Eng J* **163**, 107746 (2020).

119. Sieben, M. M. Characterization of the Permeability of Sealing Tapes and Development of a Viscosity Measuring Technique in Shaken Reactors. (RWTH Aachen University, 2017).

120. Borisov, S. M., Zenkl, G. & Klimant, I. Phosphorescent platinum(II) and palladium(II) complexes with azatetrabenzoporphyrinss new-red laser diode-compatible indicators for optical oxygen sensing. *ACS Appl Mater Interfaces* **2**, 366–374 (2010).

121. Anderlei, T., Zang, W., Papaspyrou, M. & Büchs, J. Online respiration activity measurement (OTR, CTR, RQ) in shake flasks. *Biochem Eng J* **17**, 187–194 (2004).

122. Hansen, S., Hariskos, I., Luchterhand, B. & Büchs, J. Development of a modified Respiration Activity Monitoring System for accurate and highly resolved measurement of respiration activity in shake flask fermentations. *J Biol Eng* **6**, 1–12 (2012).

123. Phue, J. N. & Shiloach, J. Impact of dissolved oxygen concentration on acetate accumulation and physiology of *E. coli* BL21, evaluating transcription levels of key genes at different dissolved oxygen conditions. *Metab Eng* **7**, 353–363 (2005).

124. Kensy, F., Zang, E., Faulhammer, C., Tan, R. K. & Büchs, J. Validation of a high-throughput fermentation system based on online monitoring of biomass and fluorescence in continuously shaken microtiter plates. *Microb Cell Fact* **8**, 1–17 (2009).

125. Neuss, A., Tomas Borges, J. S., von Vegesack, N., Büchs, J. & Magnus, J. B. Impact of hydromechanical stress on CHO cells' metabolism and productivity: Insights from shake flask cultivations with online monitoring of the respiration activity. *N Biotechnol* **84**, 96–104 (2024).

126. Philip, P. *et al.* Parallel substrate supply and pH stabilization for optimal screening of *E. coli* with the membrane-based fed-batch shake flask. *Microb Cell Fact* **17**, 1–17 (2018).

127. Andersen, K. B. & Von Meyenburg, K. Are growth rates of *Escherichia coli* in batch cultures limited by respiration? *J Bacteriol* **144**, 114–123 (1980).

128. Da Silva, S. B., Cantarelli, V. V. & Ayub, M. A. Z. Production and optimization of poly-γ-glutamic acid by *Bacillus subtilis* BL53 isolated from the Amazonian environment. *Bioprocess Biosyst Eng* **37**, 469–479 (2014).

129. Shu, C. -H & Yang, S. -T. Effects of temperature on cell growth and xanthan production in batch cultures of *Xanthomonas campestris*. *Biotechnol Bioeng* **35**, 454–468 (1990).

130. García-Ochoa, F., Castro, E. G. & Santos, V. E. Oxygen transfer and uptake rates during xanthan gum production. *Enzyme Microb Technol* **27**, 680–690 (2000).

6 Appendix

Appendix 1: Parameters are taken from the VDI Heat Atlas.

$\sigma_{water,30°C}$	70 mN/m
$\rho_{water,25°C}$	997 kg/m^3
$\rho_{water,37°C}$	993 kg/m^3
$\eta_{water,25°C}$	0.89 mPa·s
$\eta_{water,37°C}$	0.69 mPa·s
$\rho_{air,30°C}$	1.2 kg/m^3
$\eta_{air,30°C}$	0.02 mPa·s

Appendix 2: Shake flasks milled to half their maximal outer diameter to evaluate the exact geometry of the flasks.

Front view of milled down shake flasks. Three shake flasks of the same type and from same manufacturer were used as replicates. Inner measurements of the flask geometry provided in the main manuscript are mean values from the three shown flasks. Shake flasks were milled down by Aachener Quarzglas-Technologie Heinrich GmbH & Co.KG. Results are specified in Fig. 7 and 8.

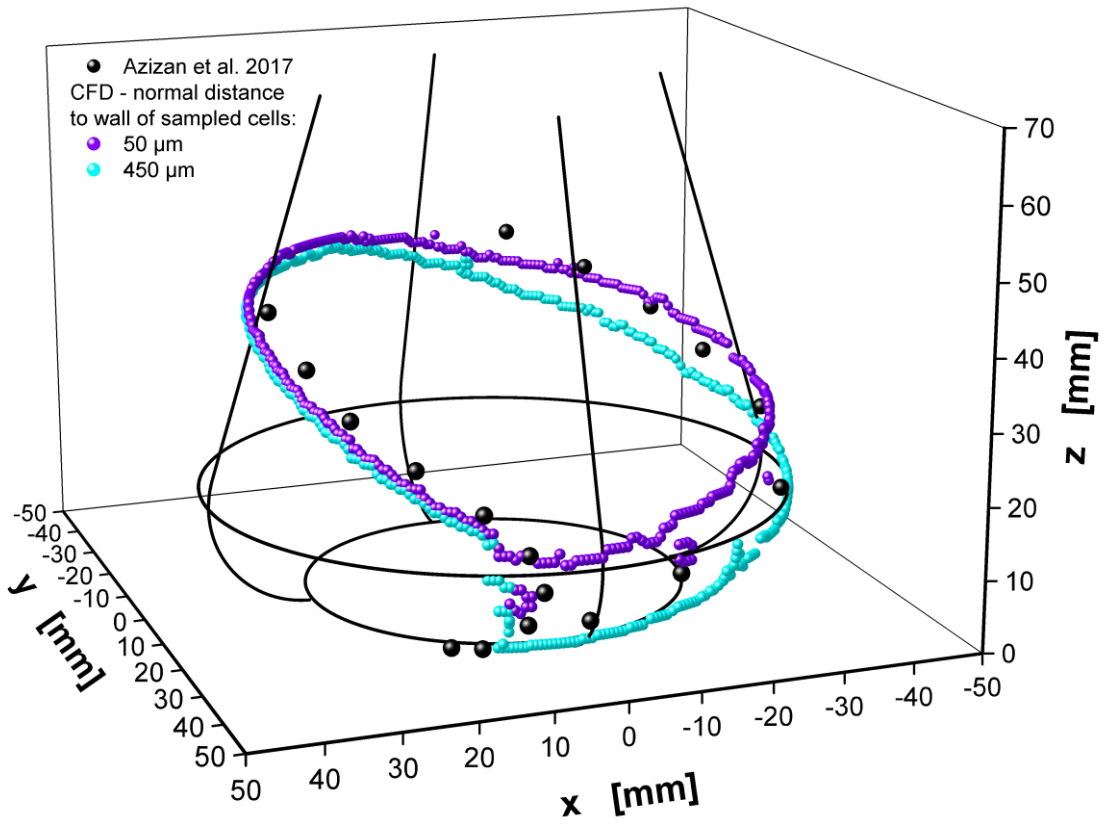

Appendix 3: 3D-representation of the comparison of liquid contact lines from CFD and experimental data[6]

Depicted is the same simulation as in Fig. 5A, only as a 3D-representation for distances of 50 to 450 µm normal to the shake flask wall to exclude the liquid film (see Fig. 8A). The figure becomes incomprehensible for more than two normal distances. Simulated conditions: Viscosity (η) = 0.69 mPa·s, shaking diameter (d_0) = 2.5 cm, filling volume (V_L) = 40 mL, shaking frequency (n) = 250 rpm, surface tension (σ) = 70 mN/m, contact angle (Θ) = 20°, temperature (T) = 25°C

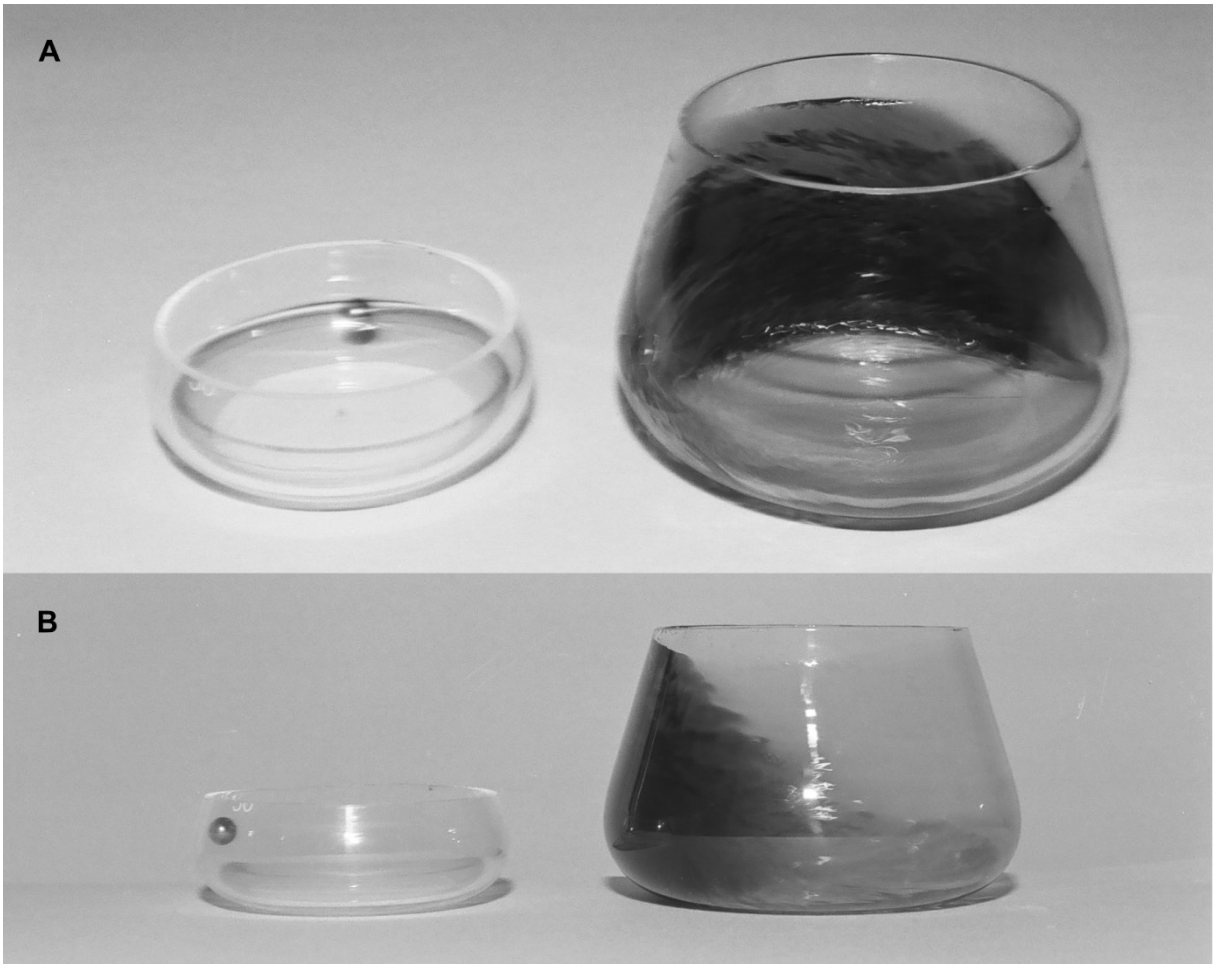

Appendix 4: Photograph of the liquid distribution at a shaking frequency of 450 rpm, viscosity of 1 mPa·s, shaking diameter of 2.5 cm and filling volume of 25 mL.

In (A) a photograph of the rotating bulk liquid in line with the centrifugal force is shown. The photograph in (B) is taken perpendicular to the centrifugal force, focusing on the tail region, following the rotating bulk liquid. The small metal balls on the left of (A) and (B) are included to show the direction of the centrifugal force. The formed liquid film can be seen in (B) as a light shadow up to the maximal liquid height. Contrary to all previous images, experimental results and CFD simulations, the shaking motion in these images is counter-clockwise.

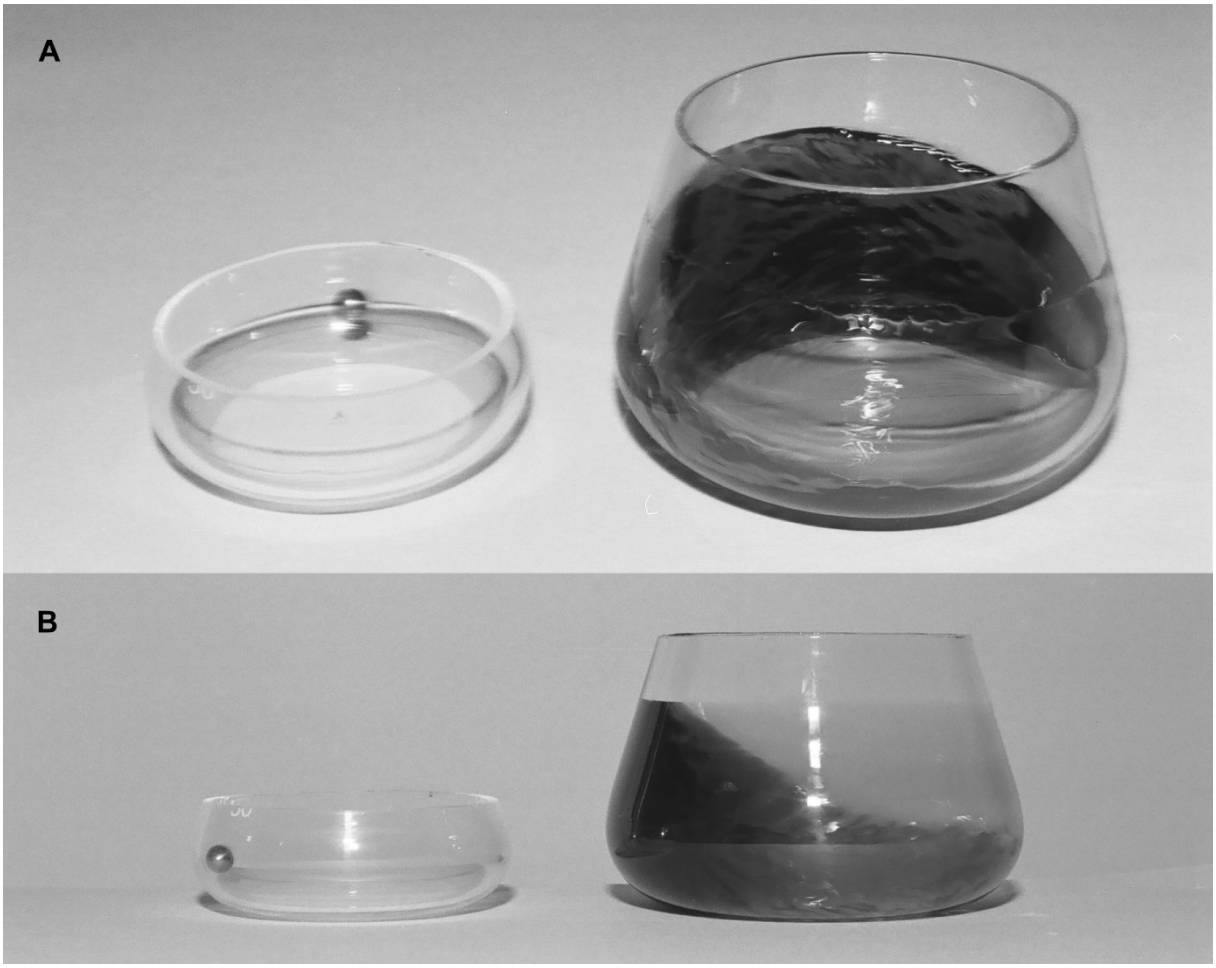

Appendix 5: Photograph of the liquid distribution at a shaking frequency of 300 rpm, viscosity of 1 mPa·s, shaking diameter of 2.5 cm and filling volume of 25 mL.

In (A) a photograph of the rotating bulk liquid in line with the centrifugal force is shown. The photograph in (B) is taken perpendicular to the centrifugal force, focusing on the tail region, following the rotating bulk liquid. The small metal balls on the left of (A) and (B) are included to show the direction of the centrifugal force. The formed liquid film can be seen in (B) as a light shadow up to the maximal liquid height. Contrary to all previous images, experimental results and CFD simulations, the shaking motion in these images is counter-clockwise.

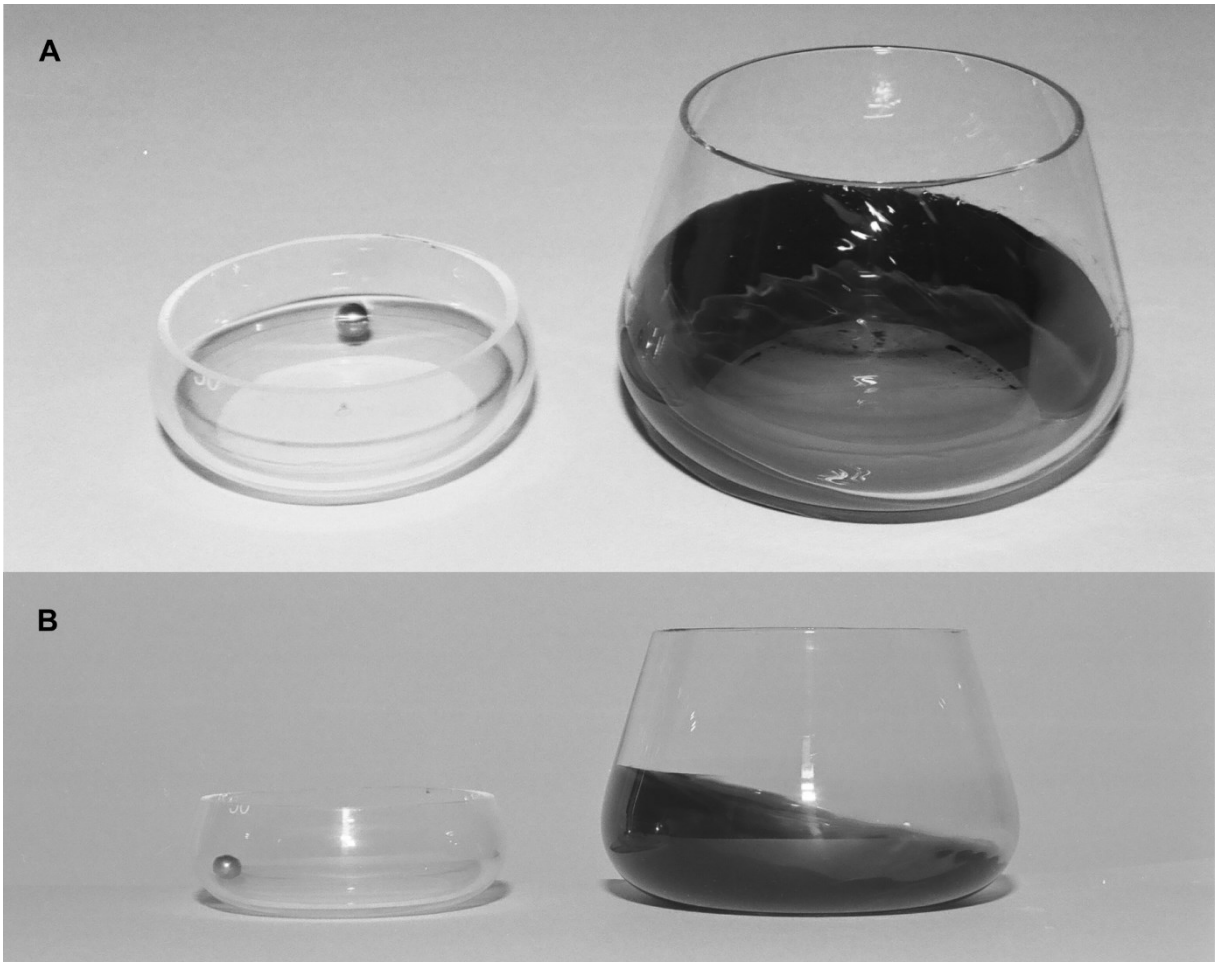

Appendix 6: Photograph of the liquid distribution at a shaking frequency of 150 rpm, viscosity of 1 mPa·s, shaking diameter of 2.5 cm and filling volume of 25 mL.

In (A) a photograph of the rotating bulk liquid in line with the centrifugal force is shown. The photograph in (B) is taken perpendicular to the centrifugal force, focusing on the tail region, following the rotating bulk liquid. The small metal balls on the left of (A) and (B) are included to show the direction of the centrifugal force. Contrary to all previous images, experimental results and CFD simulations, the shaking motion in these images is counter-clockwise.

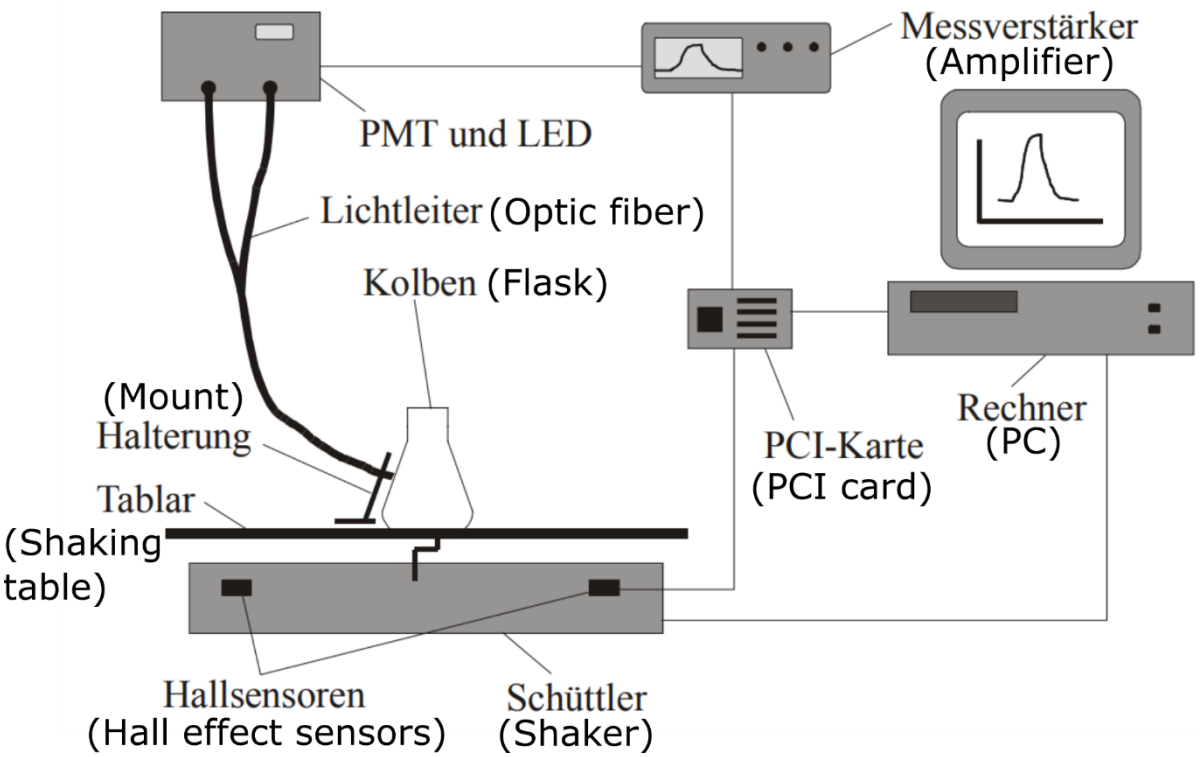

Appendix 7: Schematic of the setup for liquid thickness measurements (taken from Hermann[82]).

The figure is taken from the dissertation of Hermann[82]. Translations added in brackets. The setup was used to perform liquid thickness measurements in shake flasks. An optical fiber is mounted next to a shake flask, placed on a shaker table. Half of the optical fiber is connected to a blue LED (350 – 500 nm) for excitation of fluorescence and the other half to a photomultiplier (PMT) to record the fluorescence emission (above 570 nm). The signal form the PMT was transmitted through an amplifier and recorded on a computer. Hall effect sensors were installed within the shaker to monitor the position of the shaker and the direction of centrifugal force. The measurement frequency was 5000 Hz.

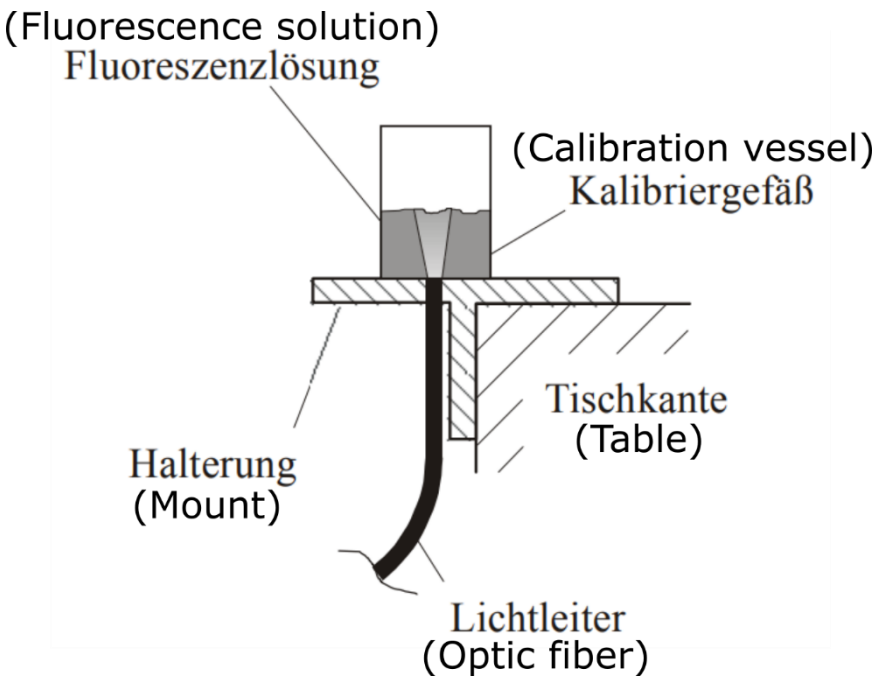

Appendix 8: Schematic of setup for the calibration of liquid thickness measurements (taken from Hermann[82]).

The figure is taken from the dissertation of Hermann[82]. Translations added in brackets. The setup was used to record a calibration, to convert recorded fluorescence intensities (Appendix 7) to liquid thickness. A custom plexiglass well was constructed and placed above the optical fiber of the fluorescence measurement system (Appendix 7). For the calibration the volume, hence, height of the fluorescent solution was incrementally increased and the resulting fluorescence intensity measured. With this data a calibration curve was created.

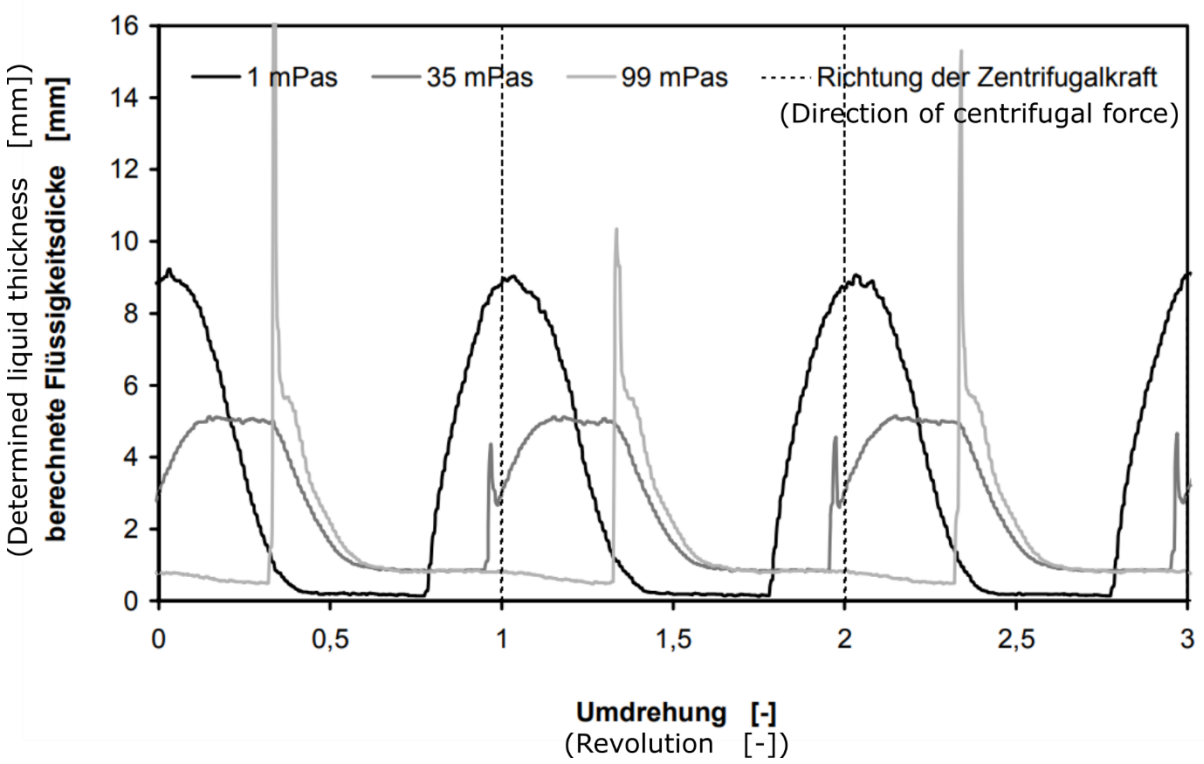

Appendix 9: Liquid thickness in shake flasks for three viscosities based on fluorescence measurements (taken from Hermann[82]).

The figure is taken from the dissertation of Hermann[82]. Translations added in brackets. Measurements were performed with the setup shown in Appendix 7 and calibrated according to Appendix 8. The calculated liquid thickness (y-axis) is plotted over three full rotations of the shake flask (x-axis) for three different viscosities. The dashed vertical lines indicate the direction of the centrifugal force. At zero revolutions the bulk liquid is in front of the sensor for 1 mPa·s. At this point the liquid thickness of the bulk liquid is determined to be roughly 9 mm. After half a rotation the bulk liquid has passed the sensor and the liquid thickness of the film is measured with about 50 µm. At a viscosity of 35 and 99 mPa·s, the liquid film starts similar in liquid thickness with about 800 µm. At 35 mPa·s, the film stays at that thickness until the bulk liquid moves in front of the sensor again. At 99 mPa·s, the film thickness decreases further to about 500 µm. The spike in the liquid thickness, when the bulk liquid arrives at the sensor (measured fluorescence intensity) at 35 and 99 mPa·s is explained by Hermann with possible reflection effects in the leading edge of the bulk liquid. Experimental conditions: Viscosity (η) = 1, 35, 99 mPa·s, shaking diameter (d_0) = 2.5 cm, filling volume (V_L) = 25 mL, shaking frequency (n) = 300 rpm, 2.5 µm fluorescein, fluorescence sensor height = 20.6 mm.

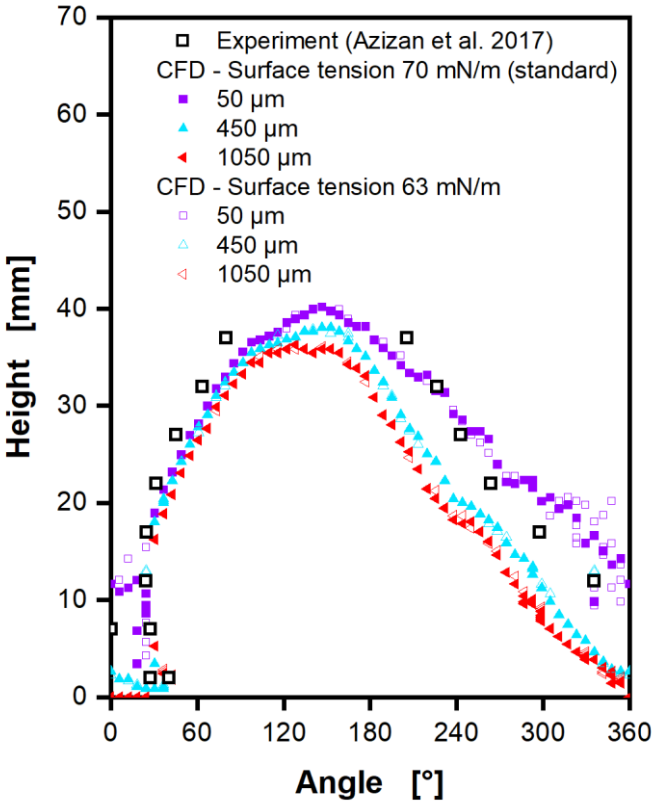

Appendix 10: Impact of the assumed surface tension on the liquid contact line calculated by the CFD model, compared to experimental data[6]

The liquid contact lines are shown in mm, viewed from the center of the shake flask, rotating around the z-axis (see Fig. 1C). Liquid contact lines from CFD calculations were extracted at multiple distances from 50 to 1050 µm normal to the shake flask wall to exclude the liquid film (see Fig. 8A). Simulated conditions: Viscosity (η) = 0.69 mPa·s, shaking diameter (d_0) = 2.5 cm, filling volume (V_L) = 30 mL, shaking frequency (n) = 250 rpm, surface tension (σ) = 70 mN/m and 63 mN/m, contact angle (Θ) = 20°, temperature (T) = 37°C

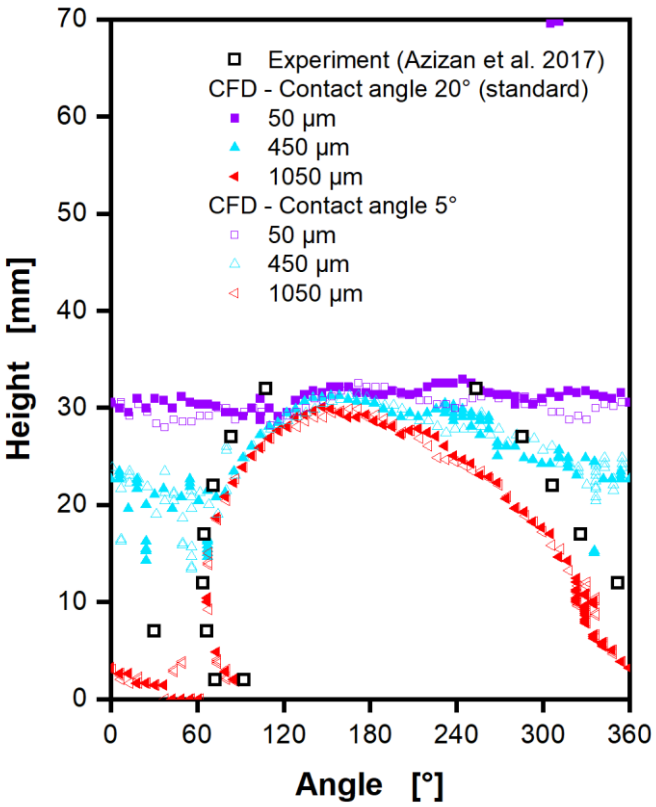

Appendix 11: Impact of the assumed contact angle on the liquid contact line calculated by the CFD model, compared to experimental data[6]

The liquid contact lines are shown in mm, viewed from the center of the shake flask, rotating around the z-axis (see Fig. 1C). Liquid contact lines from CFD calculations were extracted at multiple distances from 50 to 1050 µm normal to the shake flask wall to exclude the liquid film (see Fig. 8A). Simulated conditions: Viscosity (η) = 16.7 mPa·s, shaking diameter (d_0) = 2.5 cm, filling volume (V_L) = 30 mL, shaking frequency (n) = 250 rpm, surface tension (σ) = 70 mN/m, contact angle (Θ) = 20° and 5°, temperature (T) = 25°C

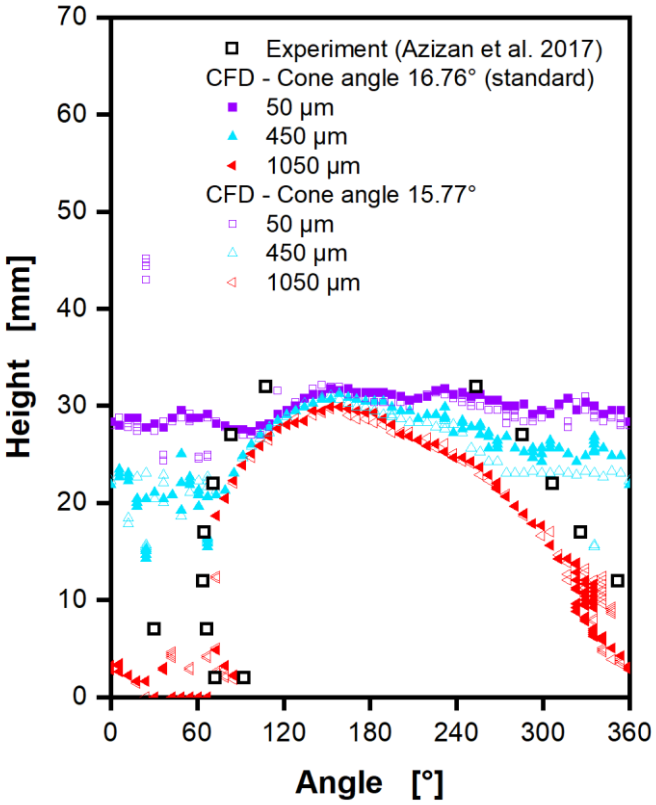

Appendix 12: Impact of the cone angle on the liquid contact line calculated by the CFD model, compared to experimental data[6]

The liquid contact lines are shown in mm, viewed from the center of the shake flask, rotating around the z-axis (see Fig. 1C). Liquid contact lines from CFD calculations were extracted at multiple distances from 50 to 1050 µm normal to the shake flask wall to exclude the liquid film (see Fig. 8A). Simulated conditions: Viscosity (η) = 16.7 mPa·s, shaking diameter (d_0) = 2.5 cm, filling volume (V_L) = 30 mL, shaking frequency (n) = 250 rpm, surface tension (σ) = 70 mN/m, contact angle (Θ) = 20°, temperature (T) = 25°C

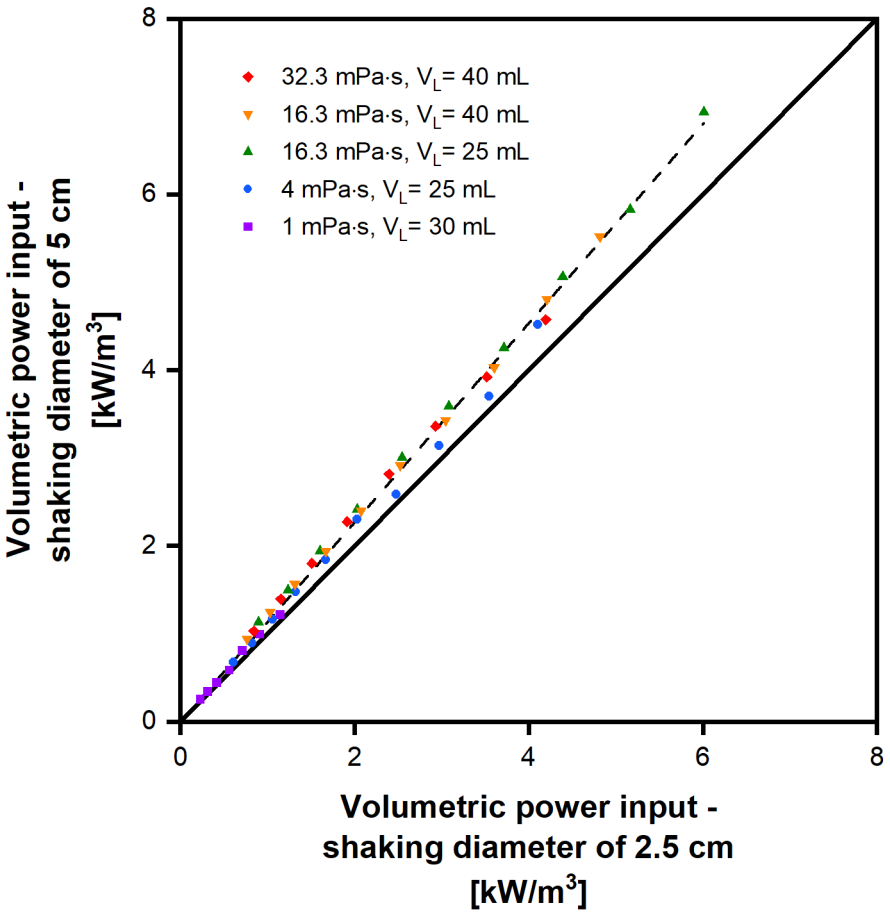

Appendix 13: Parity plot of experimentally determined volumetric power inputs from Büchs et al.[4] at a shaking diameter of 2.5 and 5cm.

The black bold line indicates parity and the dashed black line a linear fit of the data. The linear fit indicates roughly 13 % greater volumetric power inputs at a shaking diameter of 5 cm. Experimental conditions: Viscosity (η) = 1 – 32.3 mPa·s, shaking diameter (d_0) = 2.5 and 5 cm, filling volume (V_L) = 25 - 40 mL, shaking frequency (n) = 180 - 360 rpm

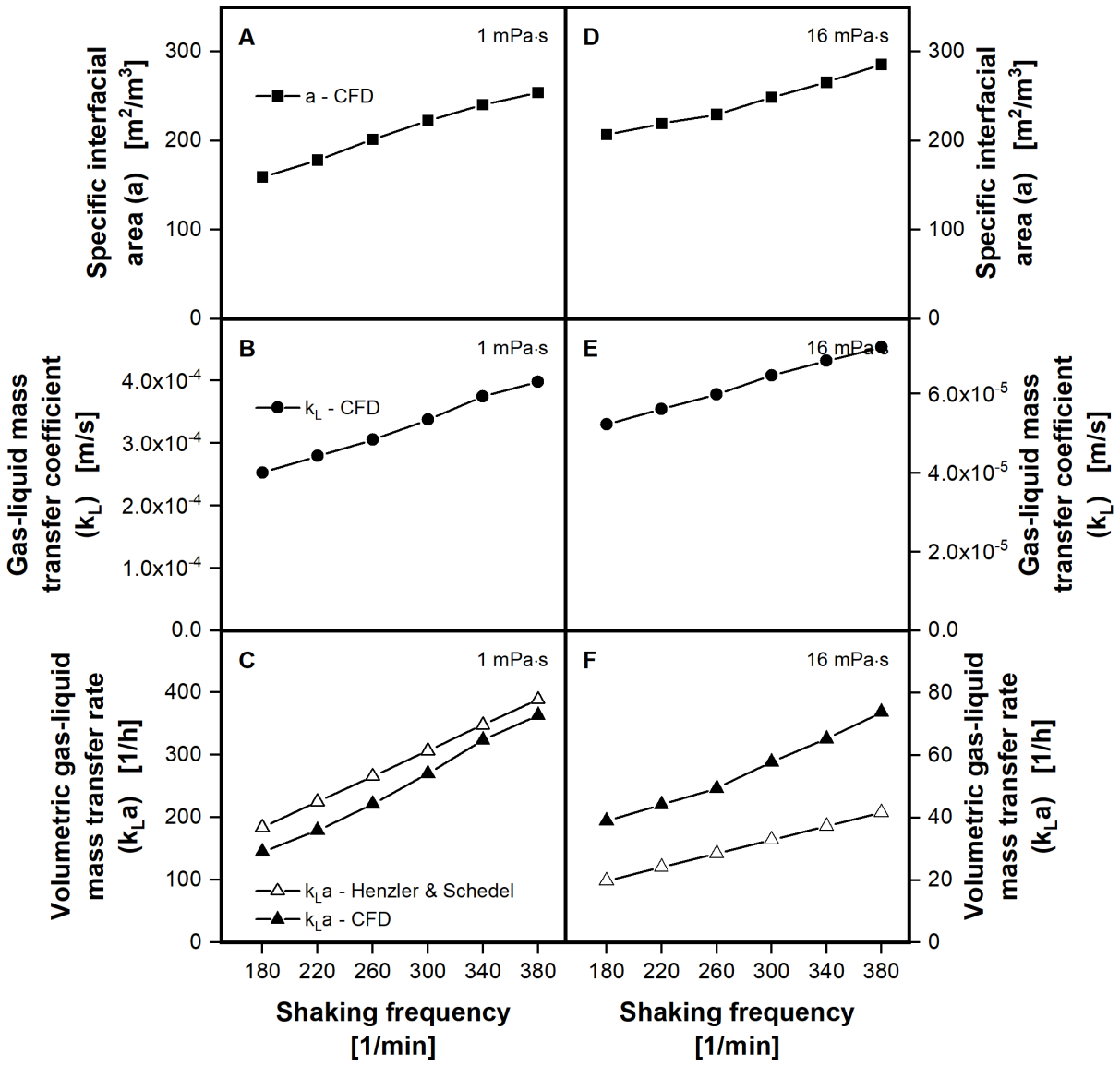

Appendix 14: The k_La value derived from CFD simulations as function of shaking frequency at a filling volume of 40 mL and viscosity of 1 and 16 mPa·s.

The specific interfacial area a (A + D), gas-liquid mass transfer coefficient k_L (B + E) and volumetric gas-liquid mass transfer rate k_La (C+ F) are derived from the CFD simulations and depicted as a function of viscosity. The k_La values from the CFD simulations in C and F are compared to values calculated with the k_La correlation from Henzler & Schedel (Eq. 37). Simulated conditions: Shaking frequency (n) = 180 - 340 rpm (A – C) and 180 – 380 rpm (D – F), shaking diameter (d_0) = 25 mm, surface tension (σ) = 70 mN/m, contact angle (Θ) = 20°, temperature (T) = 20 °C, viscosity (η) = 1 mPa·s (A – C) and 16 mPa·s (D – F), filling volume V_L = 40 mL

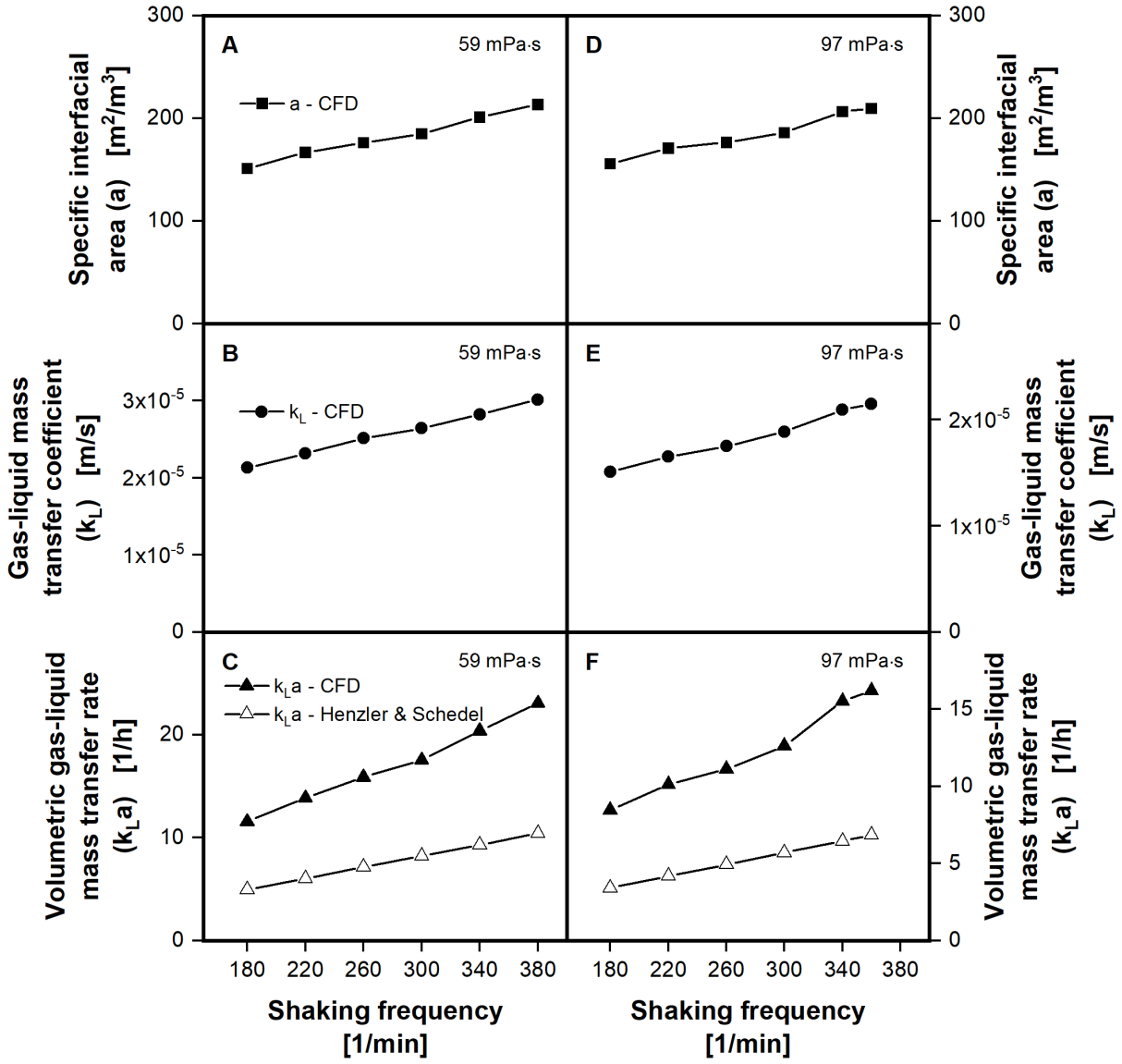

Appendix 15: The k_La value derived from CFD simulations as function of shaking frequency at a filling volume of 40 mL and viscosity of 59 and 97 mPa·s.

The specific interfacial area a (A + D), gas-liquid mass transfer coefficient k_L (B + E) and volumetric gas-liquid mass transfer rate k_La (C+ F) are derived from the CFD simulations and depicted as a function of viscosity. The k_La values from the CFD simulations in C and F are compared to values calculated with the k_La correlation from Henzler & Schedel (Eq. 37). Simulated conditions: Shaking frequency (n) = 180 - 348 rpm (A – C) and 180 – 360 rpm (D – F), shaking diameter (d_0) = 25 mm, surface tension (σ) = 70 mN/m, contact angle (Θ) = 20°, temperature (T) = 20 °C, viscosity (η) = 59 mPa·s (A – C) and 97 mPa·s (D – F), filling volume V_L = 40 mL

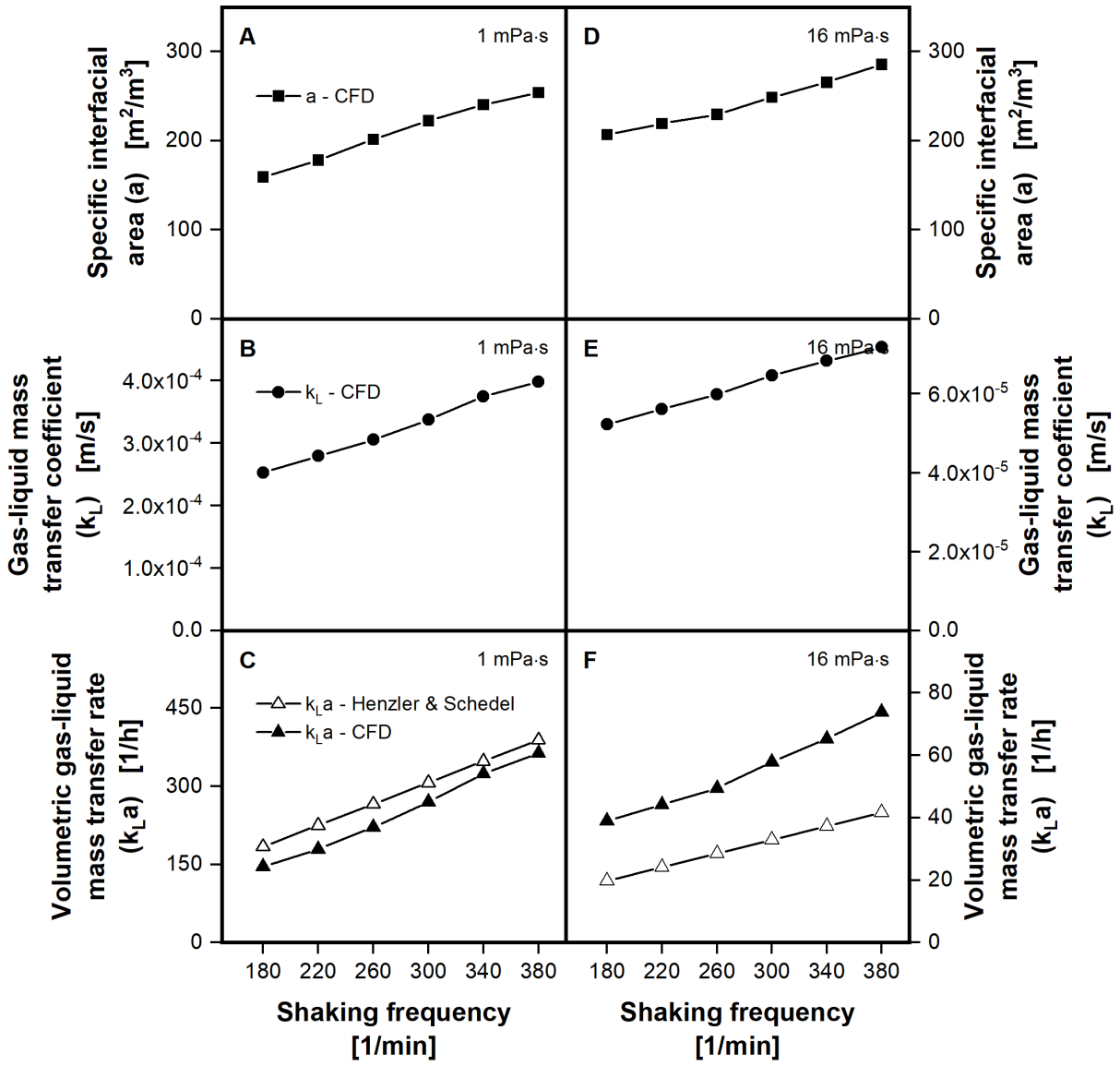

Appendix 16: The k_La value derived from CFD simulations as function of shaking frequency at a filling volume of 25 mL and viscosity of 1 and 16 mPa·s.

The specific interfacial area a (A + D), gas-liquid mass transfer coefficient k_L (B + E) and volumetric gas-liquid mass transfer rate k_La (C+ F) are derived from the CFD simulations and depicted as a function of viscosity. The k_La values from the CFD simulations in C and F are compared to values calculated with the k_La correlation from Henzler & Schedel (Eq. 37). Simulated conditions: Shaking frequency (n) = 180 - 380 rpm, shaking diameter (d_0) = 25 mm, surface tension (σ) = 70 mN/m, contact angle (Θ) = 20°, temperature (T) = 20 °C, viscosity (η) = 1 mPa·s (A – C) and 16 mPa·s (D – F), filling volume V_L = 25 mL

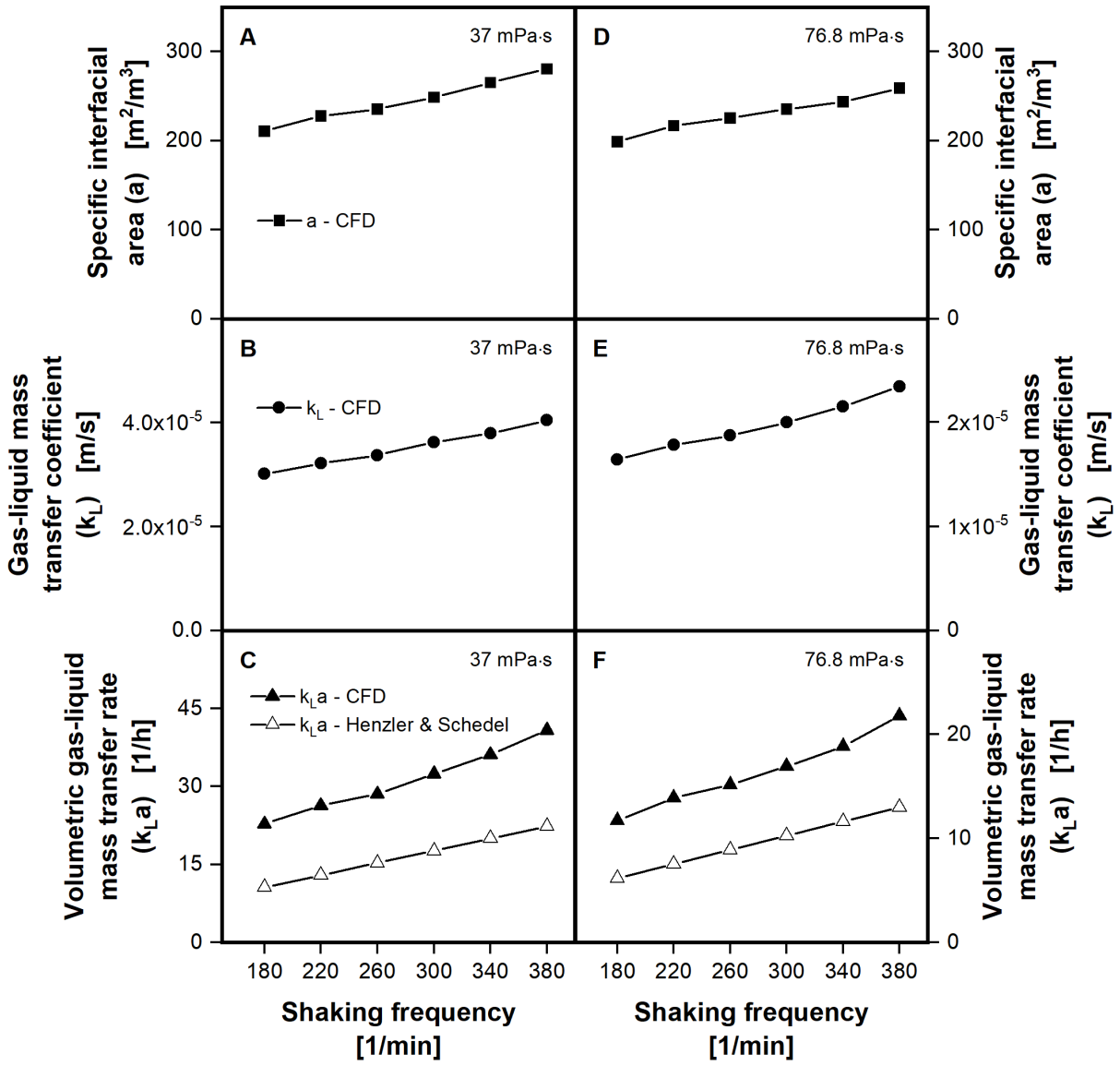

Appendix 17: The k_La value derived from CFD simulations as function of shaking frequency at a filling volume of 25 mL and viscosity of 37 and 76.8 mPa·s.

The specific interfacial area a (A + D), gas-liquid mass transfer coefficient k_L (B + E) and volumetric gas-liquid mass transfer rate k_La (C+ F) are derived from the CFD simulations and depicted as a function of viscosity. The k_La values from the CFD simulations in C and F are compared to values calculated with the k_La correlation from Henzler & Schedel (Eq. 37). Simulated conditions: Shaking frequency (n) = 180 - 380 rpm, shaking diameter (d_0) = 25 mm, surface tension (σ) = 70 mN/m, contact angle (Θ) = 20°, temperature (T) = 20 °C, viscosity (η) = 37 mPa·s (A – C) and 76.8 mPa·s (D – F), filling volume V_L = 25 mL

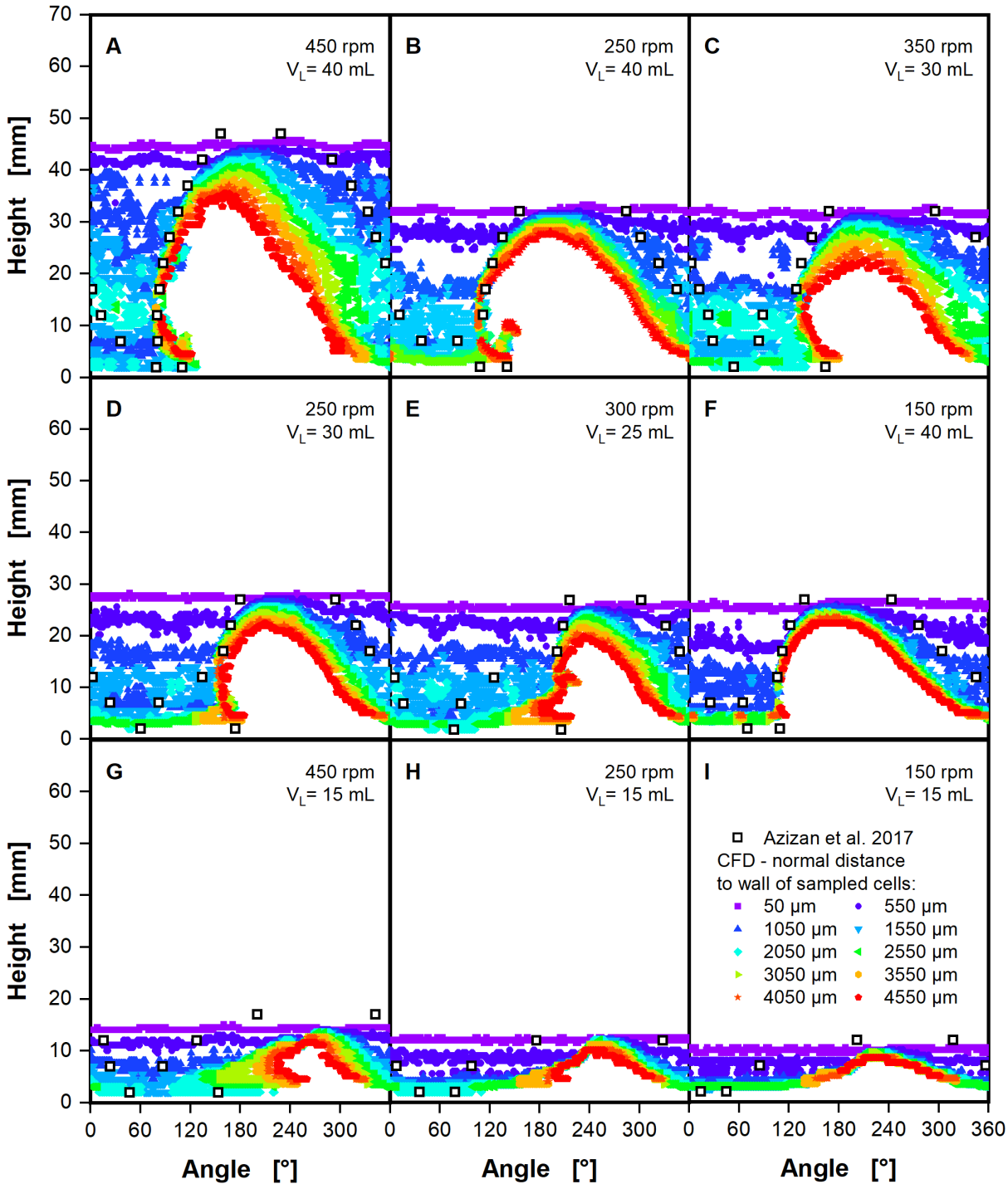

Appendix 18: Liquid contact lines extracted from the CFD model, simulating a power law, shear thinning liquid with the calculation of shear rates, as provided by OpenFOAM.

The liquid contact lines are shown in mm, viewed from the center of the shake flask, rotating around the z-axis (see Fig. 2-1). To exclude the liquid film, liquid contact lines from CFD were extracted at multiple distances from 50 to 4550 µm normal to the shake flask wall (Fig. 2-3A). Instead of determining a Newtonian viscosity for the simulations, as done in Fig. 2-8, consistency factor and flow behavior index are used in the CFD simulation and shear rates estimated by OpenFOAM. Simulated cases are essentially identical to the simulations shown in Fig. 2-8, except in the description of the rheological behavior. Simulated conditions: Shaking diameter (d_0) = 25 mm, surface tension (σ) = 70 mN/m, contact angle (Θ) = 20°, temperature (T) = 20°C, consistency factor (K) = 104 mPa·s, (m) flow behavior index = 0.956

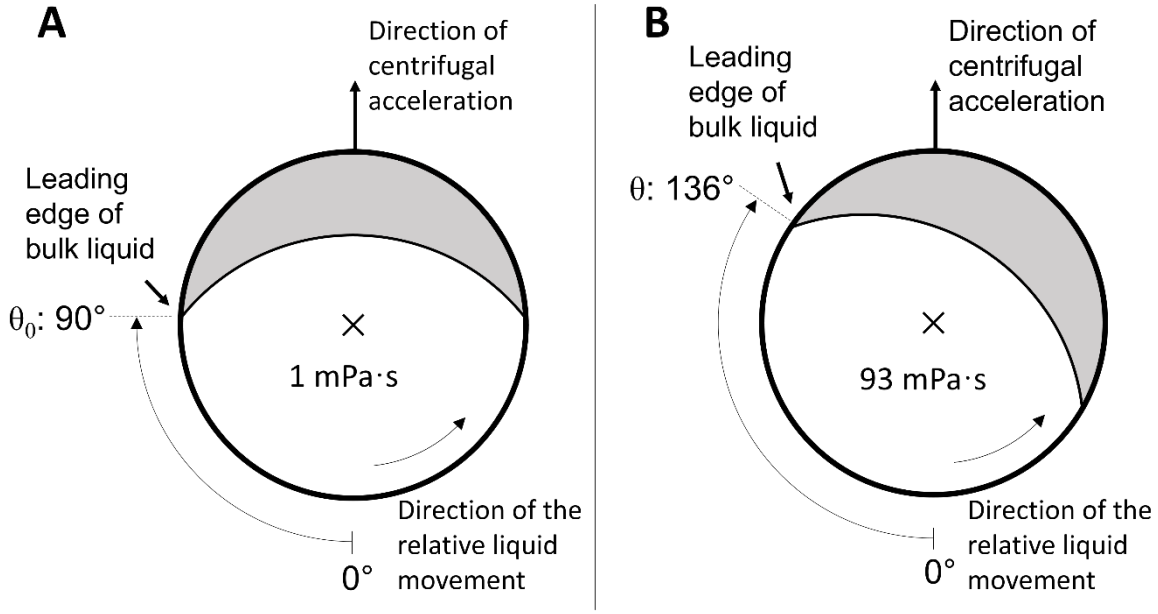

Appendix 19: Schematic view of the position of the rotating bulk liquid in shake flasks at two different viscosities.

A: The initial viscosity is low (1 mPa•s), the angle θ_0 of bulk liquid is 90°. **B**: The viscosity is high (93 mPa•s), the angle θ of bulk liquid increases from 90° to 136°. The zero position is defined by a built-in acceleration sensor. Figure adapted from Sieben[119].

Appendix 20: Preparation of 1 L of Wilms-MOPS minimal medium for cultivation of *Escherichia coli*.

Solution	Volume [mL]
Base solution	500
Trace elements solution (1000x)	1
Glucose (25x)	40
Magnesium sulfate (100x)	10
Thiamine (1000x)	1
Ampicillin (1000x)	1
Deionized water	447

Appendix 21: Composition of Wilms-MOPS base solution for cultivation of *Escherichia coli*.

Substance	Concentration [g/L]
Ammonium sulfate	13.96
Dipotassium hydrogen phosphate	6
Sodium sulfate	4
MOPS	83.7

The pH of the base solution was adjusted to a pH of 7.5. The solution was autoclaved at 121°C for 20 min.

Appendix 22: Composition of Wilms-MOPS trace elements solution for cultivation of *Escherichia coli*.

Substance	Concentration [g/L]
Zinc sulfate heptahydrate	0.54
Copper sulfate pentahydrate	0.48
Manganese sulfate monohydrate	0.30
Cobalt dichloride hexahydrate	0.54
Iron trichloride hexahydrate	41.76
Calcium chloride dihydrate	1.98
Titriplex III	33.40

The trace solution was sterile filtered with a pore size of 0.2 µm.

Appendix 23: Composition of Wilms-MOPS stock solutions for cultivation of *Escherichia coli*.

Solution	**Substance**	**Concentration [g/L]**
Glucose (25x)	Glucose monohydrate	550
Magnesium sulfate (100x)	Magnesium sulfate heptahydrate	50
Thiamine (1000x)	Thiamine hydrochloride	10
Ampicillin (1000x)	Ampicillin sodium salt	100

The glucose solution was autoclaved at 121°C for 20 min. Other solutions were sterile filtered with a pore size of 0.2 µm.

Appendix 24: Composition of the MM1P100 medium for cultivation of *Paenibacillus polymyxa*.

Substance	Concentration
Glucose monohydrate	33 g/L
Casein peptone (Carl Roth GmbH & Co.)	5 g/L
Magnesium sulfate heptahydrate	1.33 g/L
Potassium dihydrogen phosphate	1.67 g/L
Calcium chloride dihydrate	0.05 g/L
Vitamin solution RPMI 1640 (100x) (Sigma-Aldrich)	10 mL/L
Trace elements solution (1000x)	1 mL/L

All solutions were prepared as individual stock solutions. The pH value of the potassium dihydrogen phosphate solution was adjusted to 7.0 with potassium hydroxide. The trace elements solution and potassium dihydrogen phosphate solution were sterile filtrated. The vitamin solution was purchased sterile. All other solutions were autoclaved at 121 °C for 20 min.

Appendix 25: Composition of the trace elements solution for MM1P100 medium for cultivation of *Paenibacillus polymyxa*.

Substance	Concentration [g/L]
Iron sulfate heptahydrate	2.5
Sodium tartrate dihydrate	2.1
Manganese chloride tetrahydrate	1.8
Cobalt chloride hexahydrate	0.075
Copper sulfate heptahydrate	0.031
Boric acid	0.258
Sodium molybdate	0.023
Zinc chloride	0.021

Appendix 26: Composition of YM medium for cultivation of *Xanthomonas campestris*.

Substance	**Concentration [g/L]**
Glucose monohydrate	11
Yeast extract (Carl Roth GmbH & Co.)	3
Malt extract (Sigma-Aldrich)	3
Peptone (Carl Roth GmbH & Co.)	5
MOPS	30

To avoid the Maillard reaction, complex components were autoclaved separately from the non-complex components. Complex components and non-complex components were prepared with a 10-fold concentration. The YM medium was completed by mixing both solutions and diluting them with heat sterilized deionized water.

Appendix 27: Composition of GY medium for cultivation of *Xanthomonas campestris*.

Substance	**Concentration [g/L]**
Glucose monohydrate	27.5
Yeast extract (Carl Roth GmbH & Co.)	25
Potassium dihydrogen phosphate	2
Magnesium sulfate heptahydrate	0.205
MOPS	30

To avoid the Maillard reaction, complex components were autoclaved separately from the non-complex components. Complex components and non-complex components were prepared with a 10-fold concentration. The GY medium was completed by mixing both solutions and diluting them with heat sterilized deionized water.

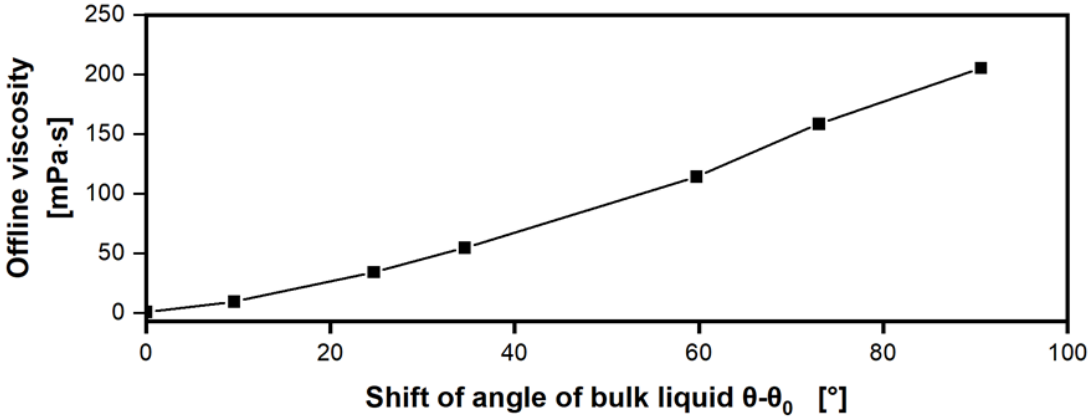

Appendix 28: Calibration of the viscosity measurement of the ShakeVisc system.

The calibration was performed with glycerol – water mixtures of different viscosities. Calibration conditions: 0.2 mg/mL Oxnano nanoparticles, shaking frequency (n) = 200 rpm, filling volume (V_L) = 30 mL, shaking diameter (d_0) = 50 mm, temperature (T) = 30°C.

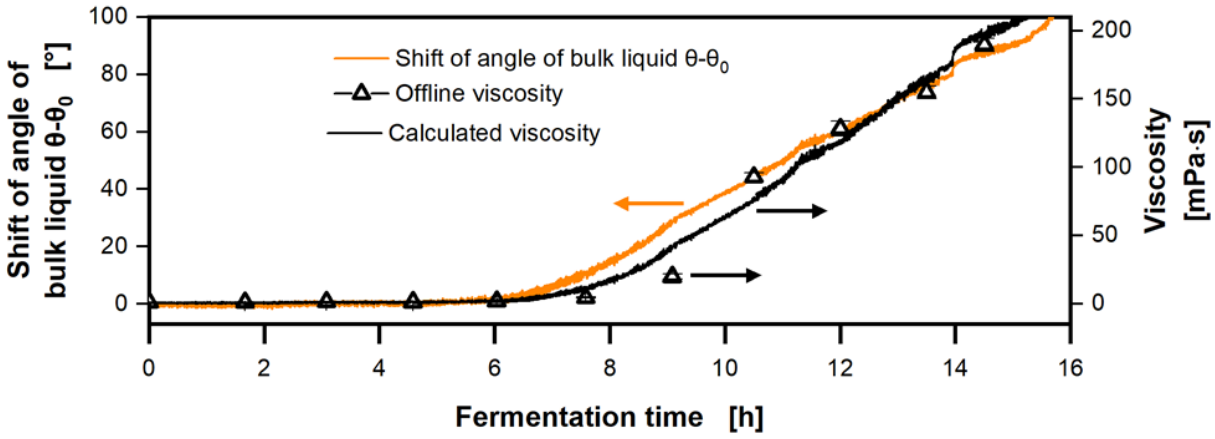

Appendix 29: Comparison of calculated viscosity, based on calibration, to offline measured viscosity of the *Paenibacillus polymyxa* cultivation from Fig. 3-7.

Calibration is shown in Appendix 28. Cultivation conditions: MM1P100 medium with 30 g/L glucose, 0.2 mg/mL Oxnano nanoparticles, initial pH = 7, initial OD600 = 0.5, shaking frequency (n) = 200 rpm, filling volume (VL) = 30 mL, shaking diameter (d0) = 50 mm, temperature (T) = 30°C. Standard deviation of offline viscosity measurements is barely visible, as it is smaller than the data points.

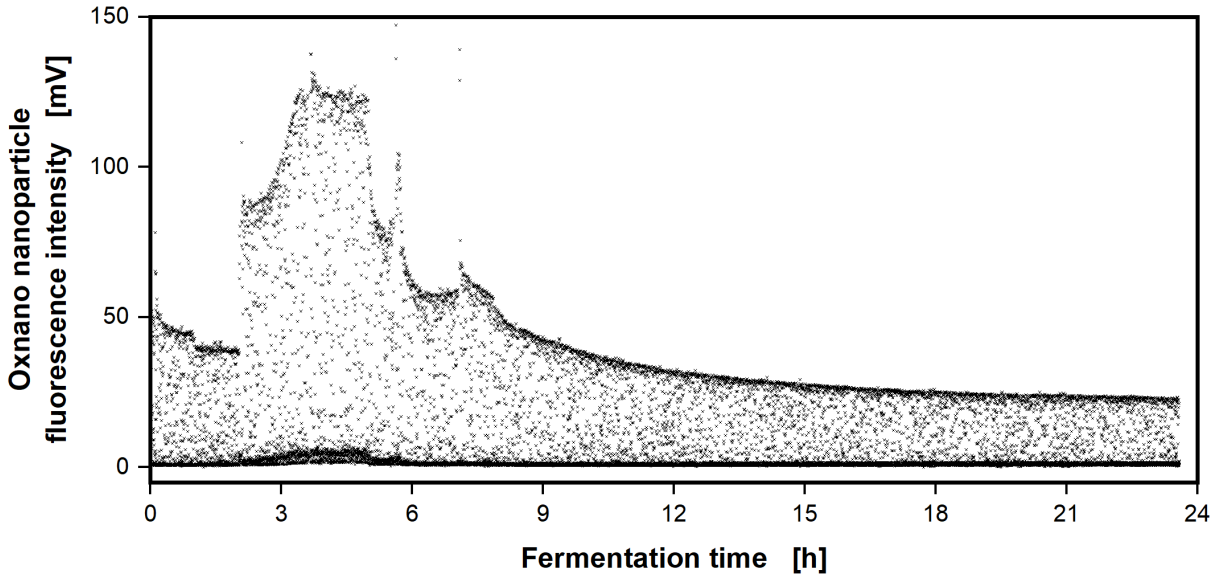

Appendix 30: Fluorescence intensity of Oxnano nanoparticles of the *Escherichia coli* cultivation from Fig. 3-4.

The upper boundary layer represents measurements from the bulk liquid. Beneath a signal intensity of 25 mV, the Oxnano nanoparticle system is known to no longer produce reliable values.

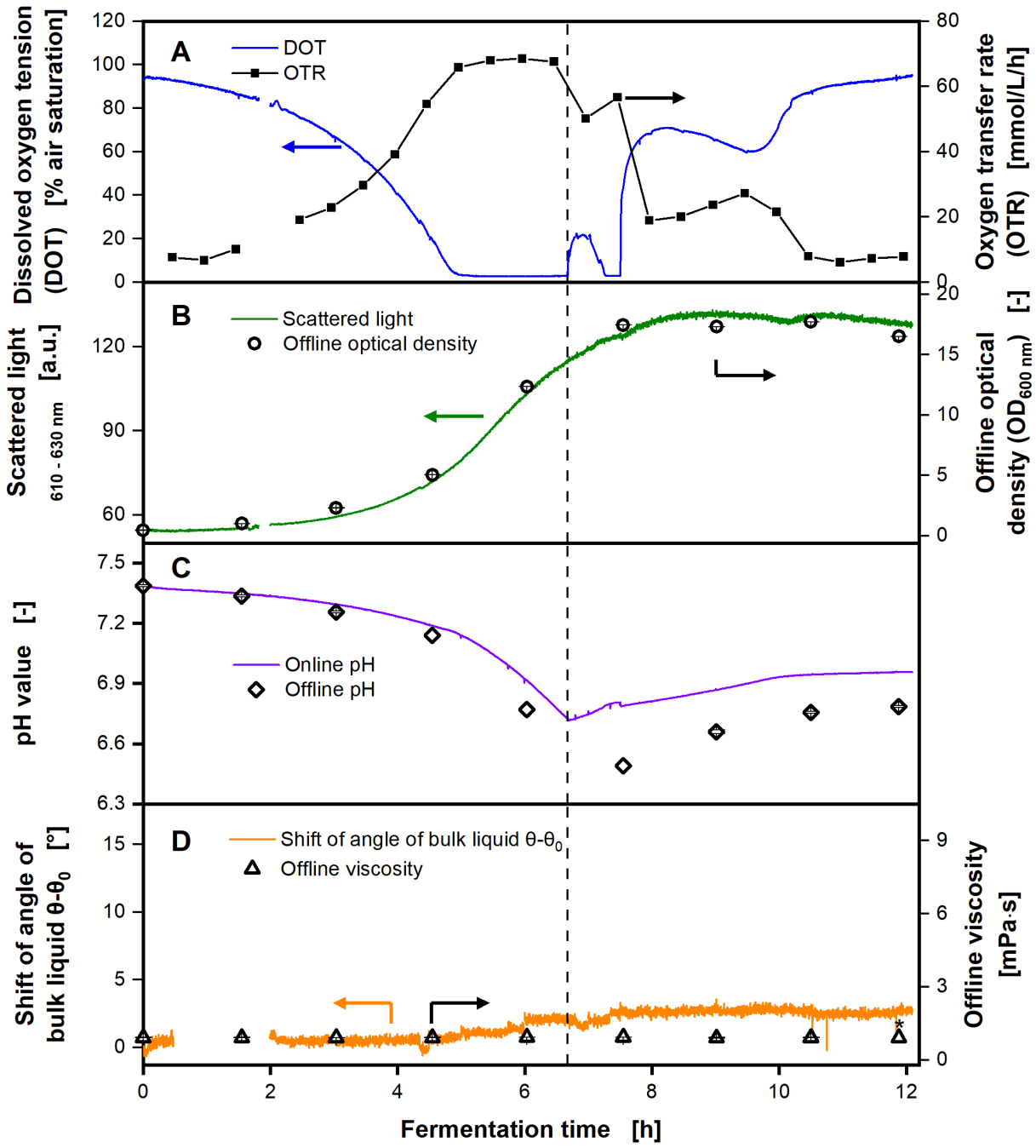

Appendix 31: Online monitoring of an *Escherichia coli* cultivation with a triggered ShakeVisc device and a RAMOS device.

This cultivation was a reproduction of the cultivation shown in Fig. 3-5. (A) Online monitoring of dissolved oxygen tension (DOT) and oxygen transfer rate (OTR), with Oxnano nanoparticles and a RAMOS device, respectively. The DOT was calibrated to 100 % in the non-inoculated medium prior to starting the monitoring. (B) Online monitoring of scattered light, compared to optical density measurements from offline samples at 600 nm. (C) Online monitoring of the pH value with pH sensitive spots, compared to offline pH, measured from offline samples. The pH spot was not calibrated before the cultivation. (D) Online monitoring of the shift of angle of bulk liquid θ-θ_0, compared to the offline viscosity, measured from offline samples with a rheometer. All offline samples were taken from separate shake flasks, cultivated in parallel. The vertical dashed line indicates the sudden change in DOT and pH after 6.5 hours. Missing data points (0.5 h – 2 h) are due to a malfunction of the lab shaker. Triggering of the measurement of the bulk liquid was enabled by an acceleration sensor, according to the illustration in Fig. 3-3B. Cultivation conditions: Wilms-MOPS medium with 20 g/L glucose, 0.2 mg/mL Oxnano nanoparticles, range of pH spot = 6 – 8, initial pH = 7.5, initial OD_{600} = 0.5, shaking frequency (n) =

350 rpm, filling volume (V_L) = 10 mL, shaking diameter (d_0) = 50 mm, temperature (T) = 37°C. Standard deviation is barely visible, as it is smaller than the data points. Measurements of offline optical density OD_{600} and offline viscosity were performed in duplicate. *Only single measurement was performed.

Appendix 32: Calculation of the specific oxygen uptake rate (qO_2)

The online measured oxygen transfer rate (OTR) and the online measured scattered light signals allow the calculation of the specific oxygen uptake rate (qO_2). The scattered light signal was correlated to the optical density (OD_{600}). Since no cell dry (CDW) weight measurements were conducted in this work, correlation between optical density and CDW were taken from literature. Hence, the online scattered light measurements can be converted to the CDW.

The qO_2 can be calculated as follows:

$$qO_2\ [mmol\ \cdot g^{-1} \cdot h^{-1}] = OTR\ [mmol\ \cdot L^{-1} \cdot h^{-1}]/CDW\ [g \cdot L^{-1}] \quad (1)$$

The calculated qO_2 values were then compared to qO_2 values found in literature. Until oxygen limitation is reached, the calculated qO_2 values are in the same range as qO_2 values reported in literature, as shown in Appendix 33, Appendix 35 and Appendix 37. Deviations are due to different cultivation conditions between data from literature and this work. In literature, fermenters were used as cultivation vessels, instead of shake flasks, also media composition differ, to name a few examples. Additionally, for *Paenibacillus polymyxa* no literature data for qO_2 values and optical density to cell dry weight correlations could be found, thus, literature data from *Bacillus subtilis* were used.

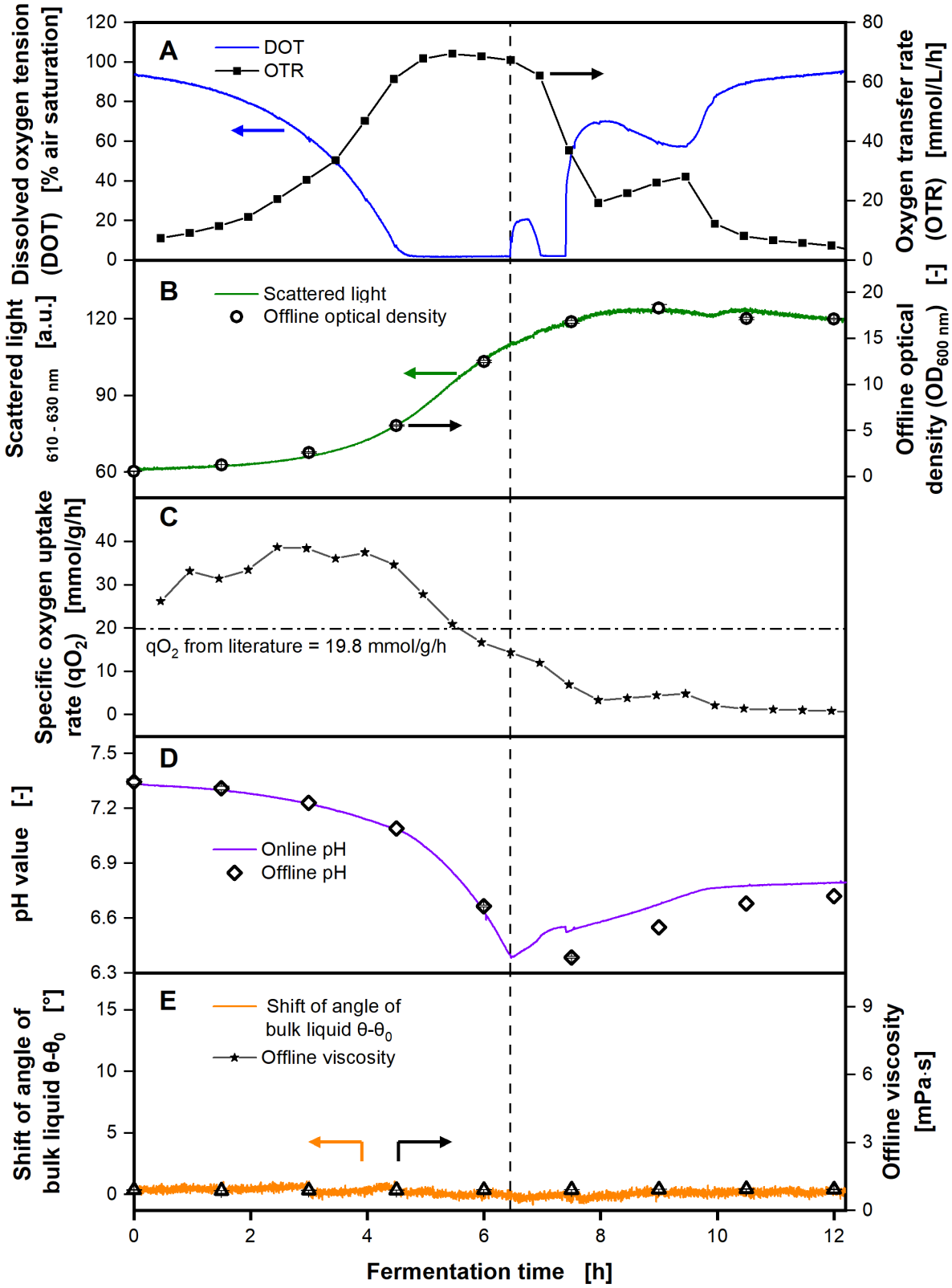

Appendix 33: Data from cultivation of *Escherichia coli* from Fig. 3-5, extended by subfigure C.

(C) Specific oxygen uptake rate (qO_2), calculated based on the recorded data of OTR and scattered light. A correlation between scattered light and offline optical density was derived from recorded data (see Appendix 34). A correlation between optical density and cell dry weight was found in the literature[126]. The vertical dashed-dotted line indicates qO_2 values from literature[127].

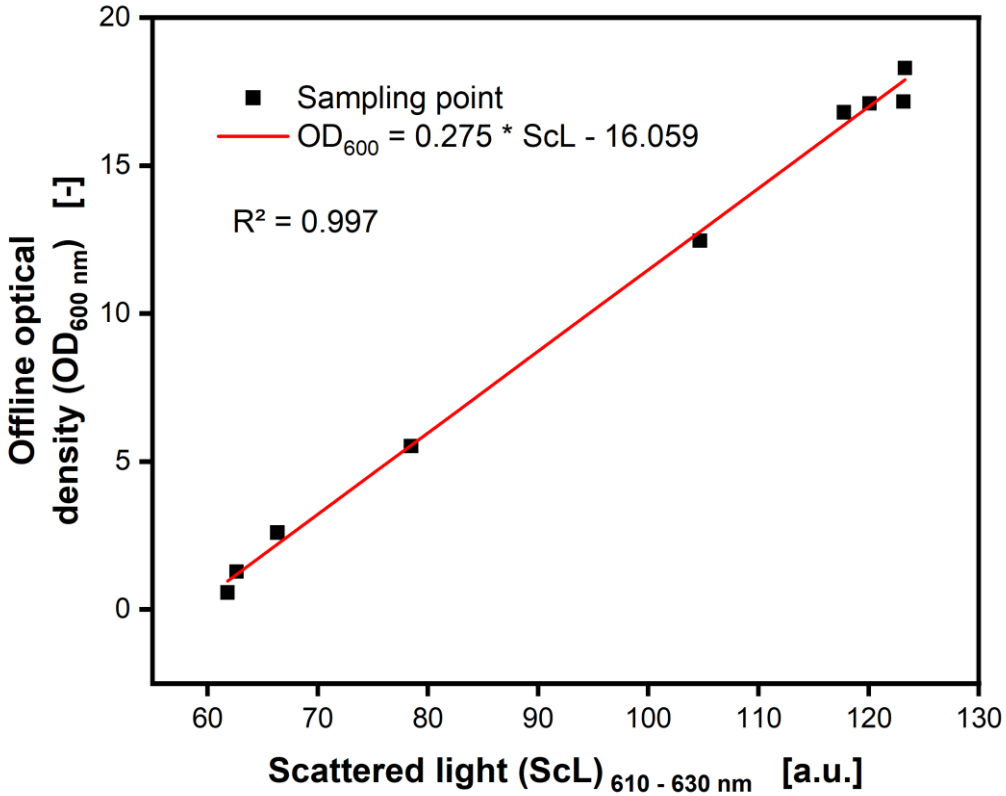

Appendix 34: Correlation between offline optical density (OD_{600}) and scattered light for *Escherichia coli*.

The data used for the calculation originate from the cultivation of *Escherichia coli*, shown in Fig. 3-5.

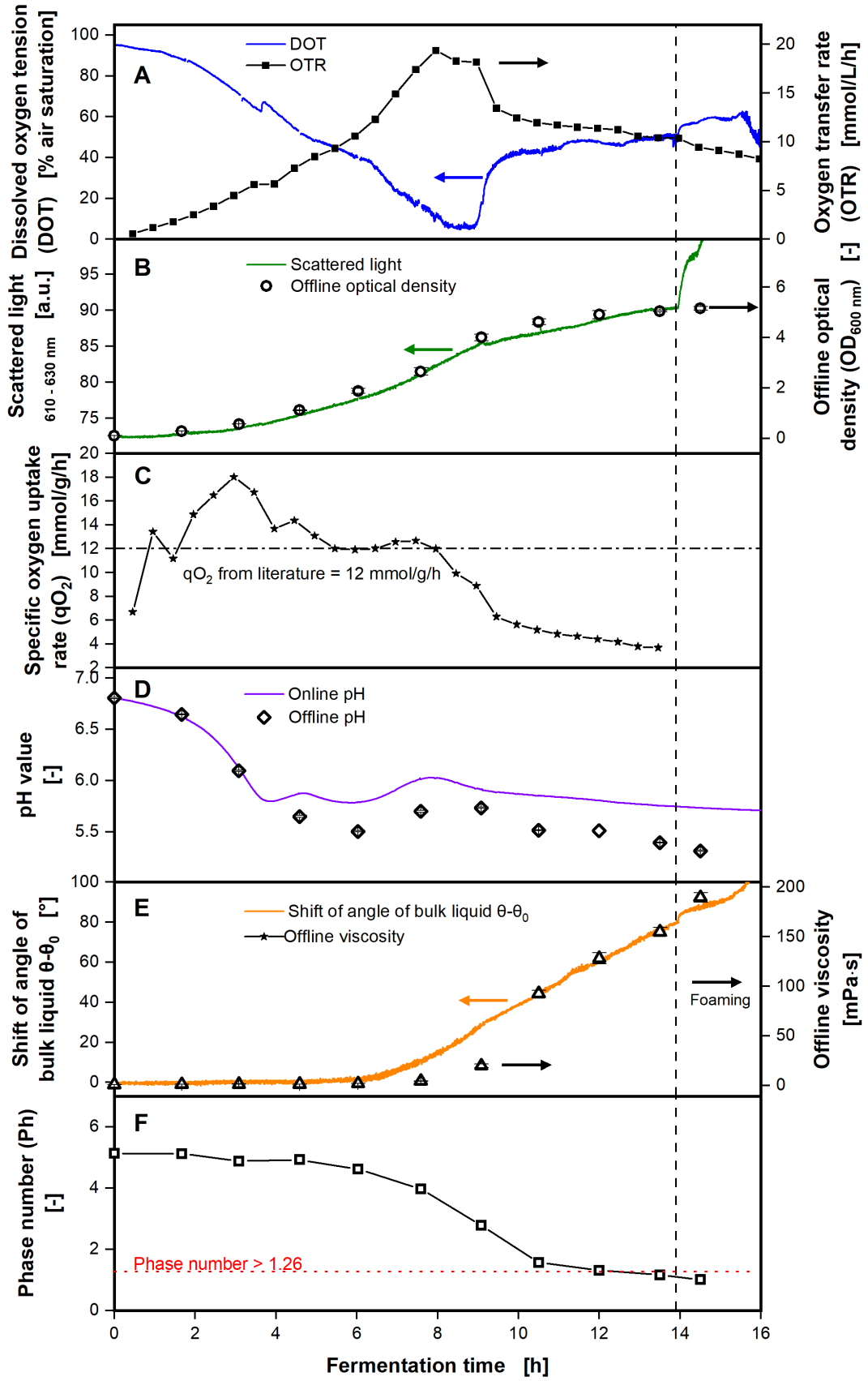

Appendix 35: Data from cultivation of *Paenibacillus polymyxa* from Fig. 3-7, extended by subfigure C.

(**C**) Calculation of the specific oxygen uptake rate (qO_2), based on recorded data of OTR and scattered light. A correlation between scattered light and offline optical density was derived from recorded data

(see Appendix 36). A correlation between optical density and cell dry weight was found in the literature[67]. The vertical dashed-dotted line indicates qO_2 values from literature[128]. For correlations between optical density and cell dry weight and qO_2, literature data of *Bacillus subtilis* were used, since data on *Paenibacillus polymyxa* are sparse.

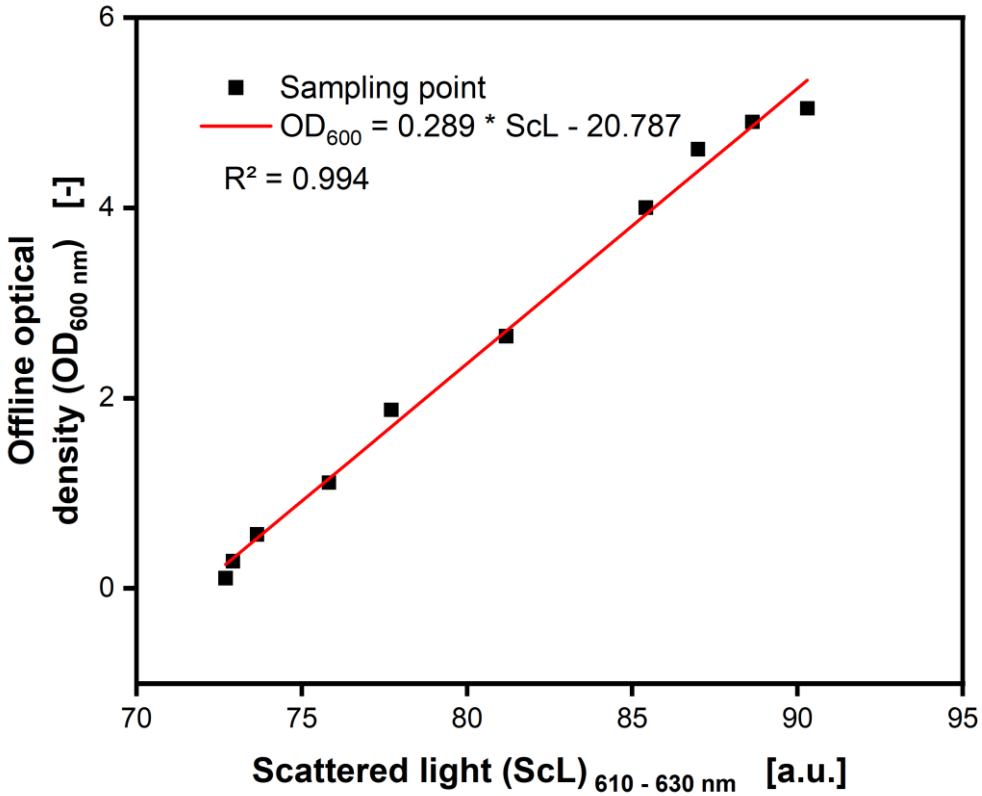

Appendix 36: Correlation between offline optical density (OD_{600}) and scattered light for *Paenibacillus polymyxa*.

The data used for the calculation originate from the cultivation of *Paenibacillus polymyxa*, shown in Fig. 3-7.

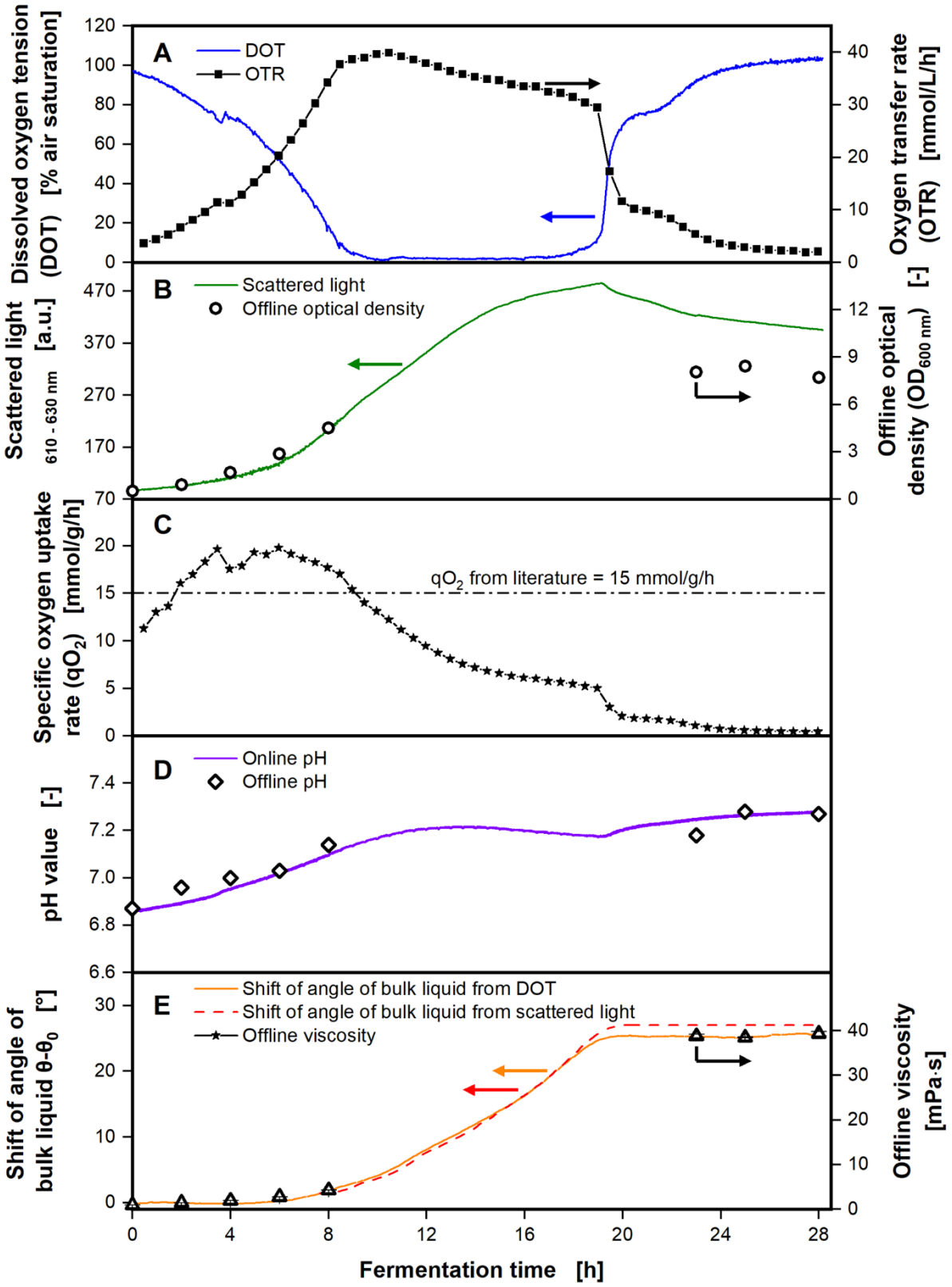

Appendix 37: Data from cultivation of *Xanthomonas campestris* from Fig. 3-8, extended by subfigure C.

(**C**) Calculation of the specific oxygen uptake rate (qO_2), based on recorded data of OTR and scattered light. A correlation between scattered light and offline optical density was derived from recorded data (see Appendix 38). A correlation between optical density and cell dry weight was found in the literature[129]. The vertical dashed-dotted line indicates qO_2 values from literature[130].

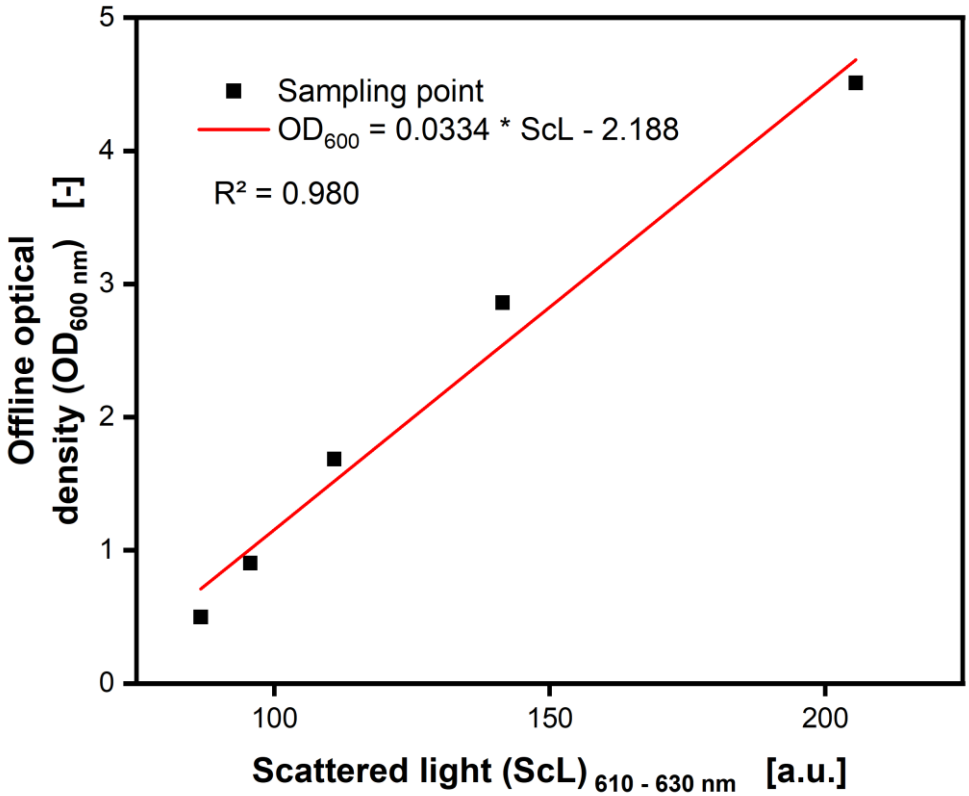

Appendix 38: Correlation between offline optical density (OD_{600}) and scattered light for *Xanthomonas campestris*.

The data used for the calculation originate from the cultivation of *Xanthomonas campestris*, shown in Fig. 3-8.

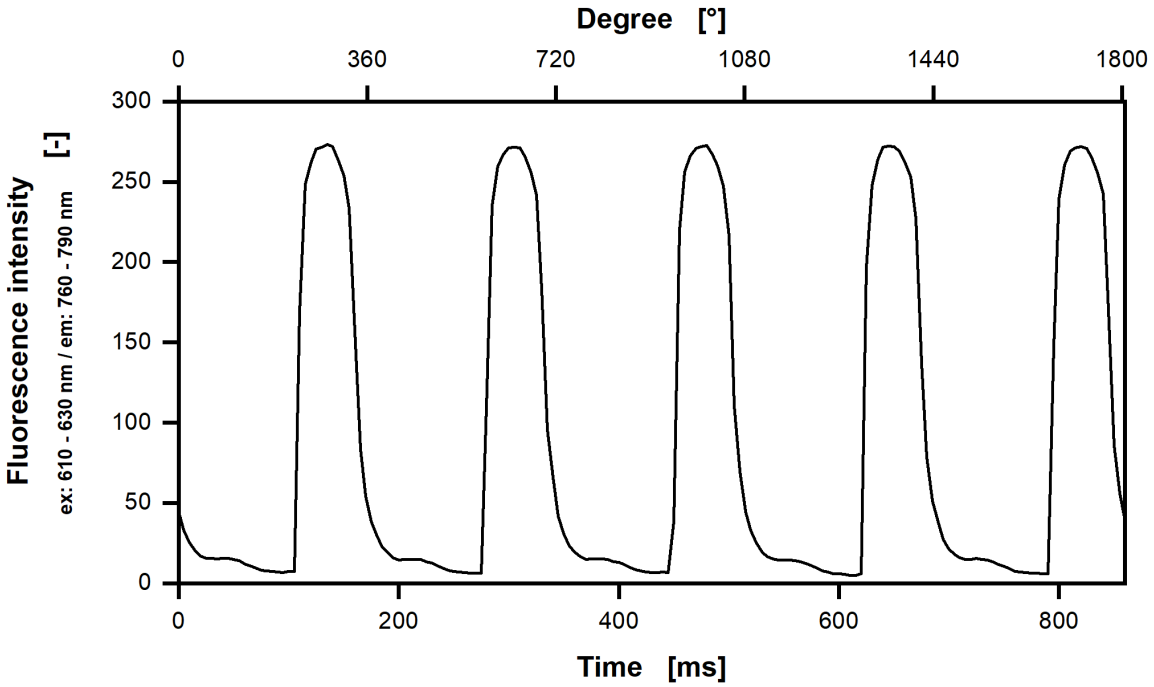

Appendix 39: Fluorescence intensity of Oxnano nanoparticles of the *Escherichia coli* cultivation from Fig. 3-5.

Fluorescence intensity was used for the detection of the leading edge of the rotating bulk liquid. At a shaking frequency of 350 rpm, one 360° rotation takes approximately 171 ms. The fluorescence signal of five consecutive rotations is shown, after a cultivation time of 4 h. Cultivation conditions: Wilms-MOPS medium with 20 g/L glucose, 0.2 mg/mL Oxnano nanoparticles, range of pH spot = 6 – 8, initial pH = 7.5, initial OD_{600} = 0.5, shaking frequency (n) = 350 rpm, filling volume (V_L) = 10 mL, shaking diameter (d_0) = 50 mm, temperature (T) = 37°C.

Appendix 40: Calculation of the glycerol carryover

Cryogenic cultures had an optical density of OD_{600} = 4 and a glycerol concentration of c_{gly} = 150 g/L.

For pre-cultures, 10 mL of Wilms-MOPS medium was inoculated with the cryogenic culture to an initial optical density of OD_{600} = 0.2. Therefore, $\frac{10\ \text{mL} \cdot 0.2}{4} = 0.5\ \text{mL}$ of cryogenic culture was used. This led to an initial glycerol concentration in the pre-culture of $c_{gly} = \frac{0.5\ \text{mL} \cdot 150\ {}^{g}/_{L}}{10\ \text{mL}} = 7.5\ \frac{g}{L}$.

Pre-cultures were harvested after approximately 7 h in the early exponential phase. At this time point, the optical density usually reached a value of roughly OD_{600} = 4. Since the pre-culture was harvested in the early exponential phase before glucose depletion, no glycerol was metabolized by this time point.

For main-cultures, 10 mL of Wilms-MOPS medium was inoculated with the pre-culture to an initial optical density of OD_{600} = 0.5. Therefore, $\frac{10\ \text{mL} \cdot 0.5}{4} = 1.25\ \text{mL}$ of pre-culture was used. This led to an initial glycerol concentration in the main-culture of $c_{gly} = \frac{1.25\ \text{mL} \cdot 7.5\ {}^{g}/_{L}}{10\ \text{mL}} = 0.9\ \frac{g}{L}$.

The calculated concentration of the glycerol carryover (c_{gly} = 0.9 g/L) is close to the measured glycerol concentration in the main culture (c_{gly} = 0.5 g/L).

Nomenclature:

c_{gly} = glycerol concentration in g/L.

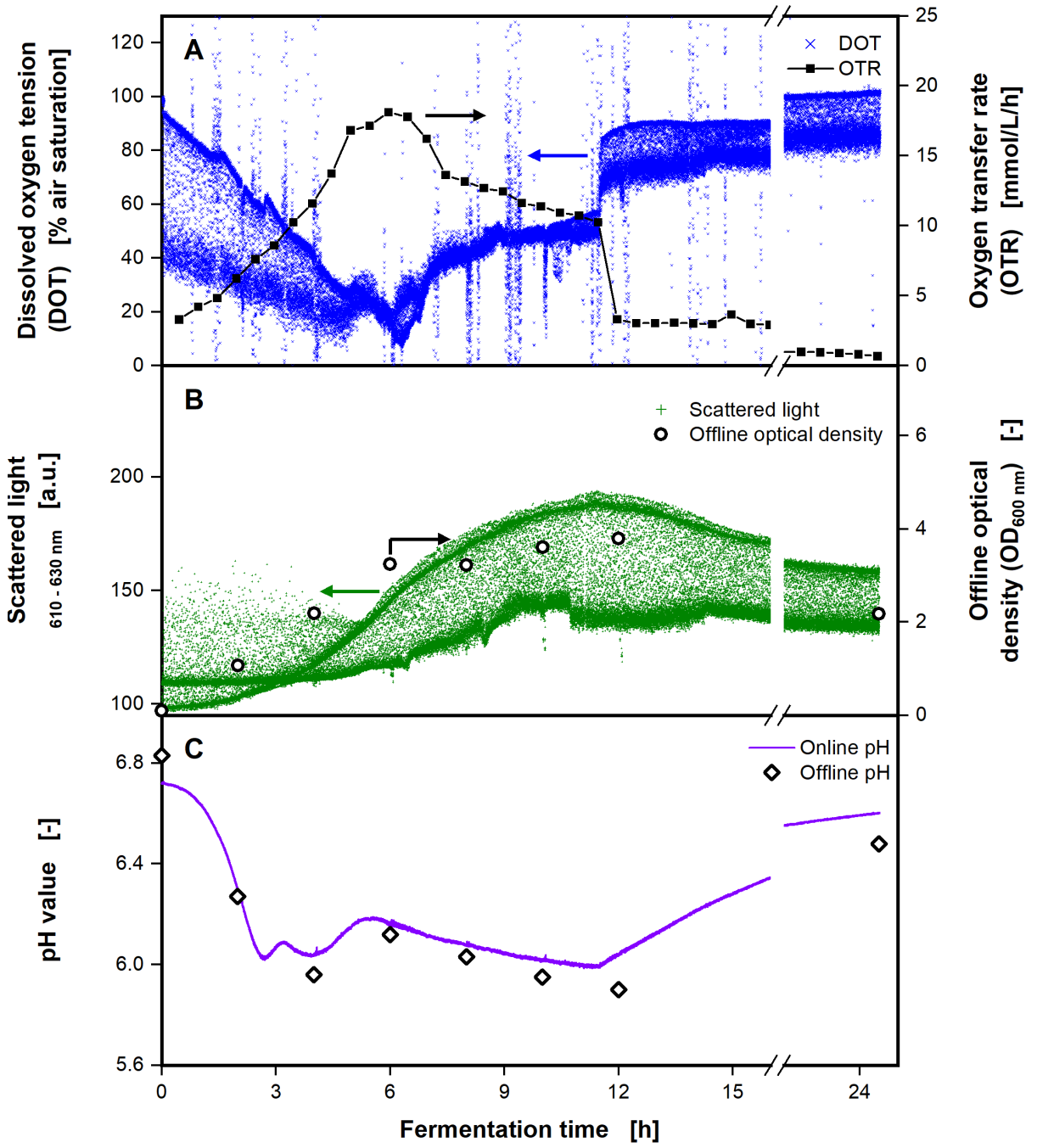

Appendix 41: Online monitoring of a *Paenibacillus polymyxa* cultivation with a non-triggered ShakeVisc device and a RAMOS device.

(A) Online monitoring of dissolved oxygen tension (DOT) and oxygen transfer rate (OTR), with Oxnano nanoparticles and a RAMOS device, respectively. The DOT was calibrated to 100 % in the inoculated medium prior to starting the monitoring. (B) Online monitoring of scattered light, compared to optical density measurements from offline samples at 600 nm. (C) Online monitoring of the pH value with pH sensitive spots, compared to offline pH, measured from offline samples. The pH spot was calibrated at pH 2 and 11 before the cultivation. All offline samples were taken from shake flasks, cultivated in parallel. Cultivation conditions: MM1P100 with 30 g/L glucose, 0.2 mg/mL Oxnano nanoparticles, range of pH spot = 6 – 8, initial pH = 7, initial OD_{600} = 0.5, shaking frequency (n) = 200 rpm, filling volume (V_L) = 30 mL, shaking diameter (d_0) = 50 mm, temperature (T) = 30°C. Offline optical density OD_{600} and offline pH was measured in single measurement. For this experiment, a different batch of casein peptone (Carl Roth GmbH & Co.), compared to Fig. 3-7, was used.

Appendix 42: Shake flask and RAMOS flask with foaming cultivation broth at the end of the cultivation of *Paenibacillus polymyxa*.

Online monitoring and offline samples of the cultivation are shown in Fig. 3-7. Cultivation conditions: MM1P100 medium with 30 g/L glucose, 0.2 mg/mL Oxnano nanoparticles, range of pH spot = 5 – 7, initial pH = 7, initial OD_{600} = 0.5, shaking frequency (n) = 200 rpm, filling volume (V_L) = 30 mL, shaking diameter (d_0) = 50 mm, temperature (T) = 30°C.

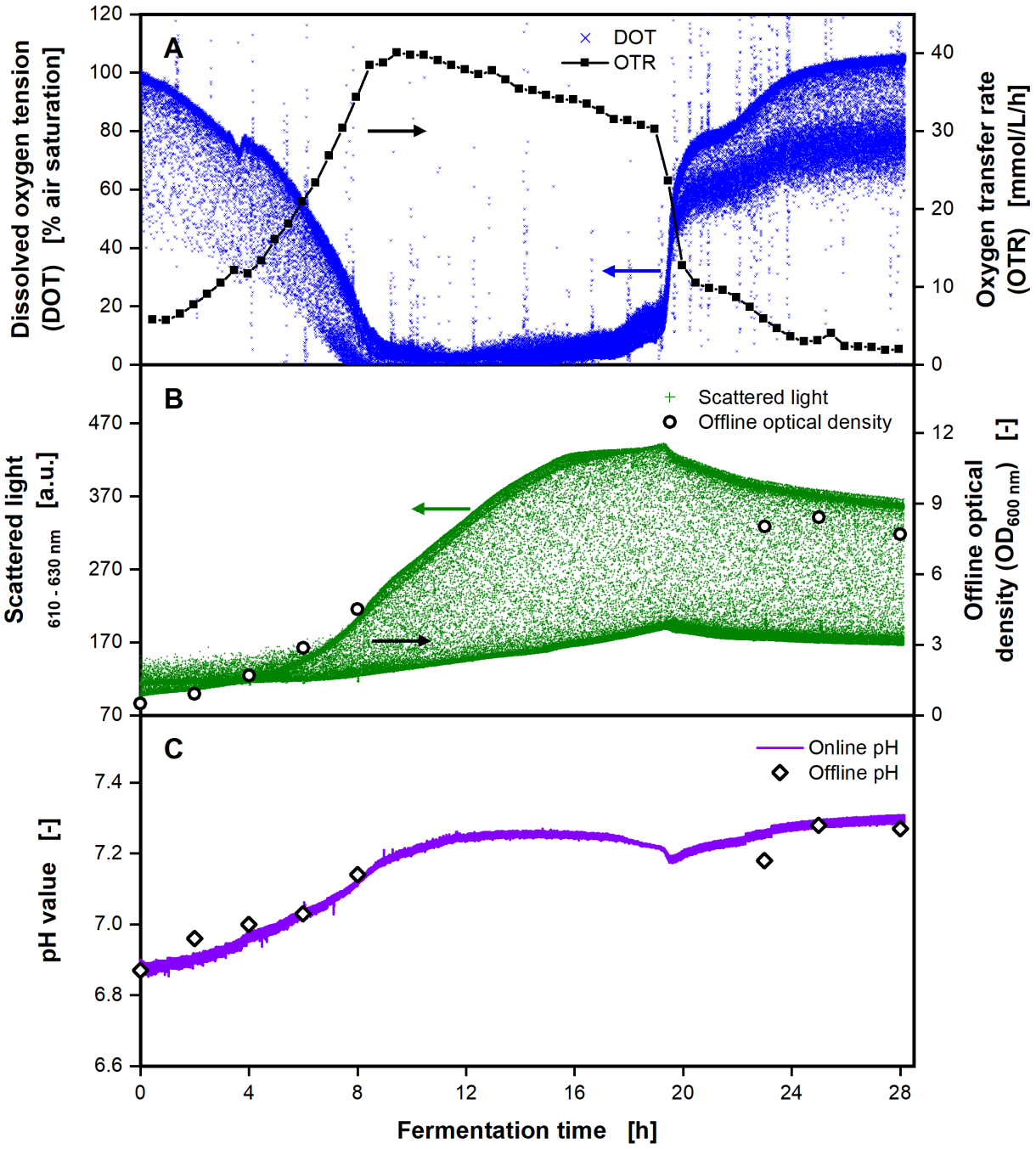

Appendix 43: Online monitoring of a *Xanthomonas campestris* cultivation with a non-triggered ShakeVisc device and a RAMOS device.

(A) Online monitoring of dissolved oxygen tension (DOT) and oxygen transfer rate (OTR), with Oxnano nanoparticles and a RAMOS device, respectively. The DOT was calibrated to 100 % in the inoculated medium prior to starting the monitoring. (B) Online monitoring of scattered light, compared to optical density measurements from offline samples at 600 nm. (C) Online monitoring of the pH value with pH sensitive spots, compared to offline pH measured from offline samples. The pH spot was calibrated at pH 2 and 11 before the cultivation. All offline samples were taken from shake flasks cultivated in parallel. Cultivation conditions: YM medium, 0.2 mg/mL Oxnano nanoparticles, range of pH spot = 6 – 8, initial pH = 6.9, initial OD_{600} = 0.5, shaking frequency (n) = 300 rpm, filling volume (V_L) = 20 mL, shaking diameter (d_0) = 50 mm, temperature (T) = 30°C. Offline optical density OD_{600} and offline pH was measured in single measurement.

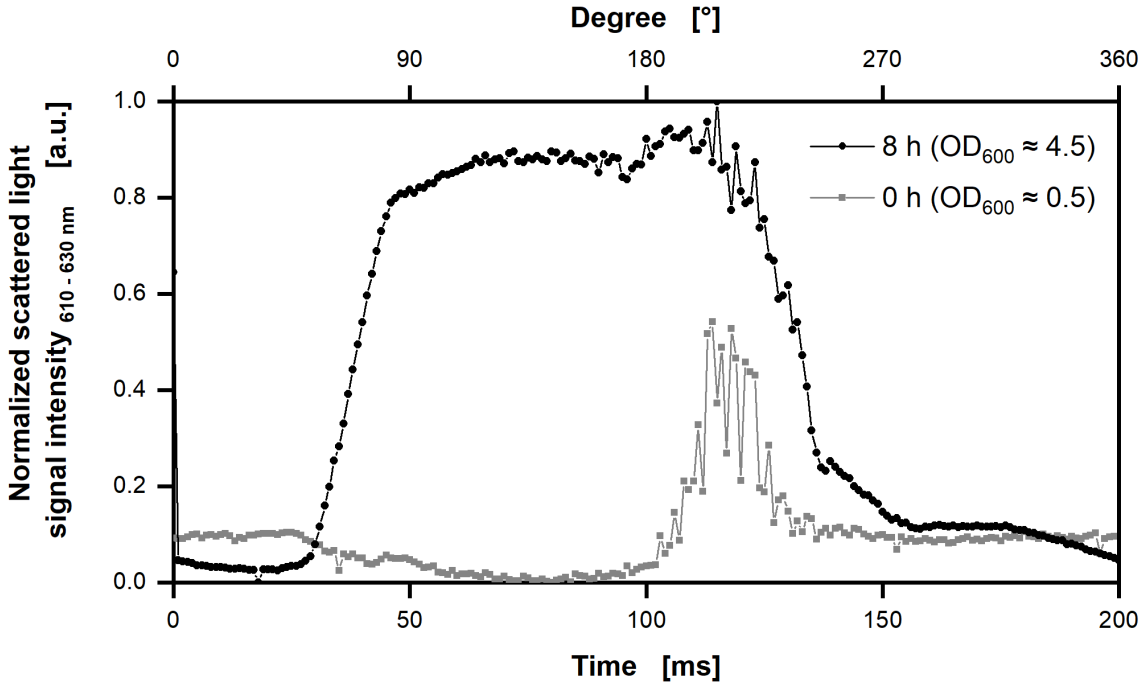

Appendix 44: Normalized scattered light signal intensity of the *Xanthomonas campestris* cultivation from Fig. 3-8.

The scattered light signal intensity was used to trigger the measurement of the shift of the angle of the bulk liquid θ-θ_0. At a shaking frequency of 300 rpm, one 360° rotation takes 200 ms. The normalized scattered light signal intensity of one rotation at two different time points of the cultivation is shown. Cultivation conditions: YM medium, 0.2 mg/mL Oxnano nanoparticles, range of pH spot = 6 – 8, initial pH = 6.9, initial OD_{600} = 0.5, shaking frequency (n) = 300 rpm, filling volume (V_L) = 20 mL, shaking diameter (d_0) = 50 mm, temperature (T) = 30°C.

Rheometer measurements to estimate concentration and chain lengths of hyaluronic acid

In cooperation with Dr. Johannes Gottschalk from the Helmholtz Institute of Biomedical Engineering headed by Prof. Lothar Elling at RWTH Aachen University an attempt to predict chain length of hyaluronic acid based on rheometer measurements was made. Dr. Johannes Gottschalk worked on the enzymatic production of low dispersity hyaluronic acid and provided hyaluronic acid samples used in Appendix 45 and Appendix 46. Hyaluronic acid is a highly viscous shear-thinning biopolymer. It was intended to, at some point, utilize online viscosity monitoring in shake flasks, as presented in chapter 3, to monitor the enzymatic synthesis. In a first step samples provided by Dr. Johannes Gottschalk were measured on a commercial rheometer (Physica MCR 301, Anton Paar GmbH, Ostfildern-Scharnhausen, Germany). Samples were measured on a logarithmic shear ramp from 10 to 5000 s^{-1}. Hyaluronic acid samples were provided with seven different mean chain lengths between 625 and 2300 kDa. Each chain length was provided in three different concentrations of 0.25, 1 and 4 g/L. A concentration of 3 g/L was also provided for 625 kDa. Recorded viscosity values were fitted with the three-parameter viscosity model by Carreau. The Carreau model captures Newtonian behavior and low shear rates and shear-thinning behavior at elevated shear rates well. It takes the following form:

$$\eta_{eff} = \eta_0[1 + (\lambda\gamma)^2]^{\frac{n-1}{2}}$$

where ηeff is the effective dynamic viscosity at the given shear rate γ. η0 is the zero-limit shear viscosity. n is the power-law index. λ is a constant with dimensions of time and relates to the shear rate for which rheological behavior switches form Newtonian to non-Newtonian. Data recorded on the rheometer and accompanying fits of the Carreau model are shown in Appendix 45. Interestingly, all samples are separated based on concentrations at high shear rates of 1000 to 5000 s^{-1}. At 5000 s^{-1} all samples with 0.25 g/L exhibit a viscosity of ~2 mPas. This value is reached by all samples, independent of chain length. Similarly, samples of 1 g/L bundle at 4-5 mPas and samples of 4 g/L at above 10 mPas. This might possibly allow for the determination of hyaluronic concentration of samples with unknown chain lengths.

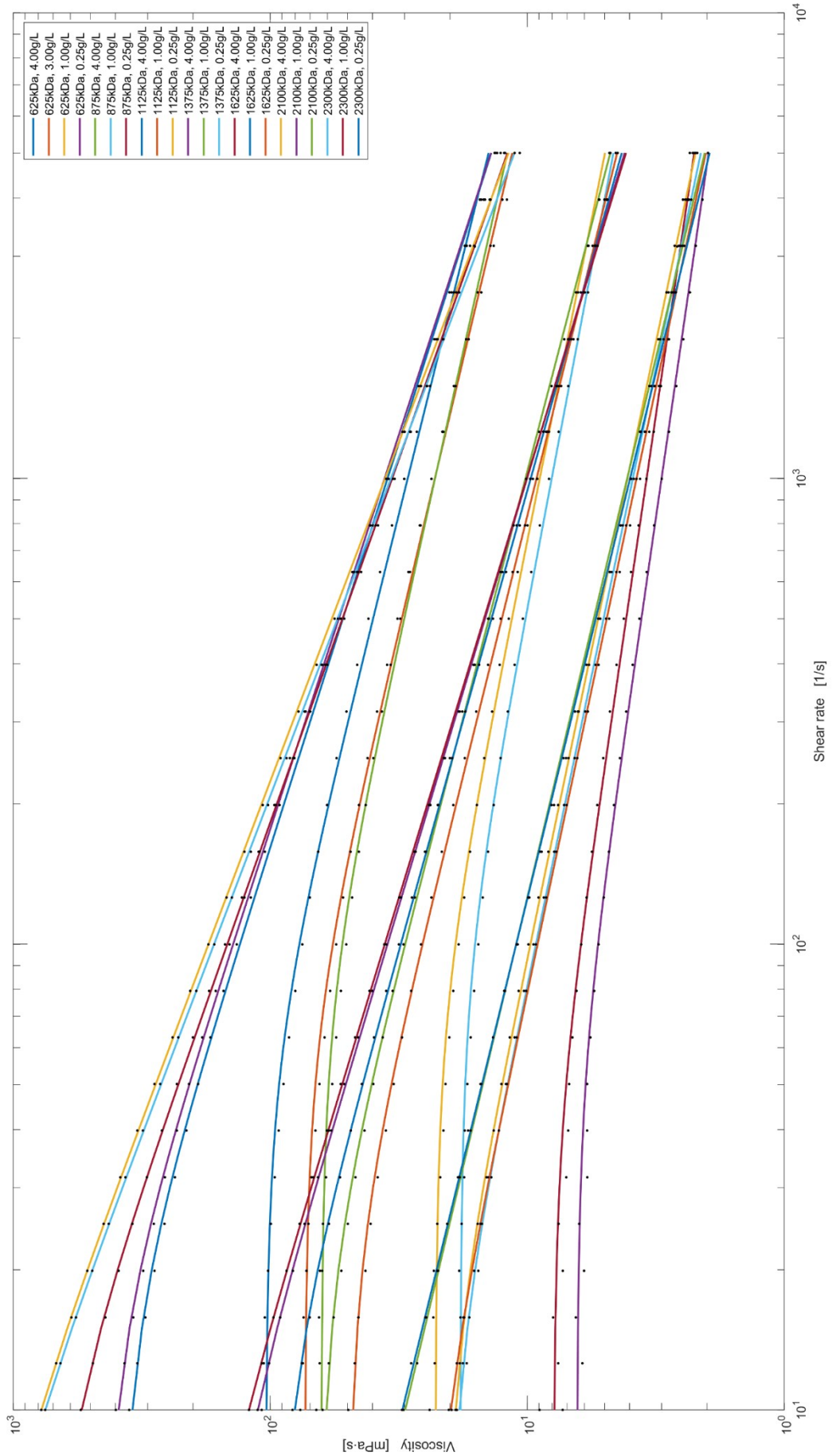
625kDa, 4.00g/L
625kDa, 3.00g/L
625kDa, 1.00g/L
625kDa, 0.25g/L
875kDa, 4.00g/L
875kDa, 1.00g/L
875kDa, 0.25g/L
1125kDa, 4.00g/L
1125kDa, 1.00g/L
1125kDa, 0.25g/L
1375kDa, 4.00g/L
1375kDa, 1.00g/L
1375kDa, 0.25g/L
1625kDa, 4.00g/L
1625kDa, 1.00g/L
1625kDa, 0.25g/L
2100kDa, 4.00g/L
2100kDa, 1.00g/L
2100kDa, 0.25g/L
2300kDa, 4.00g/L
2300kDa, 1.00g/L
2300kDa, 0.25g/L
Viscosity [mPa·s]
Shear rate [1/s]

Appendix 45: Rheometer measurements of low dispersity hyaluronic acid samples-

Hyaluronic acid samples were provided by Johannes Gottschalk from the Helmholtz Institute of Biomedical Engineering of Prof. Lothar Elling at RWTH Aachen University. The hyaluronic acid was produced enzymatically, showing a low dispersity in chain length and therefore molecular weight. Provided were hyaluronic acid samples of seven different chain length between 625 and 2300 kDa. For each chain length samples were provided in concentrations of 0.25, 1 and 4 g/L. A concentration of 3 g/L was also provided for 625 kDa. Samples were measured on a rheometer on a logarithmic shear ramp between 10 and 5000 s^{-1}. All samples were fit with the Carreau model to capture the shear-thinning behavior.

The fit parameter λ of the Carreau model was then used in an attempt to predict the chain length of hyaluronic acid samples. Appendix 46 depicts the chain lengths of all samples over the square root of λ. A linear correlation between the two can be derived, showing an R^2 of 0.96. The linear correlation results in a prediction error of just 118 kDa. This result is true for all tested concentrations and is, importantly, independent of the hyaluronic acid concentration. The combination of both approaches might enable the determination of both hyaluronic acid chain lenghts and concentration of a sample where neither information exists. Unfortunately, no funding was found to continue the investigations in a collaboration with the group of Prof. Elling.

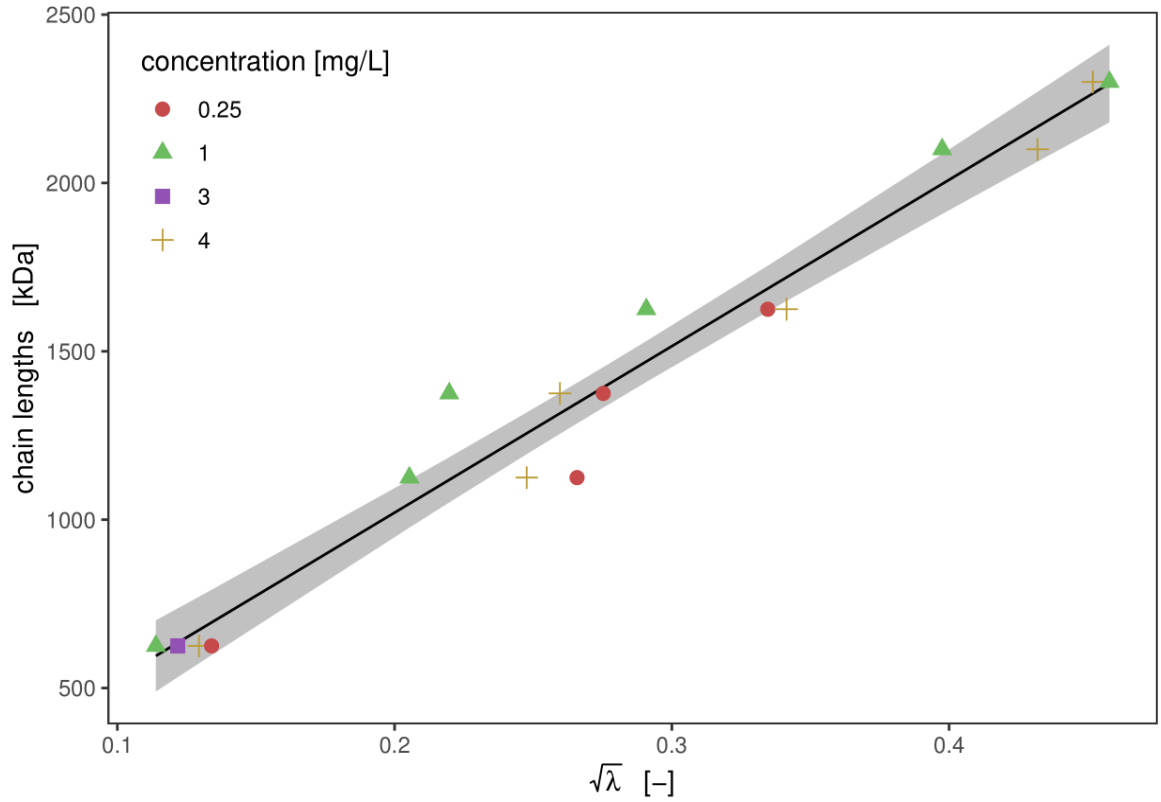

Appendix 46: Correlation of hyaluronic chain length and square root of the fit parameter λ of the Carreau model.

Hyaluronic acid samples were provided by Johannes Gottschalk from the Helmholtz Institute of Biomedical Engineering of Prof. Lothar Elling at RWTH Aachen University. The hyaluronic acid was produced enzymatically, showing a low dispersity in chain length and therefore molecular weight. Provided were hyaluronic acid samples of seven different chain length between 625 and 2300 kDa. For each chain length samples were provided in concentrations of 0.25, 1 and 4 g/L. A concentration of 3 g/L was also provided for 625 kDa. λ was taken from the fits in Appendix 45. Linear correlation between chain lengths and square root of λ results in an R^2 of 0.96 and a prediction error of 118 kDa.